

**CONTINUATION OF DOWN-HOLE GEOPHYSICAL TESTING FOR
ROCK SOCKETS**

FINAL REPORT

**Sponsored by the Florida Department of Transportation Research Center
Contract Number BDK75 977-51**

**Dr. Dennis R. Hiltunen, P.E.
Principal Investigator**

**Mr. Pengxiang Jiang
Graduate Student Researcher**

**DEPARTMENT OF CIVIL & COASTAL ENGINEERING
UNIVERSITY OF FLORIDA**

November 2013



DISCLAIMER

The opinions, findings, and conclusions expressed in this publication are those of the authors and not necessarily those of the State of Florida Department of Transportation or the U.S. Department of Transportation.

Prepared in cooperation with the State of Florida Department of Transportation and the U.S. Department of Transportation.

METRIC CONVERSION TABLE

SYMBOL (US)		MULTIPLY BY	TO FIND	SYMBOL (SI)
LENGTH				
in	inches	25.4	millimeters	mm
ft	feet	0.305	meters	m
yd	yards	0.914	meters	m
mi	miles	1.61	kilometers	km
AREA				
in²	square inches	645.2	square millimeters	mm²
ft²	square feet	0.093	square meters	m²
yd²	square yard	0.836	square meters	m²
ac	acres	0.405	hectares	ha
mi²	square miles	2.59	square kilometers	km²
VOLUME				
fl oz	fluid ounces	29.57	milliliters	mL
gal	gallons	3.785	liters	L
ft³	cubic feet	0.028	cubic meters	m³
yd³	cubic yards	0.765	cubic meters	m³
MASS				
oz	ounces	28.35	grams	g
lb	pounds	0.454	kilograms	kg
T	short tons (2000 lb)	0.907	megagrams (or "metric ton")	Mg (or "t")
TEMPERATURE (exact degrees)				
°F	Fahrenheit	5 (F-32)/9 or (F-32)/1.8	Celsius	°C
FORCE and PRESSURE or STRESS				
lbf	poundforce	4.45	newtons	N
lbf/in²	poundforce per square inch	6.89	kilopascals	kPa
SYMBOL (SI)		MULTIPLY BY	TO FIND	SYMBOL (US)
LENGTH				
mm	millimeters	0.039	inches	in
m	meters	3.28	feet	ft
m	meters	1.09	yards	yd
km	kilometers	0.621	miles	mi
AREA				
mm²	square millimeters	0.0016	square inches	in²
m²	square meters	10.764	square feet	ft²
m²	square meters	1.195	square yards	yd²
ha	hectares	2.47	acres	ac
km²	square kilometers	0.386	square miles	mi²
VOLUME				
mL	milliliters	0.034	fluid ounces	fl oz
L	liters	0.264	gallons	gal
m³	cubic meters	35.314	cubic feet	ft³
m³	cubic meters	1.307	cubic yards	yd³
MASS				
g	grams	0.035	ounces	oz
kg	kilograms	2.202	pounds	lb
Mg (or "t")	megagrams (or "metric ton")	1.103	short tons (2000 lb)	T
TEMPERATURE (exact degrees)				
°C	Celsius	1.8C+32	Fahrenheit	°F
FORCE and PRESSURE or STRESS				
N	newtons	0.225	poundforce	lbf
kPa	kilopascals	0.145	poundforce per square inch	lbf/in²

1. Report No.	2. Government Accession No.	3. Recipient's Catalog No.	
4. Title and Subtitle Continuation of Down-Hole Geophysical Testing for Rock Sockets		5. Report Date November 2013	
		6. Performing Organization Code	
7. Author(s) Pengxiang Jiang and Dennis R. Hiltunen		8. Performing Organization Report No.	
9. Performing Organization Name and Address Department of Civil and Coastal Engineering University of Florida 365 Weil Hall, P.O. Box 116580 Gainesville, FL 32611-6580		10. Work Unit No. (TRAVIS)	
		11. Contract or Grant No. BDK75 977-51	
12. Sponsoring Agency Name and Address Florida Department of Transportation 605 Suwannee Street, MS 30 Tallahassee, FL 32399		13. Type of Report and Period Covered Final Report April 2011-November 2013	
		14. Sponsoring Agency Code	
15. Supplementary Notes			
16. Abstract Site characterization for the design of deep foundations is crucial for ensuring a reliable and economic substructure design, as unanticipated site conditions can cause significant problems and disputes during construction. Traditional invasive exploration methods sample a small volume of material and insufficiently assess spatial variation in subsurface conditions. Established and emerging surface-based geophysical exploration methods may identify large-scale spatial variability, but fail to provide a detailed picture of the rock quality at depths where a socket is required for the design of a drilled shaft foundation. In order to compensate for the shortcomings of these methods, a new borehole-based characterization method has been developed, which creates images of the shear wave velocity profile along and around the borehole to provide credible socket material analyses and detect nearby anomalies. The proposed imaging technique is based on the time-domain full waveform inversion of elastic waves generated inside a borehole, which are captured by a string of sensors placed vertically along the borehole wall. This approach has the ability to simulate all possible wave types of seismic wavefields, and then compare these simulations with observed data to infer complex subsurface properties. This method formulates and solves the forward model of elastic wave propagation within a borehole using ABAQUS, a commercially available finite element package. The inversion is cast as a Least Square optimization problem solved using the regularized Gauss-Newton method. To test the proposed imaging technique, the present study performed comprehensive numerical studies. First, the accuracy of the forward model was validated. Then, the capability of the proposed imaging technique was evaluated by inverting a series of three-dimensional (3-D) synthetic data sets, including a homogeneous model, a horizontally layered model with high impedance contrast, a vertically layered model that mimicked borehole preparation, and simplified earth models containing ring-type anomalies and isolated anomalies. Good models were recovered for each case presented herein.			
17. Key Word Borehole tool, drilled shafts, finite element method, full waveform, Gauss-Newton method, rock sockets, seismic waves		18. Distribution Statement No Restrictions	
19. Security Classif. (of this report) Unclassified	20. Security Classif. (of this page) Unclassified	21. No. of Pages 118 Pages	22. Price

EXECUTIVE SUMMARY

Site characterization for the design of deep foundations is crucial for ensuring a reliable and economic substructure design, as unanticipated site conditions can cause significant problems and disputes during construction. Traditional invasive exploration methods sample a small volume of material and insufficiently assess spatial variation in subsurface conditions. Established and emerging surface-based geophysical exploration methods may identify large-scale spatial variability, but fail to provide a detailed picture of the rock quality at depths where a socket is required for the design of a drilled shaft foundation. In order to compensate for the shortcomings of these methods, a new borehole-based characterization method has been developed, which creates images of the shear wave velocity profile along and around the borehole to provide credible socket material analyses and detect nearby anomalies.

The proposed imaging technique is based on the time-domain full waveform inversion of elastic waves generated inside a borehole, which are captured by a string of sensors placed vertically along the borehole wall. This approach has the ability to simulate all possible wave types of seismic wavefields, and then compare these simulations with observed data to infer complex subsurface properties. This method formulates and solves the forward model of elastic wave propagation within a borehole using ABAQUS, a commercially available finite element package. The inversion is cast as a Least Square optimization problem solved using the regularized Gauss-Newton method.

To test the proposed imaging technique, the present study performed comprehensive numerical studies. First, the accuracy of the forward model was

validated. Then, the capability of the proposed imaging technique was evaluated by inverting a series of three-dimensional (3-D) synthetic data sets, including a homogeneous model, a horizontally layered model with high impedance contrast, a vertically layered model that mimicked borehole preparation, and simplified earth models containing ring-type anomalies and isolated anomalies. Good models were recovered for each case presented herein.

TABLE OF CONTENTS

page

CHAPTER

1	INTRODUCTION	12
1.1	Problem Statement	12
1.2	Hypothesis	14
1.3	Objectives	14
1.4	Scope.....	15
1.5	Organization of Report.....	15
2	SITE CHARACTERIZATION USING SEISMIC WAVES.....	16
2.1	Introduction	16
2.2	Seismic Waves	17
2.3	Surface-based Seismic Methods	18
2.3.1	Seismic Reflection Method	18
2.3.2	Seismic Refraction Method.....	19
2.3.3	Surface Wave Method	21
2.4	Borehole-based Seismic Methods	22
2.4.1	Crosshole Method	22
2.4.2	Downhole Method	23
2.4.3	Suspension P-S Velocity Logging	24
2.4.4	Full Waveform Sonic Logging.....	25
2.5	Initiation of the Current Research	26
3	FULL WAVEFORM INVERSION WITHIN A BOREHOLE	36
3.1	Introduction of Full Waveform Inversion.....	36
3.2	Forward Problem	38
3.2.1	Theoretical Derivation.....	38
3.2.2	Finite Element Modeling	39
3.2.2.1	Spatial-temporal discretization	40
3.2.2.2	Numerical Implementation	41
3.3	Inverse Problem.....	43
3.3.1	Introduction.....	43
3.3.2	Gauss-Newton Method.....	44
3.3.3	Regularized Gauss-Newton Method.....	46
3.4	Practical Strategies for FWI	48
3.4.1	Frequency Filtering.....	48
3.4.2	Time Windowing.....	49
4	VALIDATION OF FORWARD MODEL AND FULL WAVEFORM INVERSION	56

4.1	Introduction	56
4.2	Validation of the Forward Model	56
4.3	Inversion of Synthetic Data Generated by the Forward Model.....	57
4.3.1	Horizontally Layered Model	59
4.3.2	Cylindrically Layered Model.....	61
4.4	Inversion of Synthetic Data Generated from the 3-D Borehole Model	64
4.4.1	Homogeneous Model	65
4.4.2	Homogeneous Models with Ring Anomalies	65
4.4.3	Horizontally Layered Models with a Ring Anomaly.....	67
4.5	Summary	68
5	LOCATING ISOLATED ANOMALIES NEAR A BOREHOLE.....	86
5.1	Introduction	86
5.2	Overview of Strategies.....	86
5.2.1	Inversion with Multi-component Data.....	86
5.2.2	Inversion with Multi-bandwidth Sources	87
5.2.3	Inversion from Multiple Planes and with Multiple Shots.....	87
5.3	Synthetic Model Studies	88
5.3.1	Synthetic Model 1	88
5.3.2	Synthetic Model 2	91
5.3.3	Synthetic Model 3.....	92
5.3.4	Synthetic Model 4.....	93
5.3.5	Synthetic Model 5.....	95
5.4	Summary	96
6	CLOSURE	110
6.1	Summary of Findings.....	110
6.1.1	Forward Modeling.....	110
6.1.2	Inversion System	110
6.1.3	Inversion Results	111
6.2	Conclusions	111
6.3	Recommendations	113
	LIST OF REFERENCES	114

LIST OF FIGURES

<u>Figure</u>	<u>page</u>
2-1 Body waves: a) Compressional waves and b) Shear waves (from Stokoe and Santamarina, 2000)	29
2-2 Surface waves: a) Rayleigh waves and b) Love waves (from Stokoe and Santamarina, 2000)	29
2-3 Field arrangement used in the seismic reflection method: a) Normal moveout, b) Common offset, and c) Common depth point (from Stokoe and Santamarina, 2000)	30
2-4 Interpretation of a seismic reflection test: a) Time-migrated cross-section and b) Interpreted geologic profile (from NRC, 2000)	30
2-5 Seismic refraction method: a) Test configuration, b) Travel times, and c) Reconstructed P-wave velocity tomogram	31
2-6 Surface wave method: a) Test configuration, b) Rayleigh wave dispersion, and c) Inverted shear wave velocity profile	32
2-7 Crosshole and downhole methods: a) Crosshole testing, b) Downhole testing, and c) Crosshole tomography (from Stokoe and Santamarina, 2000) ...	33
2-8 Test setup for the suspension P-S velocity logging (from Stokoe and Santamarina, 2000)	34
2-9 Test setup for the full waveform sonic logging (from Chabot, 2003)	34
2-10 Schematics of test setup for the proposed borehole-based FWI: a) Cross-sectional view and b) Top view with eight planes to be scanned	35
3-1 Dispersion of an axially propagating surface wave in a borehole with Poisson's ratio of 0.25 (from Kalinski, 1998)	51
3-2 Discretization of an axisymmetric borehole model	51
3-3 A simplified flowchart for the proposed inversion scheme	52
3-4 Concept of frequency filtering: a) Raw data and the frequency spectrum, b) First-level filtering, and c) Second-level filtering	54
3-5 Concept of time windowing: gradually increasing the length of the window to facilitate convergence	55
4-1 Waveform comparison for boreholes with varying radii: a) Axial displacement and b) Radial displacement	69

4-2	Waveform comparison for a borehole with a 1 km radius and plane-strain flat ground solution: a) Tangential displacement and b) Normal displacement	70
4-3	Triangular wavelet sources: a) High-frequency source and b) Low-frequency source.....	71
4-4	Borehole synthetic data: a) Radial displacement and b) Axial displacement.....	72
4-5	The process for conducting the synthetic experiment inside a borehole (axisymmetric model)	73
4-6	Horizontally layered model: a) True model and b) Initial model.....	74
4-7	Inversion of the horizontally layered model using the multiscale approach: a) Short time window with low-pass filter, b) Short time window without filter, c) Full time window with low-pass filter, and d) Full time window without filter	76
4-8	Cylindrically layered model: a) True model and b) Initial model.....	76
4-9	Inversion of the cylindrically layered model using the multiscale approach: a) Short time window with low-pass filter, b) Short time window without filter, c) Full time window with low-pass filter, and d) Full time window without filter	78
4-10	The process for conducting the synthetic experiment inside a borehole (3-D model)	79
4-11	Homogeneous model: a) True model, b) Inverted model, and c) Waveform match and convergence curve.....	80
4-12	Homogeneous model with ring-type anomaly (near): a) True model, b) Inverted model, and c) Waveform match and convergence curve.....	81
4-13	Homogeneous model with ring-type anomaly (far): a) True model, b) Inverted model, and c) Waveform match and convergence curve.....	82
4-14	Homogeneous model with ring-type anomaly (farther): a) True model, b) Inverted model, and c) Waveform match and convergence curve.....	83
4-15	Horizontally layered model with ring-type anomaly: a) True model, b) Inverted model, c) Inversion for short time window, d) Inversion for medium time window, and e) Inversion for full time window.....	85
5-1	Synthetic model 1: true model and velocity section	98
5-2	Synthetic model 1: inversion result of 0-degree plane	98
5-3	Synthetic model 1: inversion result of 90-degree plane	99
5-4	Synthetic model 1: inversion result of 180-degree plane	99

5-5	Synthetic model 2: true model and velocity section	100
5-6	Synthetic model 2: inversion result of 0-degree plane	100
5-7	Synthetic model 2: inversion result of 90-degree plane	101
5-8	Synthetic model 2: inversion result of 180-degree plane	101
5-9	Synthetic model 3: true model and velocity section	102
5-10	Synthetic model 3: inversion result of 0-degree plane	102
5-11	Synthetic model 3: inversion result of 90-degree plane	103
5-12	Synthetic model 3: inversion result of 180-degree plane	103
5-13	Synthetic model 4: true model	104
5-14	Synthetic model 4: velocity section of 0–180-degree plane	104
5-15	Synthetic model 4: inversion result of 0-degree plane with one shot	105
5-16	Synthetic model 4: inversion result of 90-degree plane with one shot	105
5-17	Synthetic model 4: inversion result of 180-degree plane with one shot	106
5-18	Synthetic model 4: inversion result of 0-degree plane with two shots	106
5-19	Synthetic model 4: inversion result of 90-degree plane with two shots	107
5-20	Synthetic model 4: inversion result of 180-degree plane with two shots	107
5-21	Synthetic model 5: true model and velocity section	108
5-22	Synthetic model 5: inversion result of 0-degree plane	108
5-23	Synthetic model 5: inversion result of 90-degree plane	109
5-24	Synthetic model 5: inversion result of 180-degree plane	109

CHAPTER 1 INTRODUCTION

1.1 Problem Statement

Unanticipated site conditions are the most common cause of significant problems and disputes that occur during the construction of deep foundations and other geotechnical structures. The problem is particularly acute in karst terrain, where subsurface conditions are often highly variable. Therefore, site characterization appears to be crucial for ensuring a reliable and economic substructure design.

Traditional invasive exploration methods (e.g., SPT and CPT) probe and sample a small volume of material, often insufficiently assessing spatial variation in subsurface conditions. Standard surface seismic methods (e.g., seismic refraction and surface wave dispersion), which are routinely used for subsurface investigation in civil engineering, are limited in the characterization of challenging geological profiles that include low-velocity anomalies or sharp impedance contrasts. In addition, these methods, like all surface-based geophysical methods, have limited resolving capability below surface level.

To obtain credible information regarding material below surface level, borehole-based geophysical methods have to be used. Conventional crosshole and downhole methods provide one-dimensional (1-D) vertical velocity profiles based on direct arrivals, which are often inadequate for design purposes. Borehole surface wave method (Kalinski, 1998) can be used to derive 1-D lateral S-wave velocity profile based on surface wave dispersion, but the investigation depth is only a few inches into the formation. On the other hand, crosshole tomography is capable of producing two-dimensional (2-D) velocity tomograms between boreholes using travel time inversion.

However, if 3-D material characterization is required – when locating a drilled shaft in karst terrain, for instance – the crosshole technique can be too costly, as it requires multiple receiver holes around the source hole.

Recent advances in borehole geophysics reveal that acoustic logging in a fluid-filled borehole can create 1-D P- and S-wave velocity profiles (Kitsunezaki, 1980). This acoustic logging method can also use reflectivity to characterize the structural properties of the geologic formations behind the borehole wall (Chabot, 2003). The challenge remains as to how the derived wave velocities can be associated with the migrated structural image.

By taking advantage of the ever-increasing power of computers, the full waveform inversion (FWI) technique can now extract information from complete ground surface wavefields in order to provide high-resolution 2-D velocity images of the subsurface (Virieux and Operto, 2009). The current research explores the possibility of extending FWI techniques to the borehole level in order to quantitatively characterize the spatial variations in rock formations. This possibility is of particular advantage when evaluating karst terrain, as those subsurface conditions are often highly variable. Given the increased use in Florida of single, large-diameter, non-redundant drilled shafts as foundation elements, a comprehensive evaluation technique is imperative. Although surface-based FWI has proven superior over state-of-practice seismic methods in characterizing spatial variability, the inherent tradeoff between resolution and depth is unavoidable. Most rock-socketed drilled shafts extend deep beneath the ground; therefore, borehole-based FWI could potentially lead to a more reliable and economic

design solution for drilled shafts in karst terrain, since this technique is capable of assessing potential sockets in more detail.

3-D FWI within a borehole would be ideal for assessing drilled shaft sockets; however, 3-D surface-based FWI is still in its infancy with numerous uncertainties to be addressed, making 3-D borehole-based FWI beyond the scope of this study. Therefore, two-and-a-half-dimensional (2.5-D) borehole-based FWI, which is based on an axisymmetric forward model, is proposed instead, in order to evaluate the feasibility of characterizing spatial variations in rock formations for drilled shaft foundation design. This study evaluated the capability of the proposed imaging technique by inverting a series of 3-D synthetic data sets, including a homogeneous model, a horizontally layered model with high impedance contrast, a cylindrically layered model that mimicked borehole preparation, and simplified earth models containing ring-type anomalies and isolated anomalies. Good models were recovered for each case.

1.2 Hypothesis

The borehole-based FWI technique can be used to characterize the elastic properties of material along and around a borehole, and is capable of producing images with higher resolution than any other available site characterization method.

1.3 Objectives

The primary objective of this research is to evaluate the feasibility of 2.5-D borehole-based FWI technique for characterizing the elastic properties of material along and around a borehole. Specific objectives of this research include the following:

1. Develop an accurate and efficient borehole model that can be used as the forward engine for generating synthetic waveforms.
2. Develop a reliable and efficient inversion algorithm for borehole-based FWI in the time domain.

3. Perform synthetic studies for a wide range of geological settings to develop a reasonable array design, including receiver type, number, spacing, and source characteristics.
4. Perform synthetic studies to investigate the feasibility of the proposed imaging technique for locating isolated anomalies in the vicinity of a borehole.

1.4 Scope

The forward model used in the inversion is based on a 2.5-D axisymmetric borehole model. The synthetic data sets used in the inversion are obtained from truly 3-D borehole models. This study used ABAQUS and MATLAB in the implementation of the proposed imaging technique.

1.5 Organization of Report

Chapter two provides an overview of site characterization methods using seismic waves, both surface-based and borehole-based. Pros and cons of each method are discussed.

Chapter three elaborates on the algorithm of FWI within a borehole, including a theoretical derivation of wave propagation in a cylindrical cavity. This study built the forward model using ABAQUS, and implemented the regularized Gauss-Newton method for the inversion.

Chapter four validates the forward model and presents applications of FWI within a borehole. Optimum array design is recommended.

Chapter five investigates the feasibility of the proposed imaging technique to locate isolated anomalies (i.e., void or cavity) in the vicinity of a borehole. Several strategies are proposed and adopted for this purpose.

Chapter six summarizes the findings of this study, followed by conclusions and recommendations.

CHAPTER 2 SITE CHARACTERIZATION USING SEISMIC WAVES

2.1 Introduction

Exploration geophysics is the study of the subsurface using quantitative physical methods. These methods are based on extensive theoretical and experimental foundations, some dating back more than a century (Stokoe and Santamarina, 2000). For example, Rayleigh (1885), Love (1892), and Lamb (1904) conducted pioneering studies in the propagation of stress waves. Much of the progress in this area has been driven by hydrocarbon exploration and global seismology. Over the past 50 years, geotechnical, geoenvironmental, and earthquake engineering applications in civil engineering have stimulated further development in geophysical exploration methods, among which the seismic methods appear to be the most extensively used site characterization techniques.

Site characterization is a fundamental step in the proper design, construction, and long term performance of all types of civil engineering projects, including foundations, excavations, earth dams, embankments, seismic hazards, environmental issues, tunnels, and offshore structures. Seismic methods of site characterization involve generating and recording seismic waves to investigate the subsurface. Each method is based on the propagation of waves from an artificial source to a set of receivers, followed by an analysis of the subsurface properties of the recorded wavefield. Seismic methods are nondestructive by nature, because they are conducted with a strain level so small that the material conditions are not altered. These methods can be further classified as noninvasive if performed at the surface level, or invasive if boreholes are involved.

Seismic methods can be used to infer engineering design parameters, as strong links exist between the wave propagation characteristics and the mechanical properties of the medium to be characterized, as represented by the following equations:

$$G = \rho \cdot V_s^2 \quad (2-1)$$

$$E = 2G \cdot (1 + \nu) \quad (2-2)$$

$$\nu = \frac{V_p^2 - 2V_s^2}{2(V_p^2 - V_s^2)} \quad (2-3)$$

where V_p and V_s are compressional and shear wave velocities, ρ is mass density, G is shear modulus, E is Young's modulus, and ν is Poisson's ratio.

As these equations show, the compressional and shear wave velocity profiles derived from a typical seismic survey can be used to estimate the elastic moduli of subsurface materials. Therefore, the broad goal of seismic surveys is to assess these parameters and their spatial distribution.

2.2 Seismic Waves

In physics, a wave is a disturbance that travels through space and time, accompanied by a transfer of energy (Aki and Richards, 1980). A wave can be transverse or longitudinal, depending on the direction of particle oscillation in relation to the direction of wave propagation. Transverse waves occur when the oscillations are perpendicular to the direction of propagation. Longitudinal waves occur when the oscillations are parallel to the direction of propagation.

Body waves

For stress waves propagating far from any boundaries in a uniform medium, two fundamental modes of propagation exist: compressional waves (also called P-waves)

and shear waves (also called S-waves). These waves are known as body waves, since they propagate within the body of the medium. P-waves are longitudinal, while S-waves are transverse, as illustrated by the schematics of body waves (Figure 2-1).

Surface waves

Interfaces alter particle motion, instigating other modes of propagation. Rayleigh waves are generated when a free surface interacts with the reflected and refracted body waves. Love waves are created when the multiple total reflections of horizontally polarized shear waves (SH-waves) interact with the surface and underlying stiffer layers. As illustrated by the schematics of these two surface waves, the particle motion of Rayleigh waves is a combination of vertical and horizontal motions, while the particle motion of Love waves is similar to that of SH-waves (Figure 2-2). Therefore, Rayleigh waves are mixed, and Love waves are transverse.

2.3 Surface-based Seismic Methods

Seismic tests are routinely conducted on the ground surface, as the acquisition geometry is readily accessible and the test procedures are relatively cost-effective.

2.3.1 Seismic Reflection Method

The seismic reflection method is one of the oldest seismic methods and is well documented in ASTM standards (ASTM D7128) and many geophysics textbooks (e.g., Burger, 1992). Seismic reflection is founded on the presence of impedance contrasts in the subsurface, which occur as a result of variations in mass density, seismic velocity, or both.

The basic field arrangement used in the seismic reflection method places both source and receivers on the ground surface (Figure 2-3). Typically, P-wave measurements are performed using either vertically impacting sources or explosives.

Waves reflected from interfaces at depth are monitored with vertically sensitive geophones.

Depending on the specific application, varying patterns of the source-receiver layout can be used in the reflection survey in order to optimize the measurements (Stokoe and Santamarina, 2000). The normal moveout is used to estimate the average velocity of the formation (Figure 2-3a). Detection of reflectors is usually obtained using the common offset (Figure 2-3b). The common depth point is used to enhance the signal-to-noise ratio at a specific location (Figure 2-3c).

Advanced data-processing algorithms (e.g., reverse time migration), mostly developed by exploration geophysicists, are available and are becoming more widely used in civil engineering. Typical subsurface cross-sections are interpreted from a seismic reflection survey for identifying the alluvium-bedrock interface (Figure 2-4).

Advantages

- Seismic reflection is effective regardless of depth-related variance in the velocity at which waves propagate through the Earth.
- The subsurface can be qualitatively imaged, even for complex geologic profiles, as the full reflected wavefield is used for data processing.

Disadvantages

- The seismic reflection survey is costly to conduct, as it requires many source and receiver arrangements in order to produce meaningful subsurface images.
- Data processing of seismic reflection requires a high level of expertise.
- Resolution of the migrated image decreases as depth increases.

2.3.2 Seismic Refraction Method

The seismic refraction method is another well-documented (ASTM D5777) geophysical method for noninvasively identifying the stiffness and layer interface of

sediments at shallow depths. Conventional refraction methods are used for simple geologic profiles consisting of a few constant velocity layers with linear interfaces (Palmer, 1980). Using the ever-increasing power of computers, seismic refraction tomography can now produce 2-D velocity tomograms of the subsurface by conducting multiple shot gathers along the receiver array (White, 1989; Zhang and Toksoz, 1998).

In principle, the seismic refraction method is based on the ability to detect wave energy that is critically refracted from a higher velocity layer that underlies lower velocity sediment.

P-wave measurements are typically performed using either vertically impacting sources or explosives, while direct and refracted waves are monitored with vertically sensitive geophones on the ground surface (Figure 2-5a). The travel times are derived by manually selecting the first-arrival signals in the recorded wavefield. The P-wave velocity tomogram is then reconstructed (Figure 2-5b) by matching the synthetically generated travel times with the manually derived travel times (Figure 2-5c).

Advantages

- Seismic refraction can provide high-resolution velocity images of normal profiles at shallow depths, including mild lateral variability.
- The method is well established, and the survey is relatively easy to conduct. Many types of commercial software are available for tomographic reconstruction of the subsurface based on the matching of travel times.

Disadvantages

- Seismic refraction is only effective if the velocity at which waves propagate through the Earth increases as depth increases. In other words, velocity reversals and low-velocity anomalies cannot be detected using this method.
- Only the first-arrival signals are used in data processing, and manually selecting these signals can be time-consuming and tedious.

- Resolution of the reconstructed velocity tomograms decreases as depth increases.

2.3.3 Surface Wave Method

The surface wave method, as the name suggests, uses Rayleigh and Love waves, although Rayleigh waves are used more widely in the field. Two of the most popular methods are the spectral analysis of surface waves (SASW) (Nazarian and Stokoe, 1984; Stokoe et al., 1994) and the multichannel analysis of surface waves (MASW) (Park, et al., 1999; Zywicki, 1999). These methods involve actively exciting Rayleigh wave energy at a fixed point, and then measuring the resulting vertical motion on the surface at various distances (offsets) from the source.

The surface wave method primarily characterizes the dispersion of Rayleigh waves that propagate in a horizontally layered system. The phase velocity, V_r , primarily depends on the material properties (shear wave velocity, mass density, and Poisson's ratio) in a sample approximately one wavelength deep. Waves with different wavelengths sample different depths. As a result of the varying shear stiffness of the layers, waves with different wavelengths travel at different phase velocities. Phase velocity varies with wavelength and frequency, and this variation is characterized as a surface wave dispersion curve. This phase velocity variation is an important site characteristic that is evaluated in the field. The field dispersion curve can be extracted by using 2-D FFT (Foti, 2000) or slant-stack analysis (McMechan and Yedlin, 1981) to transform the raw data set from the time-space domain into the frequency-wave number domain. Once a credible field dispersion curve has been established, it is then inverted to obtain the shear wave velocity profile with depth. Figure 2-6 illustrates a typical

MASW test configuration, field dispersion image, and inverted shear wave velocity profile.

Advantages

- The energy of Rayleigh waves is predominant in the recorded wavefield because these waves represent a high percentage of the energy generated by a vertically impacting source. In addition, since the wavefront is cylindrical, the geometrical attenuation of Rayleigh waves is low, as opposed to the higher geometrical attenuation caused by the spherical wavefronts of body waves.
- Theoretically, the surface wave method is capable of identifying softer layers beneath stiffer materials.
- The field test can be done rapidly and cost-effectively.

Disadvantages

- Assuming the Earth model is horizontally layered, it can only obtain 1-D shear wave velocity profiles.
- Thin layers can be missed if they exhibit high impedance contrasts (e.g., are much stiffer or much softer than the surrounding material).
- Resolution of the inverted shear wave velocity profile decreases as depth increases.

2.4 Borehole-based Seismic Methods

Borehole methods are often employed when inclusions and anomalies may not be properly resolved using surface-based geophysics, or when a higher resolution image is needed at a target zone.

2.4.1 Crosshole Method

The crosshole method (ASTM D4428; Stokoe and Woods, 1972) measures the one-way travel time of seismic energy transmitted between boreholes to determine the elastic moduli of the intervening materials (Figure 2-7a). This method measures the travel times from the source to the receivers (direct travel times) and the travel times between receivers (interval travel times). By measuring the spaces between each

borehole, the depth of the seismic source, and the depth of each receiver, the apparent compressional and shear wave velocities can be calculated. The test is then repeated at multiple depths to obtain a 1-D profile of compressional and shear wave velocities at various depths.

Crosshole tomography measures the travel times of seismic raypaths between two or more boreholes in order to create velocity images of the intermediate materials (Pratt and Worthington, 1990; Pratt, 1990; Fernandez and Santamarina, 2003). These travel times are collected along the length of the receiver boreholes for each shot position, providing more spatial coverage than the standard crosshole test. By varying the depth of the seismic source, a dense network of overlapping raypaths is obtained (Figure 2-7c). The composite travel times are then used to reconstruct a highly accurate velocity tomogram of the space between the boreholes. This tomogram can then be used to identify anomalies and individual velocity layers.

Advantages

- Source and receivers are placed close to the material to be evaluated, thus enhancing resolution where inclusions and anomalies may not be properly resolved using surface-based geophysical methods.
- Crosshole tomography is able to produce high-resolution 2-D velocity tomograms between boreholes for P-, SV- and SH-waves, although not simultaneously.

Disadvantages

- The main disadvantage of crosshole testing is the time and cost associated with drilling boreholes.

2.4.2 Downhole Method

The downhole method measures the travel time of compressional and shear waves between a source on the surface and receivers within a borehole (ASTM D7400; Mok et al., 1988). In this method, a geophone or a string of geophones receives energy

from waves that are measured on a seismograph. The downhole method is based on the assumption that the first-arrival signal at a given depth is from the direct wave, since the waves travel almost vertically. Once travel distances have been determined, wave velocities are then calculated from the corresponding travel times. Travel distances are typically based on the assumption that raypaths between the source and receivers are straight, although advanced analysis can account for curved raypaths as well. Figure 2-7b presents a conventional test setup used in a downhole seismic survey.

Advantages

- The downhole method requires only one borehole, and thus is more cost-effective than the crosshole method.
- The downhole method can create both P- and SH-wave velocity profiles.
- This method does not require that the layer velocities increase with depth.

Disadvantages

- This method obtains only 1-D seismic wave velocity profiles.
- Resolution of the inverted wave velocities decreases as depth increases.

2.4.3 Suspension P-S Velocity Logging

Suspension P-S velocity logging is a relatively new method for determining seismic wave velocity profiles in both soil and rock formations (Kitsunezaki, 1980; Nigbor and Imai, 1994). The wave velocities are usually measured in a single, fluid-filled borehole.

A typical logging system uses a probe, consisting of a pressure source and two receivers suspended by a cable (Figure 2-8). The probe is lowered into the borehole to a specified depth, where the pressure source generates a pressure wave in the borehole fluid. The pressure wave is converted to seismic waves (P- and S-waves) at

the borehole wall. Along the wall at each receiver location, the P- and S-waves are converted back to pressure waves in the fluid and detected by the hydrophones. The average compressional and shear wave velocities of the surrounding material can be determined from the travel times between the two receivers. The pressure source generates pressure waves at each depth interval until waves are measured along the entire length of the borehole.

Advantages

- The wireline allows for penetration to depths of hundreds of meters.
- This method can reliably obtain both P- and SH-wave velocity profiles in either cased or uncased boreholes.
- This method can resolve thin and soft layers.

Disadvantages

- This method obtains only 1-D seismic wave velocity profiles.

2.4.4 Full Waveform Sonic Logging

In a full waveform sonic logging survey, the data acquisition method is similar to the suspension logger, as both the pressure source and the receivers are placed in the same borehole (Hornby, 1989; Chabot, 2003). However, the full waveform sonic logging tool uses a string of receivers located at different offsets along the body of the well-logging tool (Figure 2-9). As the tool is moved upwards along the borehole, it repeatedly logs the formations surrounding the borehole.

The complete signal of acoustic pressure is monitored by the hydrophone at fixed sampling rates for a certain length of time. The resulting recorded signal is called a full waveform, which is recorded at each receiver. Each full waveform contains several pressure signifiers, such as direct or fluid waves, P- and S-head waves, pseudo-

Rayleigh waves, Stoneley waves, normal modes, and converted modes. Full waveforms are then processed and analyzed to investigate the structural properties of the formations surrounding the borehole.

Advantages

- Data processing involves analysis of full waveforms, as opposed to the first-arrival signals used in P-S suspension logging.

Disadvantages

- Migration-type analysis results in only a qualitative description of the formations surrounding the borehole.

2.5 Initiation of the Current Research

As discussed above, characterizing spatial variations in rock formations is essential for the design of drilled shaft foundations in karst terrain where subsurface conditions are often highly variable.

Crosshole tomography is well known for its capability to produce reliable 2-D velocity tomograms of the material between boreholes (Pratt and Worthington, 1990; Pratt, 1990). However, reconstructed velocity tomograms fail to characterize the existence of isolated anomalies, such as voids or low-velocity inclusions, in planes outside of where the boreholes are located. In order to detect such anomalies, multiple receiver holes must be drilled around the source hole, and then crosshole tomography must be applied between each source hole and the individual receiver holes. This task substantially increases the cost of conducting the crosshole test. Therefore, building on the work of Tran et al. (2011), the current study aimed to use only one borehole, while still characterizing 2-D and 3-D velocity variations in the surrounding material.

Previous studies have employed the suspension logging method for obtaining reliable 1-D S-wave velocity profiles versus depth. Kalinski (1998) attempted to apply

the SASW inside a borehole in order to obtain lateral variation measurements. Cheng (1997) found that the cylindrical geometry of the borehole significantly affected the dispersive characteristics of surface waves and that appropriate numerical models were needed to accurately simulate the experimental data. By assuming that the formation surrounding the borehole was cylindrically multilayered, 1-D S-wave velocity profiles of a few inches into the radius could be inverted. Thus, as an alternative to crosshole tomography, Kalinski (1998) proposed that the borehole SASW method be used in conjunction with suspension logging to derive a high-resolution S-wave velocity profile of the subsurface. However, it must be noted that 1-D vertical variation plus 1-D lateral variation is not equal to 2-D variation. More importantly, an isolated anomaly cannot be characterized using this combined method.

Recent advances in borehole acoustic logging use the acquired full waveforms to look deep into the borehole walls. Hornby (1989), Fortin et al. (1991), Coates et al. (2000), and Chabot (2003) used an acoustic well-logging tool, equipped with monopole/dipole sources and a string of receivers suspended in a fluid-filled borehole. These tools, combined with some advanced signal processing flows were used to image scattered energy originating from acoustic impedance contrasts from beyond the borehole wall. Those contrasts could be interpreted as structural changes, providing improved knowledge of subsurface spatial variations not easily captured through surface seismic analysis. However, it must be noted that the migrated image does not provide any quantitative correlation between impedance contrasts and engineering design parameters of interest (e.g., S-wave velocity).

FWI, a combination of migration and tomography (Mora, 1989), offers a new angle on imaging, as it uses only one borehole to characterize 2-D and 3-D velocity variations in rock formations. The proposed experimental setup uniformly mounts a linear array of three-component transducers along the vertical borehole wall (Figure 2-10). Similar to the MASW or seismic refraction conducted on the ground surface, this method uses an appropriate seismic source – either mechanical, piezoelectric, or electromagnetic – to generate a tri-axial shot gather. With an array of receivers fully coupled to the wall, the seismic source can be moved up and down to acquire multiple shot gathers. Ideally, this method creates a 3-D scan of material along and around the borehole by rotating the receiver array circumferentially inside the borehole. Alternatively, a 3-D receiver array can be placed at the beginning of the test.

Subsequent chapters will present details of numerical formulations and applications.

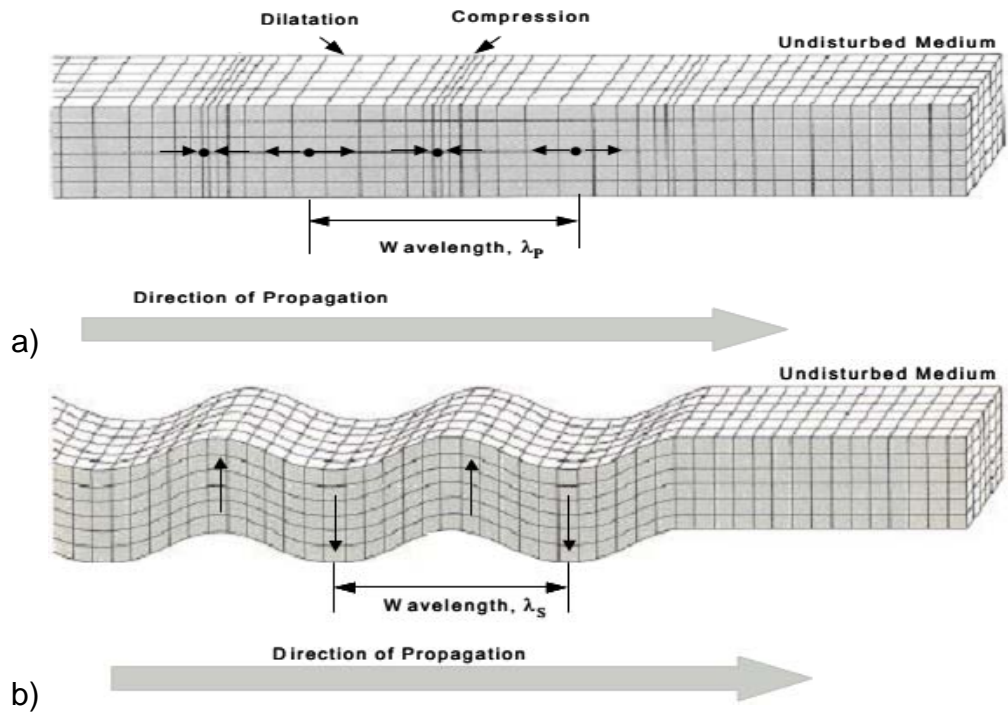


Figure 2-1. Body waves: a) Compressional waves and b) Shear waves (from Stokoe and Santamarina, 2000)

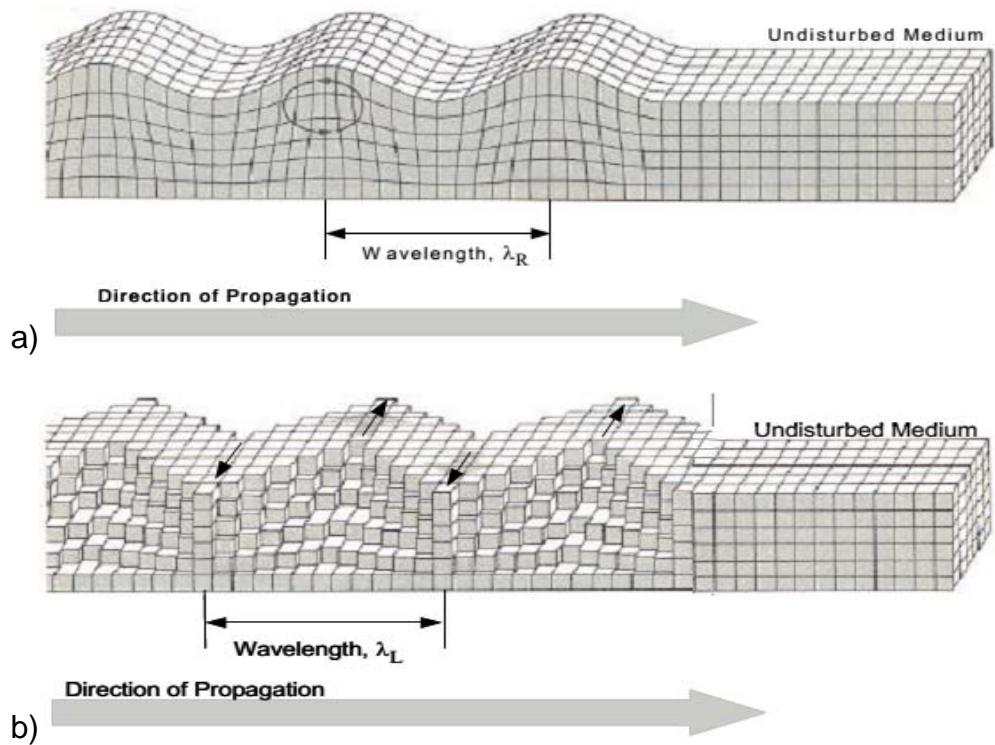


Figure 2-2. Surface waves: a) Rayleigh waves and b) Love waves (from Stokoe and Santamarina, 2000)

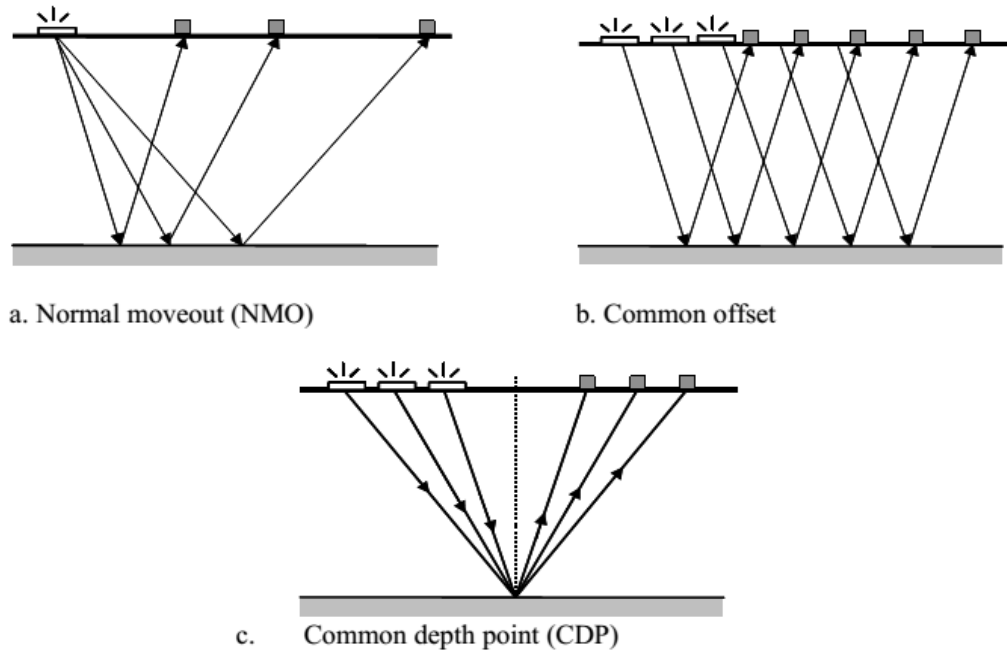


Figure 2-3. Field arrangement used in the seismic reflection method: a) Normal moveout, b) Common offset, and c) Common depth point (from Stokoe and Santamarina, 2000)

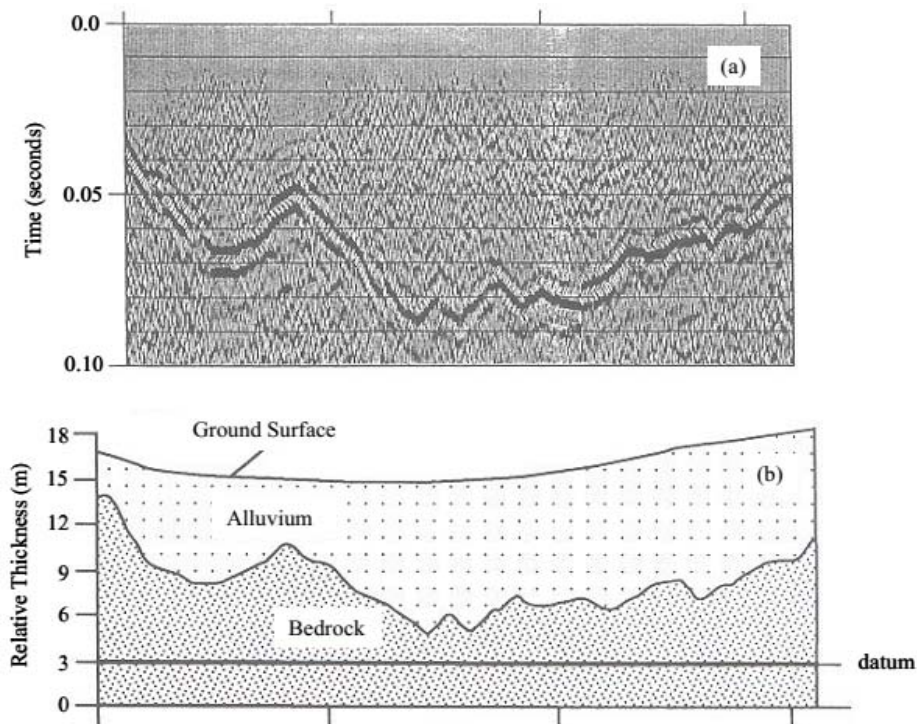
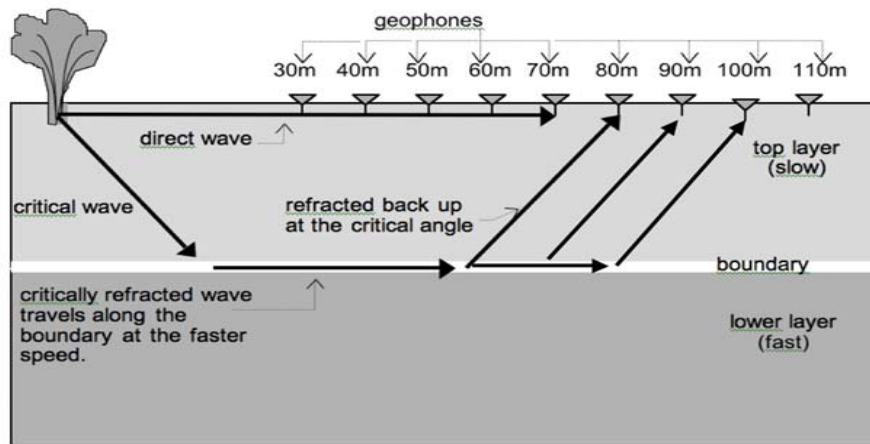
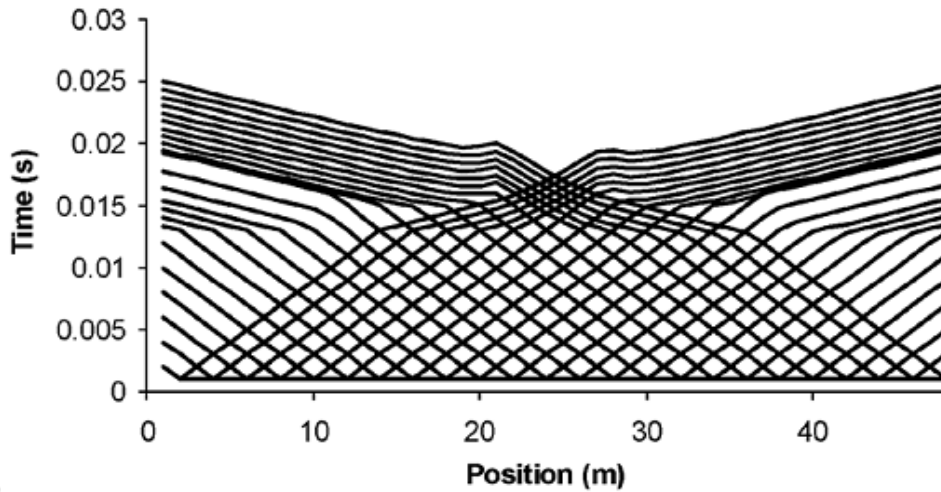


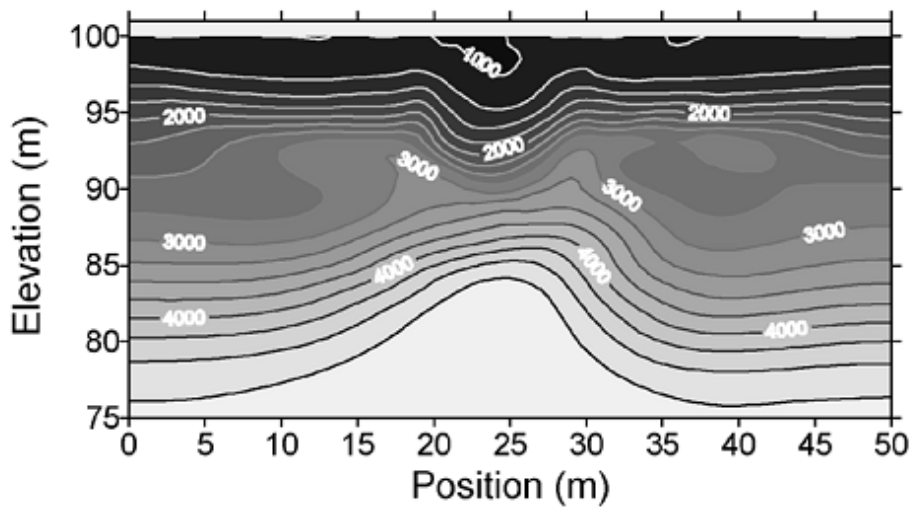
Figure 2-4. Interpretation of a seismic reflection test: a) Time-migrated cross-section and b) Interpreted geologic profile (from NRC, 2000)



a)

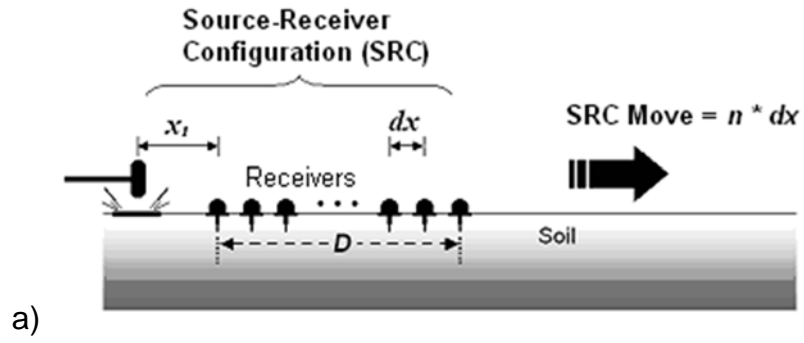


b)

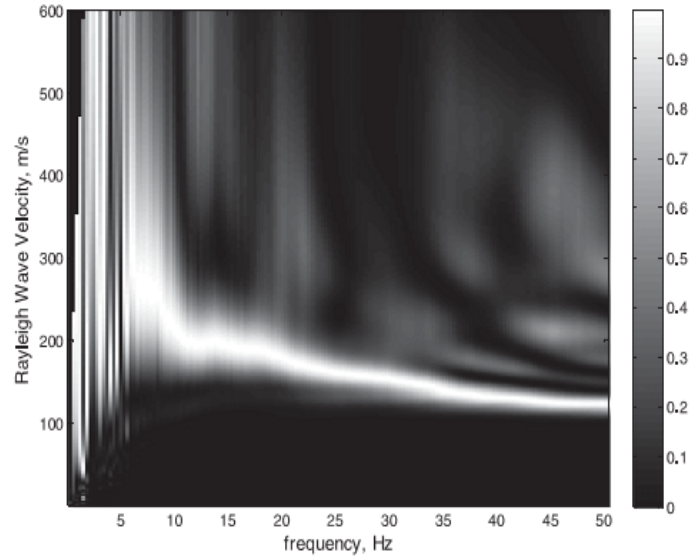


c)

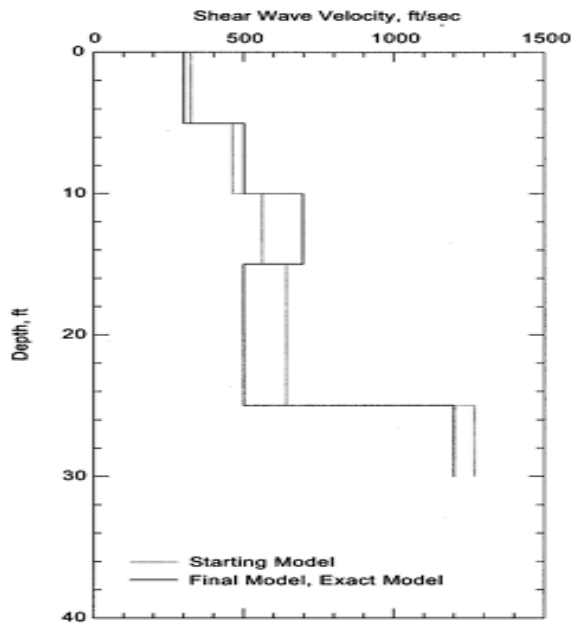
Figure 2-5. Seismic refraction method: a) Test configuration, b) Travel times, and c) Reconstructed P-wave velocity tomogram



a)

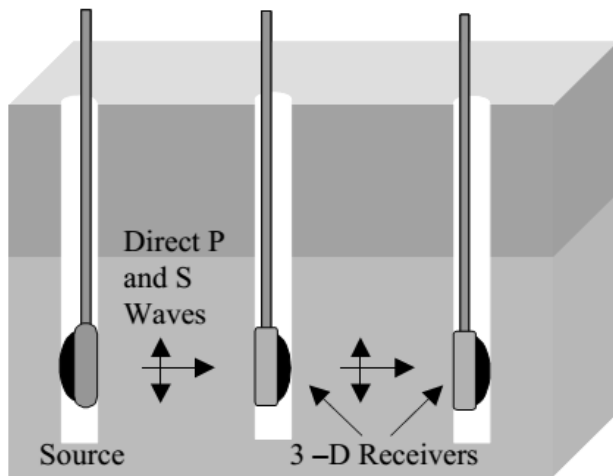


b)

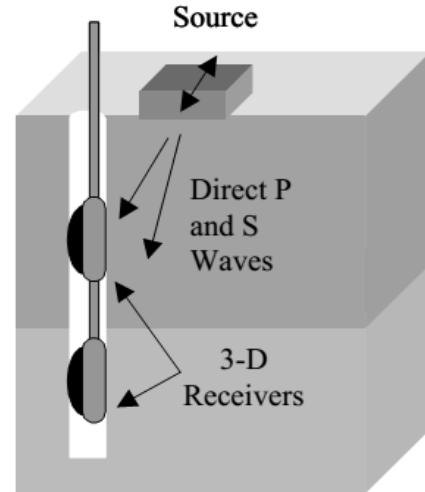


c)

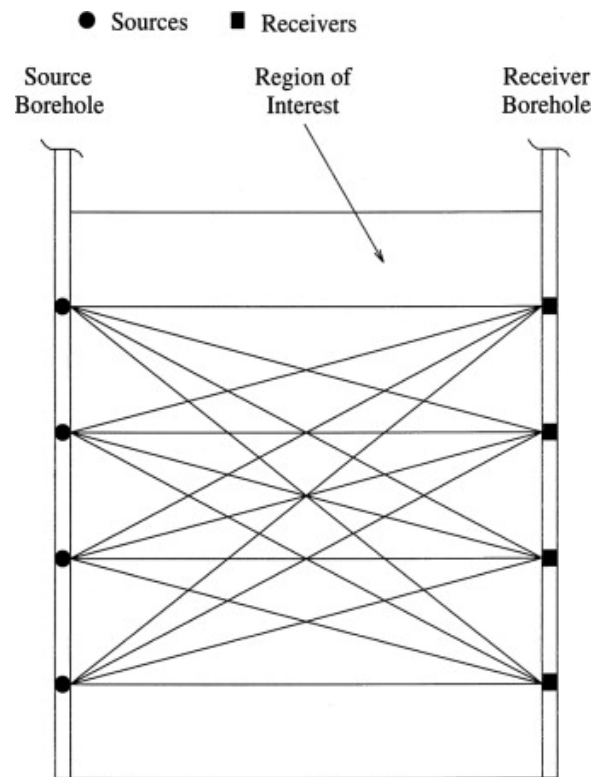
Figure 2-6. Surface wave method: a) Test configuration, b) Rayleigh wave dispersion, and c) Inverted shear wave velocity profile



a. Crosshole Testing



b. Downhole Testing



c) Crosshole Tomography

Figure 2-7. Crosshole and downhole methods: a) Crosshole testing, b) Downhole testing, and c) Crosshole tomography (from Stokoe and Santamarina, 2000)

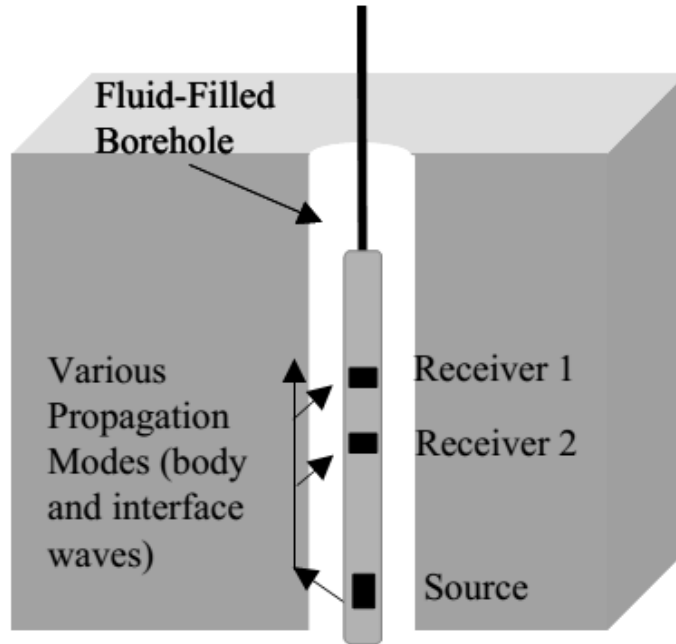


Figure 2-8. Test setup for the suspension P-S velocity logging (from Stokoe and Santamarina, 2000)

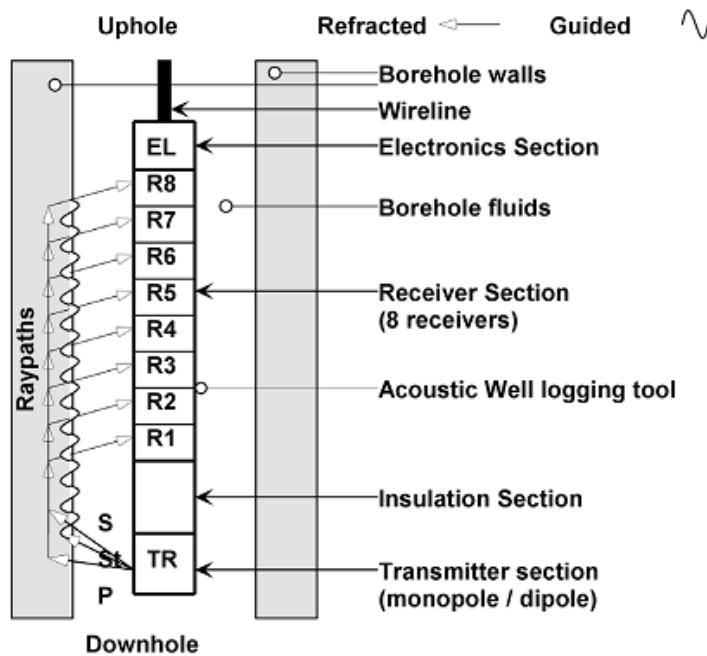
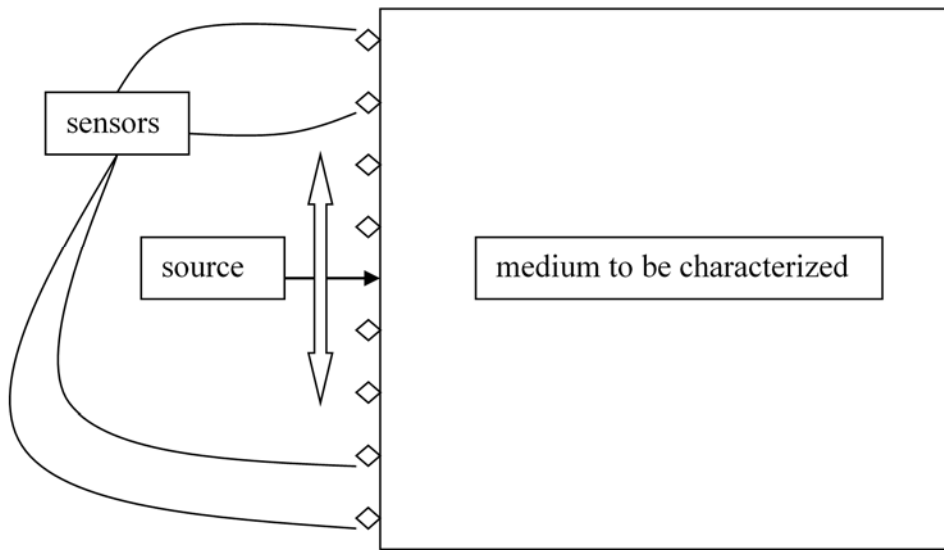
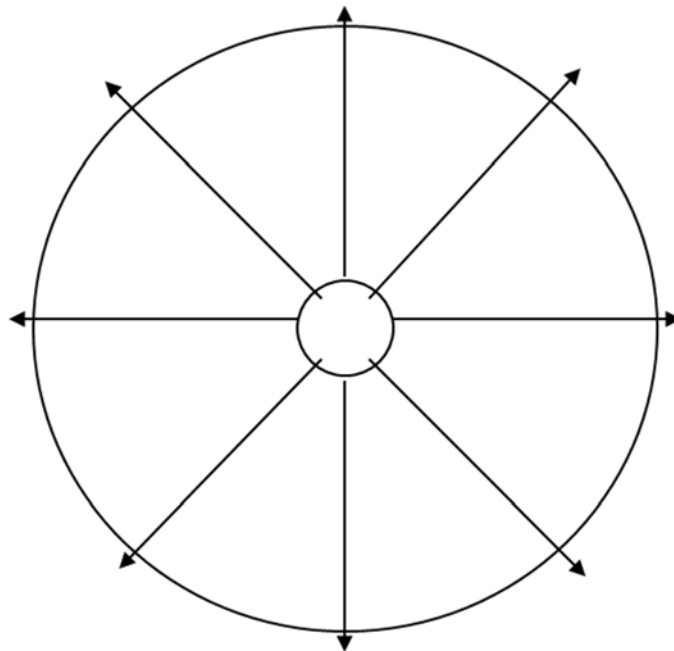


Figure 2-9. Test setup for the full waveform sonic logging (from Chabot, 2003)



a)



b)

Figure 2-10. Schematics of test setup for the proposed borehole-based FWI: a) Cross-sectional view and b) Top view with eight planes to be scanned

CHAPTER 3 FULL WAVEFORM INVERSION WITHIN A BOREHOLE

3.1 Introduction of Full Waveform Inversion

As discussed above, standard seismic methods use limited wavefield information, such as reflectivity (as in the seismic reflection and borehole acoustic logging methods), travel times (as in the seismic refraction, crosshole, and PS suspension logging methods), and phase velocity dispersion (as in the surface wave method). Therefore, the resulting capabilities of these methods are limited.

The theory of seismic FWI was formulated in the 1980s (Lailly, 1983; Tarantola, 1984); however, it was rarely used as computers at the time had limited power and memory. Recent advances in high-performance computers have generated considerable interest in applying FWI to exploration seismology, mainly for the purpose of reservoir characterization. Given the new capabilities of this method, civil engineering projects have recently begun using FWI for the purpose of site characterization (Tran and Hiltunen, 2012; Tran and McVay, 2012; Romdhane et al., 2011).

Seismic inversion is essentially equivalent to conducting migration and reflection tomography simultaneously (Mora, 1989). Major advantages of FWI are that it utilizes the amplitude and phase information of seismic wavefields, properly managing multipathing, mode conversion, and other complex wavefield phenomena (Virieux and Operto, 2009). In addition, FWI is largely automated, as opposed to requiring intense manual interpretation, and can be formulated in either time or frequency domain (Tarantola, 1984; Pratt et al., 1998). In a restrictive sense, FWI requires a complete recording of all wave paths – specifically, reflection, refraction, and multiples. In a less restrictive sense, FWI aims to identify Earth models that enable the production of

synthetics that mimic the complete observed data set (Plassix, 2008). Two key elements of FWI are an accurate and efficient forward model, and a repeatable and reliable inversion scheme.

It must be noted that the majority of seismic full waveforms are generated, recorded, and inverted from the ground surface, as this technique is the easiest and presents the most well-developed forward models (e.g., 2-D time domain finite difference solution). Although full waveforms are also logged using borehole acoustic techniques, FWI has never been attempted using this technique, as wave propagation inside a borehole is significantly more complicated than wave propagation from flat ground.

In the case of fluid-filled boreholes, an omnidirectional pressure source (monopole) creates a compressional wave pulse in the borehole fluid. This pulse propagates out into the formation, creating a disturbance around the borehole wall, and exciting compressional and shear waves in the formation (Schlumberger, 1997). As these waves propagate in the formation, they generate head waves in the borehole fluid, thus generating refracted arrivals. After the head waves, guided borehole waves arrive, followed by the Stoneley waves. The guided borehole waves are generated by reflections of source waves reverberating in the borehole (Schlumberger, 1997). The Stoneley waves travel more slowly than the fluid waves, and decay as they travel through the fluid-borehole interface away from the borehole. Far-field velocities are associated with geophysical parameters, while near-field velocities are associated with geomechanical properties (Chabot, 2003).

In the case of dry boreholes, an omnidirectional mechanical source creates compressional and shear waves that travel along and into the formation. Dispersive, Rayleigh-type surface waves develop in the borehole annulus. The phase and group velocities depend on the ratio between the wavelength and the size of the borehole (Biot, 1952).

This chapter details the numerical implementations of FWI within a dry borehole.

3.2 Forward Problem

The prediction of observations, given the parameters defining the model, constitutes the forward problem. In the context of seismic FWI, forward modeling involves solving the governing wave equations, thereby predicting the particle responses at observational points.

3.2.1 Theoretical Derivation

Wave propagation in cylindrical cavities is governed by the wave equation (Biot, 1952), which can be solved by transforming the data into cylindrical coordinates and treating the equation as an axisymmetric problem. This process requires solving the following equations:

$$\frac{\partial^2 \phi}{\partial r^2} + \frac{1}{r} \frac{\partial \phi}{\partial r} + \frac{\partial^2 \phi}{\partial z^2} = \frac{1}{V_p^2} \frac{\partial^2 \phi}{\partial t^2} \quad (3-1)$$

$$\frac{\partial^2 \psi}{\partial r^2} + \frac{1}{r} \frac{\partial \psi}{\partial r} - \frac{\psi}{r^2} + \frac{\partial^2 \psi}{\partial z^2} = \frac{1}{V_s^2} \frac{\partial^2 \psi}{\partial t^2} \quad (3-2)$$

where ϕ is compressional potential function, ψ is shear potential function, r is radial distance from the cavity center, z is axial distance, t is time, V_p is compressional wave

velocity, and V_s is shear wave velocity. For non-attenuated waves propagating in the axial direction, the solutions to the above equations are as follows:

$$\phi = \phi_0 K_0(mr) \cos(kz - \omega t) \quad (3-3)$$

$$\psi = \psi_0 K_1(pr) \sin(kz - \omega t) \quad (3-4)$$

where ϕ_0 and ψ_0 are constants, k is wave number ($k = 2\pi / \lambda$), ω is angular frequency ($\omega = 2\pi f$), K_0 is modified Bessel function of the second kind of zero order, and K_1 is modified Bessel function of the second kind of first order. The parameters m and p are defined as follows:

$$m = k \sqrt{1 - \left(\frac{V_r}{V_p}\right)^2} \quad (3-5)$$

$$p = k \sqrt{1 - \left(\frac{V_r}{V_s}\right)^2} \quad (3-6)$$

where V_r is Rayleigh wave velocity.

Given the boundary conditions of zero normal and shear stress at the cavity wall, Equations (3-3) and (3-4) are used to derive an implicit relationship between V_r and λ :

$$4(1 - \xi_1^2) \left[\frac{1}{pr_0} + \frac{K_0(pr_0)}{K_1(pr_0)} \right] - \frac{2(2 - \xi_1^2)\sqrt{1 - \xi_2^2}}{mr_0} - \frac{(2 - \xi_1^2)^2 K_0(mr_0)}{\sqrt{(1 - \xi_1^2)} K_1(mr_0)} = 0 \quad (3-7)$$

where r_0 is cavity radius, $\xi_1 = V_r / V_s$, and $\xi_2 = V_r / V_p$. Figure 3-1 illustrates this relationship as derived from Equation (3-7) with the Poisson's ratio being 0.25.

3.2.2 Finite Element Modeling

Analytical solutions can only be obtained for simple models (e.g., a cylindrical cavity in a homogeneous medium as illustrated above). Numerical approximations are

required to handle complex geometry, loading, boundary conditions, and material properties. A number of numerical methods are commonly used to generate synthetic seismograms, such as the method based on ray theory, the finite difference method, and the finite element method.

When developing a feasibility study on characterizing the spatial variation of material using FWI within a borehole, it is beneficial to determine the viability of the whole system before developing a specialized forward modeling code. Therefore, this study used ABAQUS – a commercially available, general-purpose finite element package – to model the propagation of seismic waves inside a borehole. Specifically, an axisymmetric borehole model was formulated as the forward model (Figure 3-2). The model was 4 m long, with a 2 m radial extension and a 10 cm diameter. The model was uniformly discretized into 36 cells (9 by 4) measuring 0.5 m by 0.5 m each. Material properties were assigned to each cell independently, including density, Young's modulus, and Poisson's ratio. A 6-node modified quadratic axisymmetric triangular element was used in the explicit dynamics analysis.

3.2.2.1 Spatial-temporal discretization

In wave propagation problems, element dimensions are chosen with respect to the highest frequency for the lowest wave velocity. Element dimensions that are too large will filter high frequencies, whereas very small element dimensions can introduce numerical instability as well as require considerable computational resources (Zerwer et al., 2002). An approximate element dimension is calculated using the following equation:

$$g \leq \alpha \cdot \lambda_{\min} \quad (3-8)$$

where

$$\lambda_{\min} = \frac{V_{\min}}{f_{\max}} \quad (3-9)$$

where λ_{\min} is minimum wavelength, V_{\min} is minimum wave velocity in the model, and f_{\max} is maximum frequency of interest. The constant α must be less than 0.5 because of the Nyquist limit, and the actual value depends on whether the mass matrices are consistent ($\alpha = 0.25$) or lumped ($\alpha = 0.2$).

The time increment must be carefully chosen to maintain numerical accuracy and stability. Numerical instability may cause the solution to diverge if the time increment is too large. Conversely, a very short time increment can cause spurious oscillations, known as the Gibb's phenomenon. The calculation of the time increment depends on the element dimension computed with the following expression:

$$\frac{1}{10} \frac{g}{(V_p)_{\max}} \leq \Delta t \leq \frac{g}{(V_p)_{\max}} \quad (3-10)$$

where Δt is time increment, g is element dimension, and $(V_p)_{\max}$ is maximum compressional wave velocity in the model. Although the time increment incorporates the spatial Nyquist limit, it must also entail the temporal Nyquist limit, as expressed in the following equation:

$$\Delta t \leq \frac{1}{2f_{\max}} \quad (3-11)$$

3.2.2.2 Numerical Implementation

The explicit dynamics analysis procedure in ABAQUS/Explicit is based on the implementation of an explicit integration rule and the use of lumped mass matrices. The

explicit central difference integration rule is used to integrate the following equations of motion:

$$v^{i+1/2} = v^{i-1/2} + \frac{\Delta t^{i+1} + \Delta t^i}{2} a^i \quad (3-12)$$

$$u^{i+1} = u^i + \Delta t^{i+1} v^{i+1/2} \quad (3-13)$$

where u is displacement, v is velocity, and a is acceleration. The superscript i refers to the increment number, while $i+1/2$ and $i-1/2$ refer to mid-increment values. The central difference integration operator is explicit in that the kinematic state can be advanced using known values from previous increments. The use of lumped element matrices is key to the computational efficiency of the explicit procedure because the inversion of the mass matrix used to compute the accelerations at the beginning of the increment is triaxial, as expressed in the following equation:

$$a = M^{-1}(F^i - I^i) \quad (3-14)$$

where M is diagonal lumped mass matrix, F is applied load vector, and I is internal force vector. The explicit procedure requires no iterations and no tangent stiffness matrix.

The mean velocities $v^{i+1/2}$ and $v^{i-1/2}$ require special treatment under initial conditions and certain constraints. The state velocities are stored as a linear interpolation of the mean velocities:

$$v^{i+1} = v^{i+1/2} + \frac{1}{2} \Delta t^{i+1} a^{i+1} \quad (3-15)$$

The initial values of velocity and acceleration are set to zero unless specified otherwise. The following condition is asserted:

$$v^{+1/2} = v^0 + \frac{1}{2} \Delta t^1 a^0 \quad (3-16)$$

Substituting this expression for $v^{i+1/2}$ in Equation (3-12) yields the following solution:

$$v^{-1/2} = v^0 - \frac{1}{2} \Delta t^0 a^0 \quad (3-17)$$

3.3 Inverse Problem

3.3.1 Introduction

The inverse problem refers to using actual measurements to estimate the model parameters characterizing the system under investigation. The goal is to derive an appropriate model that minimizes the error between measurement and estimation. In the context of seismic FWI, measurement refers to the observed wavefield recorded in each receiver, while estimation refers to the synthetic wavefield generated by the forward operator for the most geologically meaningful model.

In fitting a function $y_{est}(t; p)$ of an independent variable t and a vector of n parameters p to a set of data points (t_i, y_i) , it is customary and convenient to minimize the sum of the weighted squares of the errors (or weighted residuals) between the measured data $y(t_i)$ and the curve-fitting function $y_{est}(t; p)$. This scalar-valued fitness measure (objective function) is called the chi-squared error criterion, or the L2 norm:

$$\chi^2(p) = \frac{1}{2} \sum_{i=1}^m \left[\frac{y(t_i) - y_{est}(t; p)}{w_i} \right]^2 = \frac{1}{2} (y - y_{est}(p))^T W (y - y_{est}(p)) = \frac{1}{2} y^T W y - y^T W y_{est} + \frac{1}{2} y_{est}^T W y_{est} \quad (3-18)$$

where w_i is a measure of the error in measurement $y(t_i)$, and the weighting matrix W is diagonal with $W_{ii} = 1/w_i^2$. The minimization of χ^2 is carried out iteratively. The goal of each iteration is to find a perturbation h to the parameter p that reduces χ^2 .

Inverse problem solving is essentially implemented as a process of numerical optimization. In general, numerical optimization techniques can be classified into two

broad categories: local optimization techniques and global optimization techniques. Global optimization techniques, such as simulated annealing (Ingber, 1989) and genetic algorithm (Sen and Stoffa, 1992), can be used for seismic waveform inversion. As compared to local optimization techniques, these techniques require neither a good starting model for convergence nor the calculation of Jacobian and Hessian matrices for model updates. However, since effective sampling of the model parameter space requires a sufficiently large number of forward calculations, these optimization techniques are not particularly efficient for 2-D/3-D parameter estimation problems. On the other hand, local optimization techniques, such as the conjugate-gradient method (Mora, 1987; Tarantola, 1987) and the Gauss-Newton method (Sheen et al., 2006), are historically more widely implemented for seismic waveform inversion. Local optimization techniques attempt to find a local minimum by searching along the downhill direction. Therefore, these methods do not guarantee that the local minimum is the needed global minimum, unless, in rare cases, the starting model is in the vicinity of the global minimum. Nonetheless, in the current implementation of FWI within a borehole, the Gauss-Newton method was chosen for the relatively straightforward implementation, fast convergence property, and a record of successful application (Pratt et al., 1998; Sheen et al., 2006). The requirement of constructing a good starting model was circumvented by a multistage approach described below.

3.3.2 Gauss-Newton Method

The Gauss-Newton method is an iterative technique for solving nonlinear least-squares problems. This method assumes that the objective function and its first and second partial derivatives with respect to model parameters are continuous. In addition,

the objective function is assumed to be approximately quadratic in the parameter space near the optimal solution.

Functions evaluated with perturbed model parameters may be locally approximated through a first-order Taylor series expansion:

$$y_{est}(p+h) \approx y_{est}(p) + \left[\frac{\partial y_{est}}{\partial p} \right] h = y_{est} + Jh \quad (3-19)$$

where J is the Jacobian matrix, the first partial derivative with respect to model parameters. Substituting the approximation for the perturbed function, $y_{est} + Jh$, for y_{est} in Equation (3-18) results in the following equation:

$$\chi^2(p+h) \approx \frac{1}{2} y^T W y + \frac{1}{2} y_{est}^T W y_{est} - \frac{1}{2} y^T W y_{est} - (y - y_{est})^T W J h + \frac{1}{2} h^T J^T W J h \quad (3-20)$$

Equation (3-20) implies that χ^2 is approximately quadratic in the perturbation h , and that the Hessian matrix of the chi-squared fit criterion, the second partial derivative with respect to model parameters, can be approximated by $J^T W J$.

The perturbation h that minimizes χ^2 is found by enforcing $\partial \chi^2 / \partial h = 0$:

$$\frac{\partial}{\partial h} \chi^2(p+h) \approx -(y - y_{est})^T W J + h^T J^T W J \quad (3-21)$$

The resulting equation for the Gauss-Newton perturbation is as follows:

$$[J^T W J] h_{gn} = J^T W (y - y_{est}) \quad (3-22)$$

The model parameters, p , then update as follows:

$$p^{n+1} = p^n + [J^T W J]^{-1} J^T W (y - y_{est}^n) \quad (3-23)$$

In the current implementation, the Jacobian matrix is numerically approximated using finite differences:

$$J_{ij} = \frac{\partial(y_{est})_i}{\partial p_j} = \frac{y_{est}(t_i; p + \delta p_j) - y_{est}(t_i; p)}{\|\delta p_j\|} \quad (3-24)$$

where J is the Jacobian matrix, $y_{est}(t_i; p + \delta p_j)$ is estimation of the perturbed model, $y_{est}(t_i; p)$ is estimation of the current model, and $\|\delta p_j\|$ is absolute value of perturbation of the j -th model parameter.

3.3.3 Regularized Gauss-Newton Method

Many inverse problems are mathematically ill-posed because they operate with insufficient data. The inversion – if at all possible – would unevenly magnify noise in the solution, particularly on values of the model parameters that are least constrained by the data (Santamarina and Fratta, 2005). Regularization is a technique for making inverse problems well-posed by adding bias to the solution, such as assuming a smooth variation among model parameters.

Similarly, in the application of the Gauss-Newton method to seismic waveform inversion, regularization is particularly important for stabilizing the system and incorporating *a priori* information into the problem (Tarantola, 1987). The current study discards the measurement error (synthetic data) and follows the approach presented by Sheen et al. (2006).

The regularized misfit function S can be defined as follows:

$$S(p) = S_d(p) + \lambda S_p(p) \quad (3-25)$$

where S_d is the data objective function (as in Equation 3-18), S_p is the model objective function that contains the *a priori* information of the model, and λ is a scalar (between 0

and 1) that controls the relative importance of S_p . The model objective function can be defined as follows:

$$S_p(p) = \frac{1}{2} \|L\Delta p\|^2 \quad (3-26)$$

Ignoring the measurement error changes Equation (3-23) to the following:

$$p^{n+1} = p^n + [J^T J + \lambda L^T L]^{-1} J^T (y - y_{est}^n) \quad (3-27)$$

Note that if $L = I$, it represents the damped least-squares solution (Levenberg, 1944; Marquardt, 1963), which corresponds to the zeroth-order Tikhonov regularization, where the L2 norm of model parameters is minimized (Aster et al., 2005). If L is a discrete spatial differential operator, it resembles Occam's inversion (Constable et al., 1987), which corresponds to the second-order Tikhonov regularization, where the spatial variation among model parameters is minimized (Aster et al., 2005). Combined use of these two regularization techniques yields the following regularized Gauss-Newton formula:

$$p^{n+1} = p^n + \alpha^n [J^T J + \lambda_1 P^T P + \lambda_2 I^T I]^{-1} J^T (y - y_{est}^n) \quad (3-28)$$

where $\lambda_1 = 5e-6$ and $\lambda_2 = 5e-4$ are used, α is a step length, I is the identity matrix, and P is the roughening matrix, the elements of which are determined using the following discrete 2-D Laplacian operator:

$$P_i \Delta p = (\Delta p_i)^E + (\Delta p_i)^W + (\Delta p_i)^N + (\Delta p_i)^S - 4(\Delta p_i) \quad (3-29)$$

where the superscripts E , W , N , and S refer to four neighbors of the i -th model parameter p_i , and P_i refers to the i -th row of the matrix, P , whose element is either 1, -4, or 0.

A constant step length of $\alpha = 0.5$ is taken through all iterations for simplicity. However, an optimal value of the step length can be determined by a linearized approach as follows (Sheen et al., 2006):

$$\alpha^n \cong \frac{[\mathbf{J}^T \mathbf{g}^n]^T [y - y_{est}^n]}{[\mathbf{J}^T \mathbf{g}^n]^T [\mathbf{J}^T \mathbf{g}^n]}, \text{ where } \mathbf{g}^n = [\mathbf{J}^T \mathbf{J} + \lambda_1 \mathbf{P}^T \mathbf{P} + \lambda_2 \mathbf{I}^T \mathbf{I}]^{-1} \mathbf{J}^T (y - y_{est}^n) \quad (3-30)$$

3.4 Practical Strategies for FWI

Inverse problems are generally very difficult. The difficulties stem from three issues: existence, uniqueness, and instability (Aster et al., 2005). First, inverse problems may not have a solution due to inexact physics in the forward model or noise in the data. Second, there may be an infinite number of models that can fit the data equally well. Lastly, inverse problems may be ill-posed or ill-conditioned, where the solution is very sensitive to small changes in the data. In the synthetic model studies, however, the solution always exists, and the issues of uniqueness and instability can be largely solved using regularization. Nonetheless, another important issue exists: convergence. Depending on the initial model, local optimization techniques may converge to a local minimum, or may not converge at all.

3.4.1 Frequency Filtering

Seismic FWI applied to surface data is highly nonlinear, and tends to converge to a local minimum if the starting model is not in the vicinity of the global minimum. Therefore, a good initial model is often required to avoid local minima; however, obtaining a suitable initial model is often difficult if no *a priori* information is available. To mitigate nonlinearity and loosen the initial model requirement, a multiscale approach is often utilized in either time domain (Bunks et al., 1995) or frequency domain (Sirgue and Pratt, 2004). This multiscale approach builds a background model by inverting the low-

frequency component, and then increases the resolution by gradually adding high-frequency components in the data. The degree of nonlinearity, or the multimodal distribution of the misfit function with respect to the model parameters, depends on the frequency content of seismic data. The misfit (objective) function is more linear at low frequencies than at high frequencies. For this reason, inversion processes that sequentially proceed from low to high frequencies are more likely to reach the global minimum than processes that start with high-frequency raw data.

To illustrate the effect of frequency filtering, a series of low-pass filters was applied to raw data (Figure 3-4). Each subpart of the Figure displays the time signal and the associated frequency content. It should be noted that, in Figure 3-4a, the frequency spectrum in the raw data is being dominated by three peaks, approximately centered at 500, 1500, and 2500 Hz. After first-level filtering, the highest frequency peak disappears, and only the first two peaks remain in the spectrum (Figure 3-4b). Applying another lower-pass filter leaves only one peak in the spectrum (Figure 3-4c).

3.4.2 Time Windowing

As discussed below, synthetic wavefields generated within a borehole are significantly more complicated than wavefields generated from the ground surface. Thus, problems can become extremely nonlinear when FWI is applied to borehole data. To further reduce the nonlinearity, this study proposes starting with a short time window at a low-frequency band. After some iterations, higher frequencies are incorporated in the inversion with the same time window. Then, the inversion proceeds with longer time windows, followed by similar filtering strategies, until the full data set has been considered. Figure 3-5 illustrates this windowing technique. For the waveform shown in Figure 3-4c, the first window was clipped at 2.5 ms, and the second window was clipped

at 5 ms, with the full window corresponding to the entire length of the signal. Gradually increasing the time window and frequency bandwidth applied to the residual enabled a radial velocity update and reduced the possibility of the misfit function being stuck at local minima. Implemented in this way, the proposed inversion scheme essentially uses the *a priori* information continuously gained from previous iterations, and steers the model update towards the global minimum. The proposed inversion scheme is illustrated in a flowchart in Figure 3-3.

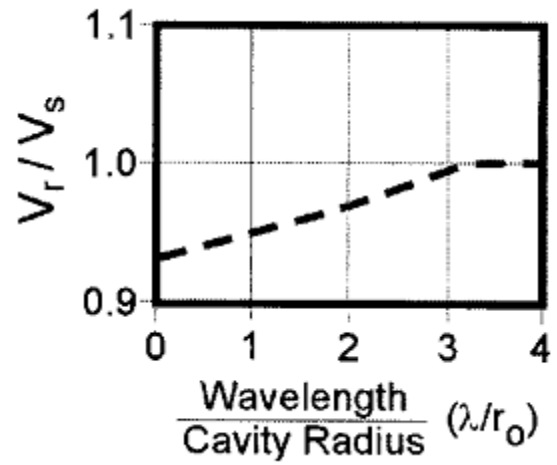


Figure 3-1. Dispersion of an axially propagating surface wave in a borehole with Poisson's ratio of 0.25 (from Kalinski, 1998)

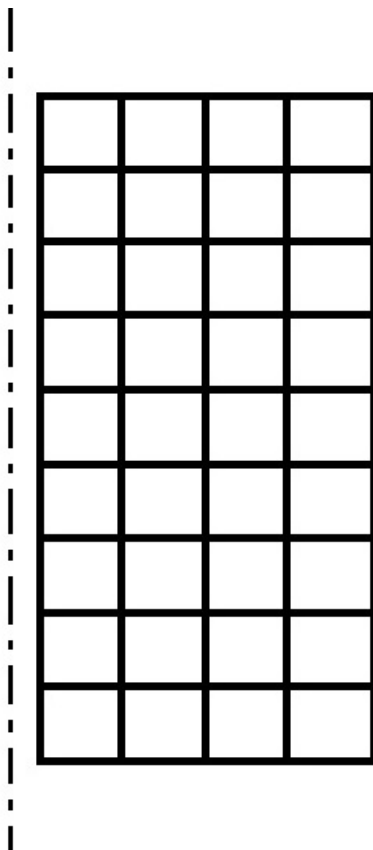


Figure 3-2. Discretization of an axisymmetric borehole model

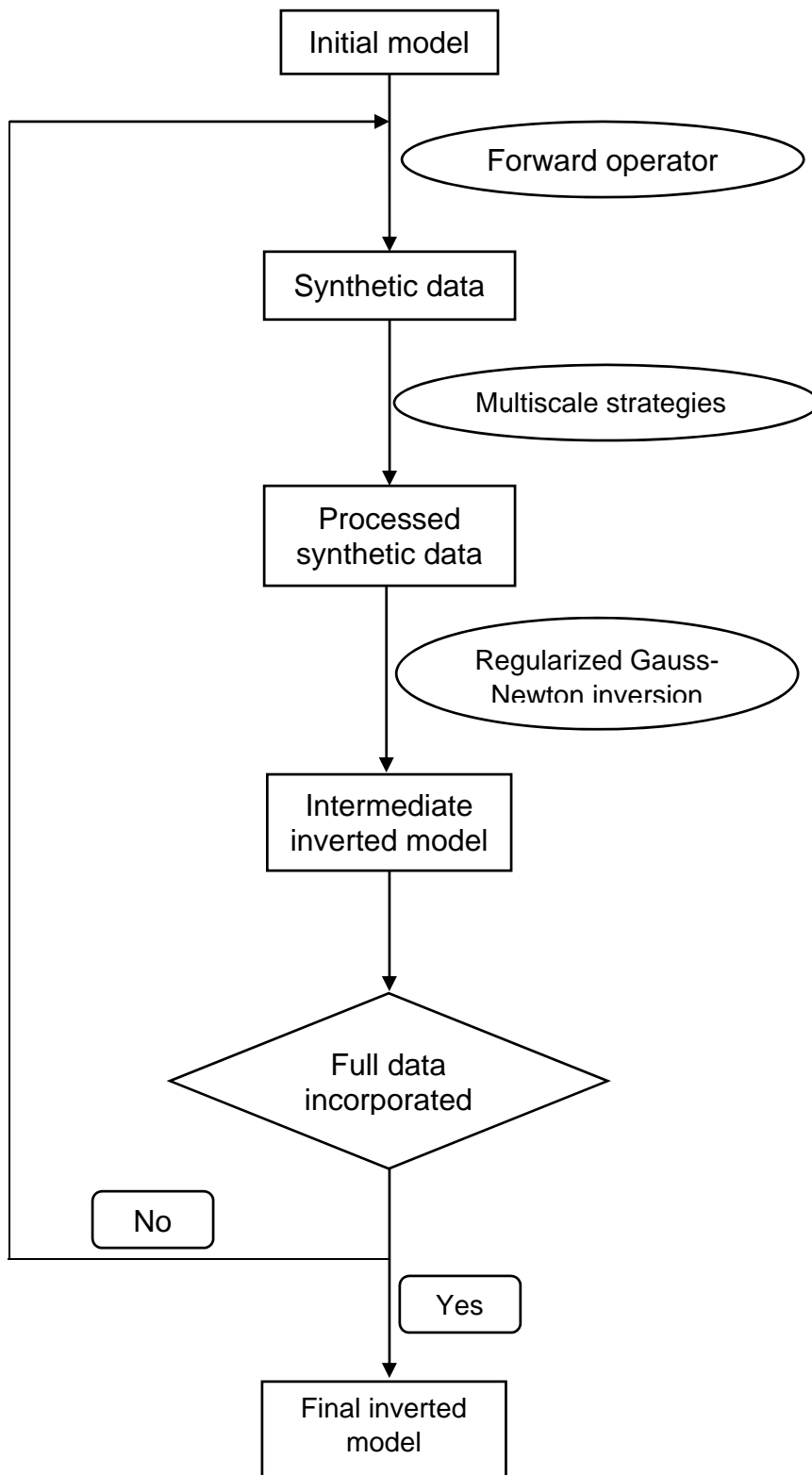
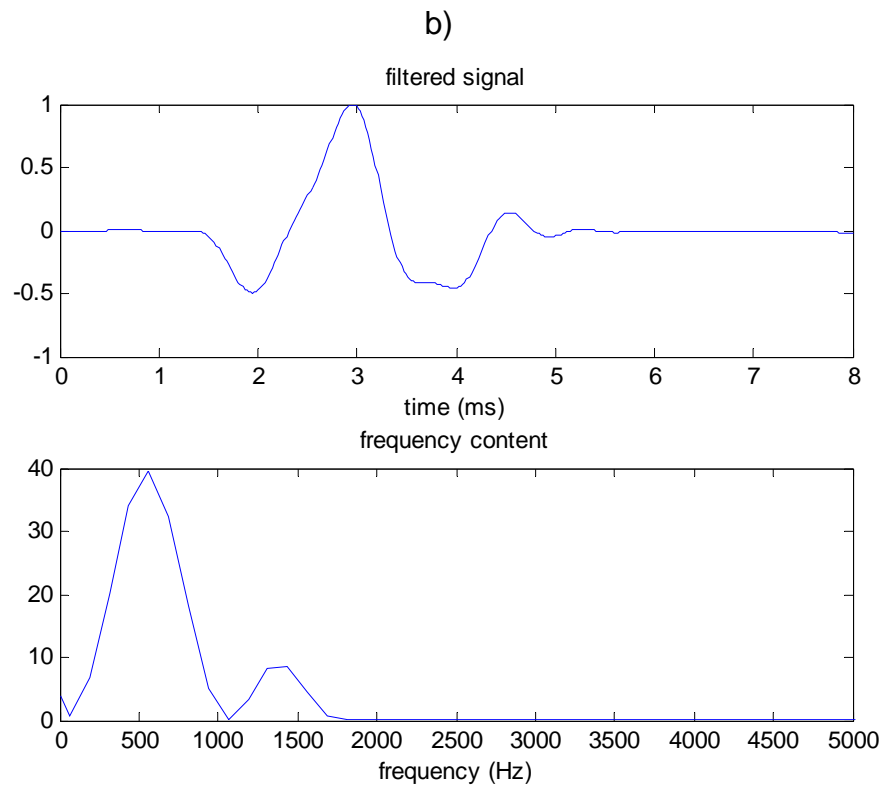
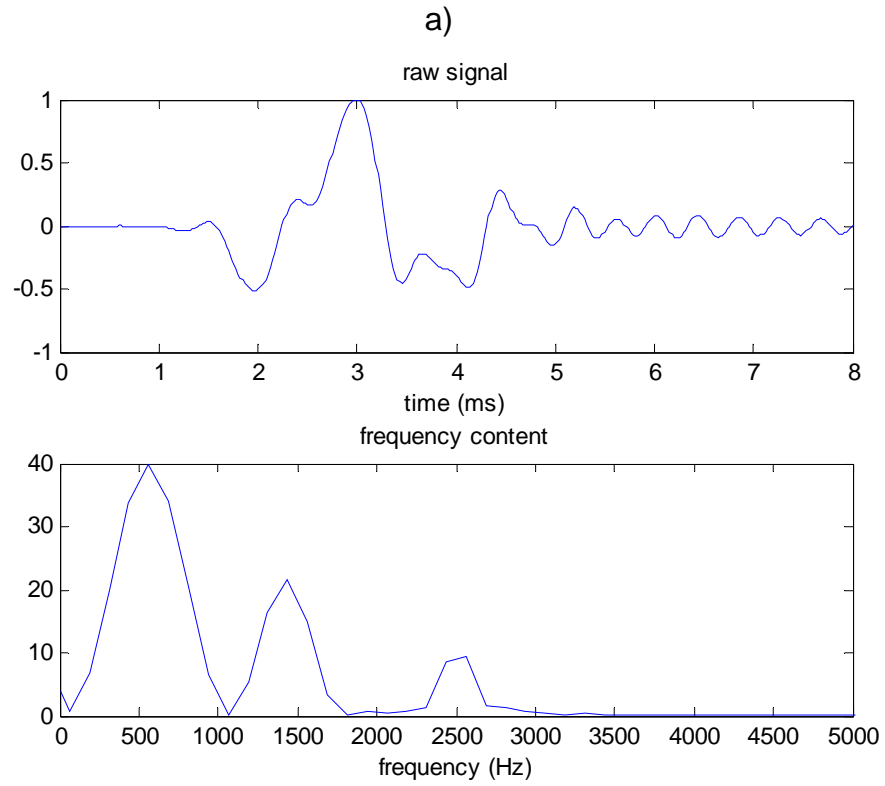


Figure 3-3. A simplified flowchart for the proposed inversion scheme



(Figure 3-4 is continued in the next page)

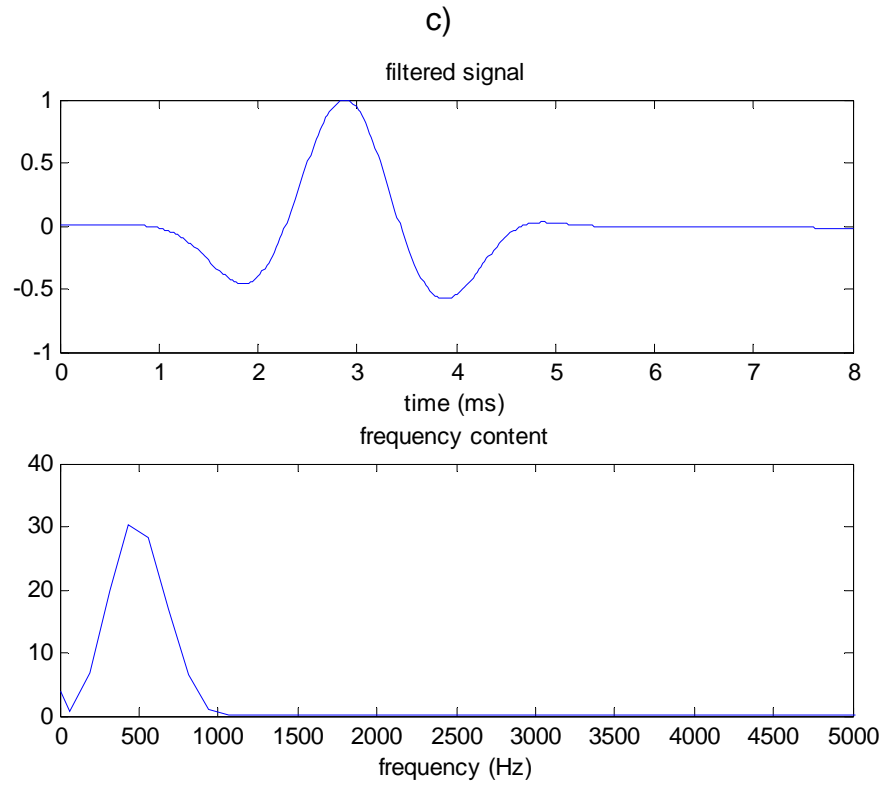


Figure 3-4. Concept of frequency filtering: a) Raw data and the frequency spectrum, b) First-level filtering, and c) Second-level filtering

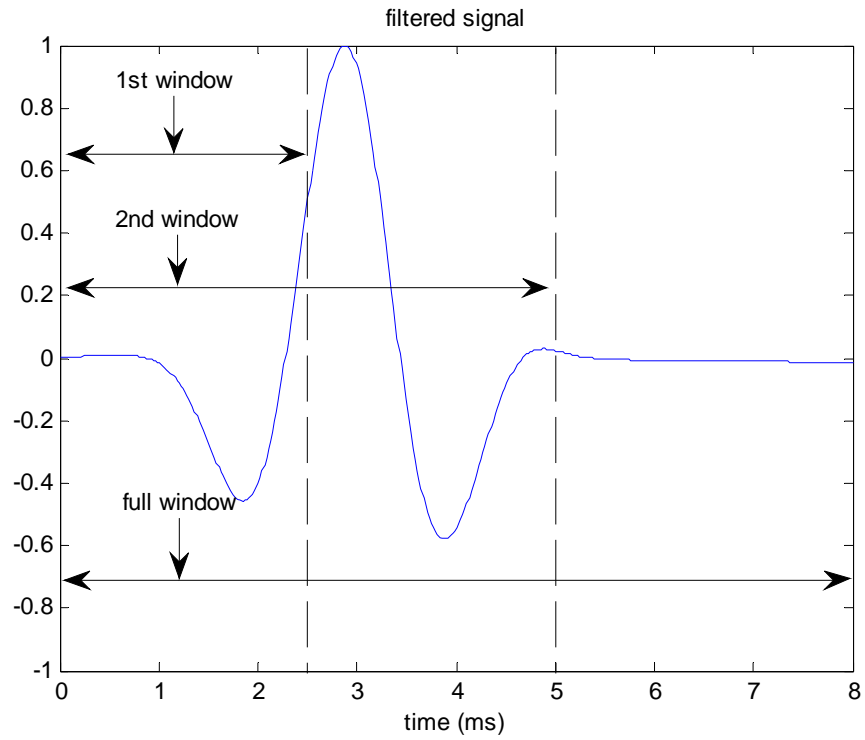


Figure 3-5. Concept of time windowing: gradually increasing the length of the window to facilitate convergence

CHAPTER 4 VALIDATION OF FORWARD MODEL AND FULL WAVEFORM INVERSION

4.1 Introduction

Using the previously developed forward model and inversion scheme, this chapter describes how the coupled system works. First, the forward model is validated by comparing the synthetic waveforms with known analytical solutions. Second, the inversion scheme is tested using synthetic records generated from axisymmetric forward models. Lastly, the inversion scheme is further tested using synthetic records generated from 3-D borehole models.

4.2 Validation of the Forward Model

The solution provided by the forward model must be accurate; otherwise, the subsequent inversion may be inaccurate or even misleading, as FWI aims at minimizing errors between the observed waveforms and the synthetic waveforms generated by the forward model.

Biot (1952) predicted that the velocity of Rayleigh waves propagating inside a borehole depends on the ratio between the wavelength and the size of the borehole. To test this theoretical prediction, the present study investigated homogeneous axisymmetric borehole models with radii of 0.05, 0.25, 1, and 10 m, shear wave velocity of 1000 m/s, Poisson's ratio of 0.25, and mass density of 2000 kg/m³. The particle displacements were recorded at the same location on each borehole and then compared. A triangular wavelet source generated the waveforms (Figure 4-3a), ensuring that the wavelength was fixed for all cases. Axial and radial particle displacements were measured and graphed individually for each borehole radius, and the amplitude of individual waveforms was normalized for ease of comparison (Figure 4-

1). The resulting graphs clearly illustrate that Rayleigh waves travel faster within boreholes with smaller radii, given the wavelength being the same, which confirms the theoretical prediction depicted in Figure 3-1.

On the other hand, it is hypothesized that the plane-strain model can be approximated as the radius of the axisymmetric borehole model approaches infinity. To test this hypothesis, this study compared the waveforms generated from the axisymmetric borehole model with a 1 km radius to the plane-strain solution. Results confirm that the normal and tangential components of the corresponding waveforms matched perfectly (Figure 4-2).

This set of waveform comparisons demonstrated, though indirectly, that the axisymmetric forward model formulated using ABAQUS was correct and accurate for use in the subsequent waveform inversions.

4.3 Inversion of Synthetic Data Generated by the Forward Model

In order to obtain credible velocity profiles, an analysis protocol that systematically and consistently analyzes wavefield data must be developed. This protocol can be established using synthetic model studies with known solutions; therefore, the current project performed such a study to test the effectiveness of the inversion scheme proposed in Figure 3-3. In this study, the synthetic records were generated using the axisymmetric forward model discussed above, and treated as field data. The velocity profile was then reconstructed by means of inversion. Theoretically, the inverted velocity profile should be the same as the assumed known model.

In the current implementation, only the shear wave velocity was inverted, while the Poisson's ratio (0.25) and mass density (2000 kg/m^3) remained constant during the inversion. As shown in Figure 3-2, the inversion model was uniformly discretized into 36

pixels (9 by 4), and shear wave velocity values were assigned independently to each pixel, resulting in 36 model parameters to be inverted. The synthetic waveforms were generated using a triangular wavelet source (Figure 4-3b). Note that, due to the axisymmetric nature of the model, the source was not a point load, as it may appear in Figure 2-10, but rather a uniformly distributed ring load that excites perpendicularly to the borehole wall. A low-frequency source is desirable because lower frequencies generally allow farther energy penetration, and thus deeper characterization. For this study, the goal was to obtain a velocity profile that radially extended 5 ft into the borehole wall. Using the ring load source, the ratio of the dominating wavelength to the borehole radius far exceeded the 3.2 cut-off value shown in Figure 3-1. This ratio resulted in mode conversion, as the surface wave energy converted to shear wave energy that propagated at a velocity equal to V_s . The resulting radial and axial particle displacements are graphed in Figure 4-4.

Note that the radial component was highly oscillatory, while the axial component was relatively well behaved. As discussed above, the nonlinearity of the inverse problem depends on the level of oscillation in the seismic data. The use of radial components inside a borehole is a natural extension of the fact that the vertical components of seismic data are routinely used in surface waveform inversions. However, the radial component in this study was highly oscillatory, which prevented the inversion from converging, despite the use of the proposed multiscale strategy. Conversely, convergence did occur when the initial model was very close to the true model. In fact, if convergence is to be achieved, the quality of the initial model must increase as the nonlinearity of the inverse problem increases. This is the very reason

why the multiscale approach was developed, to lessen the need for a good initial model by reducing the nonlinearity of the error space. It is therefore concluded that the radial component, as generated in the above study, is not viable for use in borehole waveform inversion, as the level of detail needed in the *a priori* information is nearly impossible to meet. On the other hand, the axial component, or the in-plane component, of the borehole data is much easier to manage.

Figure 4-5 presents the schematic used for conducting the synthetic experiment. A triangular wavelet source (Figure 4-3b) was excited at the center (the red arrow in Figure 4-5) of the inner wall of an axisymmetric borehole model. A 10-channel receiver array was uniformly placed along the wall, with the nearest offset and trace interval being 0.5 m (the hollow circles in Figure 4-5). Using this configuration, the axial component of the particle displacements was monitored (the double-headed arrows near the receiver array in Figure 4-5). For the synthetic model studies discussed in the following sections, inversions were carried out by matching the axial component of the particle displacements. The amplitude of the waveforms and the L2 norm of the misfit function were normalized for ease of comparison.

4.3.1 Horizontally Layered Model

The horizontally layered model (Figure 4-6a) comprised nine distinct velocity layers, each 0.5 m thick. The shear wave velocity varied gradually from 450 m/s at the top, to 1000 m/s in the middle, and back to 450 m/s at the bottom. This model was chosen because a majority of geological materials are multi-layered and exhibit spatial variations.

The shear wave velocity of the initial model was 775 m/s uniformly across all pixels (Figure 4-6b). A total of 4 ms of full waveforms was acquired. The inversion

started with a short time window of 2 ms, and a low-pass filter was applied to the associated waveforms. The first column of pixels in the updated model after 10 iterations had good resolution, while the second and third columns were vague, and the last column exhibited no change in values (Figure 4-7a). The associated waveforms matched very well, and the inversion converged rapidly. This model required approximately twenty minutes for 10 iterations on a standard personal computer, and the computer time will scale up with the number of iterations. Next, using the last updated model as the initial model, the waveforms were inverted under the same time window with no filter applied. After an additional 10 iterations, the resolution of the middle columns of pixels improved considerably, while no major change occurred in the last column (Figure 4-7b). The waveforms were well matched, and the inversion converged very rapidly.

To increase resolution, FWI was applied, and the time window was set as the entire length of the acquired waveforms. Using the last updated model as the initial model, a low-pass filter was applied to the inversion after 25 iterations, which significantly improved the resolution in the last three columns (Figure 4-7c). At this point, the layered structure became identifiable, especially for the middle rows of pixels. Again, the waveforms were well matched, and the convergence rate was fast. The solution illustrated in Figure 4-7c is considered to be a very good initial model for further velocity updates.

To further increase resolution, high-frequency components of the data should be incorporated into the inversion. Therefore, the last step in this process was to set the inversion to continue for 100 iterations based on the raw data set, unless converged

according to the predefined stopping criteria. The layered structure of the final inverted model was very well recovered, as the first three pixel columns closely approximated the true model (Figure 4-7d). Some smearing is visible in the last column, despite the fact that the waveforms were in excellent agreement across all channels. This smearing occurred because those model parameters were less constrained by the acquired data, and thus could not be inverted with certainty. Two possible solutions to this problem are: 1) to further increase the length of the acquired data in order to look deeper behind the borehole wall, or 2) to collect multiple shot gathers by placing the source at multiple locations along the receiver array in order to improve spatial coverage. The latter approach is more effective, particularly when resolving isolated anomalies in the vicinity of a borehole, as detailed in Chapter 5.

The convergence rate in the last step of the inversion was much slower than in the previous steps (Figure 4-7d). Previously, the L2 norm had decreased by a factor of 10 in less than 10 iterations, while this decrease occurred over approximately 50 iterations in the final step. In fact, the L2 norm only decreased by a factor of 2 in the first 10 iterations, and it continued decreasing at an extremely slow rate for the last 50 iterations. In the Gauss-Newton method, convergence tends to be quadratic once the search approaches the local minimum. However, since misfit function at high frequencies tend to have an extremely nonlinear error space, a reduced convergence rate can be expected. It is also possible that limited sensitivity of the acquired data, discussed above, caused the slow convergence rate.

4.3.2 Cylindrically Layered Model

The cylindrically layered model (Figure 4-8a) consisted of four constant velocity layers, each 0.5 m thick. The shear wave velocity varied from 1000 m/s, to 775 m/s, to

450 m/s, and back to 1000 m/s. This model is capable of producing significant reflections and mode conversions, and was therefore selected to test the effectiveness of the proposed inversion scheme in handling complicated wavefield data.

A uniform shear wave velocity of 775 m/s was selected as the initial model (Figure 4-8b). The multiscale strategy was applied throughout the inversion. First, the inversion ran for 20 iterations with a 2 ms time window and a low-pass filter (Figure 4-9a). The resulting first column showed good pixel recovery, and the resolution in the second column changed slightly as a result of the assigned true velocity values. The third column exhibited a low velocity zone, while no significant changes appeared in the last column. The waveforms were in good agreement, and the inversion converged fairly rapidly.

Next, the inversion continued for another 20 iterations with the same time window and without filtering (Figure 4-9b). The first two layers were near perfect reconstructions of the true model, a low velocity layer became visible in the third column, and the last column remained unchanged. Again, the waveforms were well matched, and the convergence rate was fast. The next 20 iterations used a full time window of 4 ms and a low-pass filter (Figure 4-9c). The most noticeable change appeared in the last column of pixels, which began to gain high velocity values. A more clearly developed low velocity layer was also observed in the third column. The waveforms were once again in good agreement; however, the convergence curve was not as smooth as previous curves.

To increase the resolution of the recovered image, the raw data set was inverted in the last step for 100 iterations (Figure 4-9d). This set of iterations perfectly recovered the first three layers of the true model, whereas some uncertainties appeared in the last

layer. As expected, the good model recovery caused the waveforms to be in near perfect agreement across all channels; however, the shapes of the waveforms were very complicated and difficult to match. Had the inversion started with the raw data set, it would have never converged given the chosen initial model. In other words, the final inverted model shown in Figure 4-9d cannot be obtained using the initial model presented in Figure 4-8b. Interestingly, the convergence curve shown in Figure 4-9d exhibited a discontinuity at approximately 75th iteration, after which the convergence rate increased significantly, then gradually decreased.

These two synthetic model studies illustrate that the proposed inversion scheme is indeed capable of reconstructing the assumed true model. Applying the multiscale strategy in the time and frequency domains can mitigate the nonlinearity of the inverse problem and lessen the need for a good initial model for essentially any gradient-based inversion technique. In addition, the tradeoff between penetration depth and resolution must be realized, meaning long wavelengths (low frequencies) penetrate further, while short wavelengths (high frequencies) provide higher spatial resolutions.

It must be noted that imperfect model recovery is always possible, even when using data generated by the forward model, as the data may poorly constrain some of the model parameters, resulting in non-unique solutions in practice. Therefore, synthetic model studies are valuable for guiding experiment design. The viability of a solution and the attainability of the resolution depend on two critical aspects: 1) the distribution of measurements for good spatial coverage, and 2) the selection of instruments for gathering high-quality data (Santamarina and Fratta, 2005). Three options exist for improving model recovery: 1) increase the length of the acquired full waveforms, 2)

increase spatial coverage by collecting multiple shot gathers at multiple locations along the borehole, or 3) use a combination of the first two options. Again, in Chapter 5 it is demonstrated that multiple shots are effective, particularly when resolving isolated anomalies in the vicinity of a borehole.

4.4 Inversion of Synthetic Data Generated from the 3-D Borehole Model

To evaluate the compatibility of the proposed inversion scheme with respect to the input data, synthetic records in this section were generated from 3-D borehole models using ABAQUS. Ideally, given the same Earth model, the axisymmetric forward model and the 3-D model should predict the same wavefield. However, since different types of elements and various meshing techniques were used to formulate the finite element models, the synthetic waveforms are not identical, but are fairly similar. Because “noisy” data were used to infer model parameters, true models could not be perfectly recovered.

Figure 4-10 presents the schematic used for conducting this synthetic experiment inside a 3-D borehole. To approximate a pulse loading, a triangular wavelet source (Figure 4-3b) was radially excited in the center of the borehole wall (indicated by the red square in Figure 4-10). The axial component of particle displacements (the double-headed arrows in Figure 4-10) was monitored using a 10-channel receiver array uniformly placed along the wall, with the nearest offset and trace interval being 0.5 m (the hollow circles in Figure 4-10). For the synthetic model studies discussed in the following sections, inversions were carried out by matching the predicted waveforms (from the axisymmetric forward model) against the observed waveforms (from the 3-D borehole models). The amplitude of the waveforms and the L2 norm of the misfit function were normalized for ease of comparison.

4.4.1 Homogeneous Model

A uniform shear wave velocity of 1000 m/s was selected for the true model of this simple homogeneous borehole model (Figure 4-11a). The inversion started with an initial shear wave velocity of 775 m/s and followed a similar multiscale approach (Figure 4-11b). The true model was well recovered in that the inverted values of shear wave velocity ranged from 950 m/s to 1070 m/s. The bowl-shaped resolvability is due to the limited spatial coverage, as only one shot gather was acquired in the data collection. The observed and predicted waveforms were in very good agreement, and a typical convergence curve was observed (Figure 4-11c).

This synthetic model study illustrates that the proposed inversion scheme is capable of handling 3-D data set, because when studying a homogeneous medium the 3-D model and the axisymmetric forward model are compatible with each other.

4.4.2 Homogeneous Models with Ring Anomalies

Despite the fact that ring-shaped anomalies are rare in practice, this study investigated them to test the resolving capability of the proposed inversion scheme in terms of “depth” of characterization. The observed waveforms were generated with a low-velocity, ring-shaped anomaly ($V_s = 450$ m/s) buried inside a 3-D homogeneous medium ($V_s = 1000$ m/s). The ring-shaped anomalies were designed so that the radial distances into the borehole wall increased continually.

The near anomaly (Figure 4-12a) had a 0.5 m by 0.5 m square section placed 0.5 m away from the wall. The inversion started with an initial shear wave velocity of 1000 m/s. Only one low-pass filter was applied to the full waveforms, and the inversion was set to run for 15 iterations. Figure 4-12b illustrates that the anomaly was successfully detected in the inverted model. The inverted shear wave velocity value was

approximately 480 m/s for the anomaly, and ranged from 950 m/s to 1050 m/s for the homogeneous background. The waveforms were well matched, and the convergence rate was fast (Figure 4-12c). These results can be attributed to the good initial model used for the inversion, and to the success of the Gauss-Newton method.

The deep anomaly had a 0.5 m by 0.5 m square section placed 1.0 m away from the wall (Figure 4-13a). Using the same initial model and inversion procedure, the inversion was set to stop after 50 iterations. The anomaly and the homogeneous background were well recovered (Figure 4-13b), with the inverted shear wave velocity value at approximately 520 m/s for the anomaly, and ranging from 950 m/s to 1050 m/s for the homogeneous background. The waveforms were well matched, and the convergence rate was rapid for the first 10 iterations, but slowed considerably over the remaining iterations (Figure 4-13c).

The deeper anomaly had a 0.5 m by 0.5 m square section placed 1.5 m away from the wall (Figure 4-14a). Following the same initial model and inversion procedure, the inversion was set to stop after 50 iterations. The anomaly and the homogeneous background were well recovered (Figure 4-14b). The inverted shear wave velocity value was approximately 550 m/s for the anomaly, and ranged from 950 m/s to 1100 m/s for the homogeneous background. The waveforms were well matched, and the convergence rate was acceptable (Figure 4-14c).

The above synthetic model studies based the inversion on an axisymmetric forward model, whereas the input data were taken from 3-D borehole models, and suggest that with a good initial model the inversion technique can consistently detect ring-shaped anomalies.

4.4.3 Horizontally Layered Models with a Ring Anomaly

To add further complexity, this study investigated a ring-shaped anomaly inside a horizontally layered media (Figure 4-15a). The anomaly had a 0.5 m by 0.5 m square section placed 0.5 m away from the borehole wall. The shear wave velocity of the anomaly was 450 m/s, and the shear wave velocity of the layered structure was the same as in Figure 4-6a.

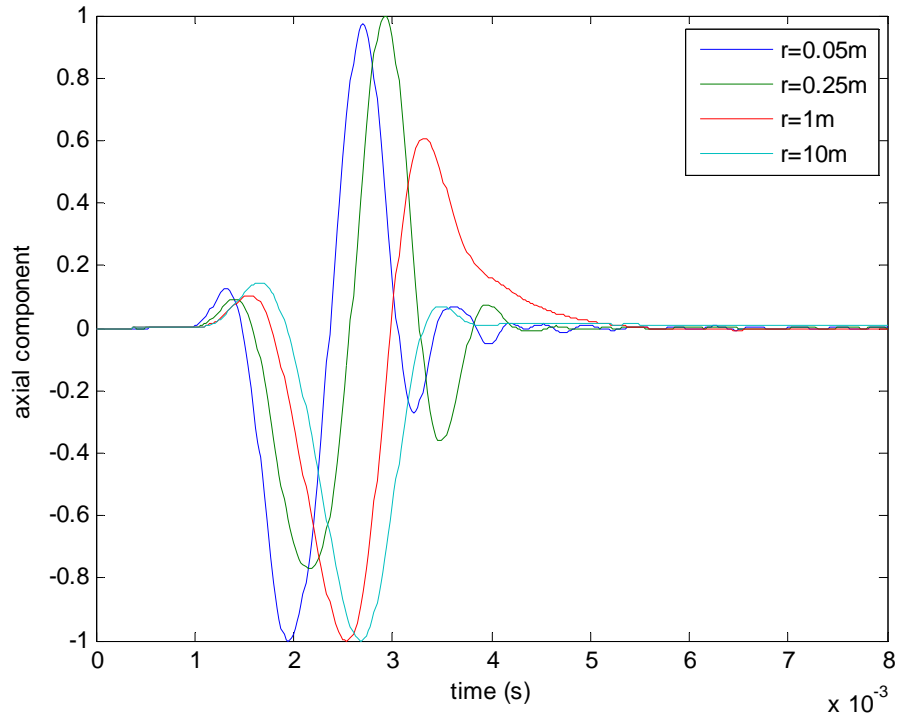
A uniform shear wave velocity of 775 m/s was selected as the initial model (Figure 4-15b). Following the proposed multiscale approach, the inversion was carried out using three consecutive time windows, and a low-pass filter was applied to the waveforms at each time window. First, the inversion was set to run for 10 iterations with the shortest time window of 2 ms, and the last updated model was used as the starting model for the next run. Next, the inversion was set to run for 15 iterations with the medium time window of 3 ms, and again the last updated model was taken as the starting model for the next run. Finally, the inversion proceeded until 30 iterations were completed, with the full time window of 4 ms. The velocity models were updated radially, as illustrated by the intermediately inverted models at each time window presented in Figures 4-15c through 4-15e. The anomaly started to become visible even with the shortest time window, while the layered structure only became distinguishable as the time window widened. The radial updates were successful due to the fact that details were successively added to the solution as high-frequency components, and full records were taken into account in the waveform inversion.

In the final inverted model (Figure 4-15e), the true model was reasonably well recovered, as both the layered structure and the anomaly were successfully delineated and detected. It is of note that the recovered shear wave velocity values gradually lost

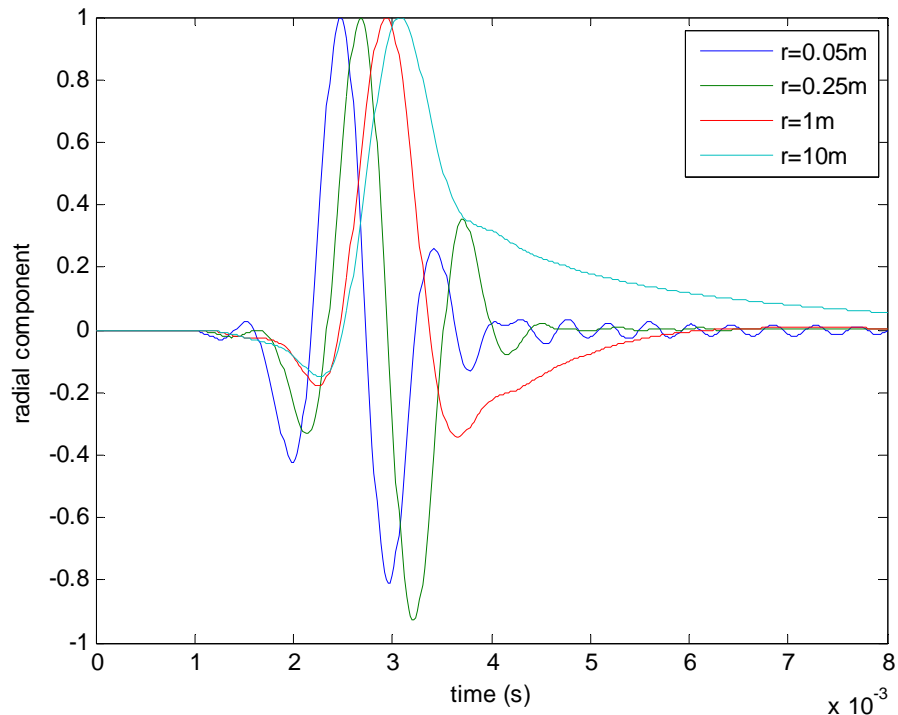
fidelity as the radial distance increased, which is the inherent tradeoff between penetration depth and resolution, discussed above. Nonetheless, the observed and predicted waveforms were in good agreement across all channels, and the misfit function rapidly converged as the number of iterations increased for all inversion attempts (Figures 4-15c through 4-15e). The velocity resolution may be improved by adding multiple shot gathers along the receiver array, as sensitive data would significantly constrain the inverted model.

4.5 Summary

This chapter validated the finite-element-based forward model developed in chapter 3, and verified that the proposed inversion scheme is effective with synthetic data sets generated from both the axisymmetric forward models and the 3-D borehole models.

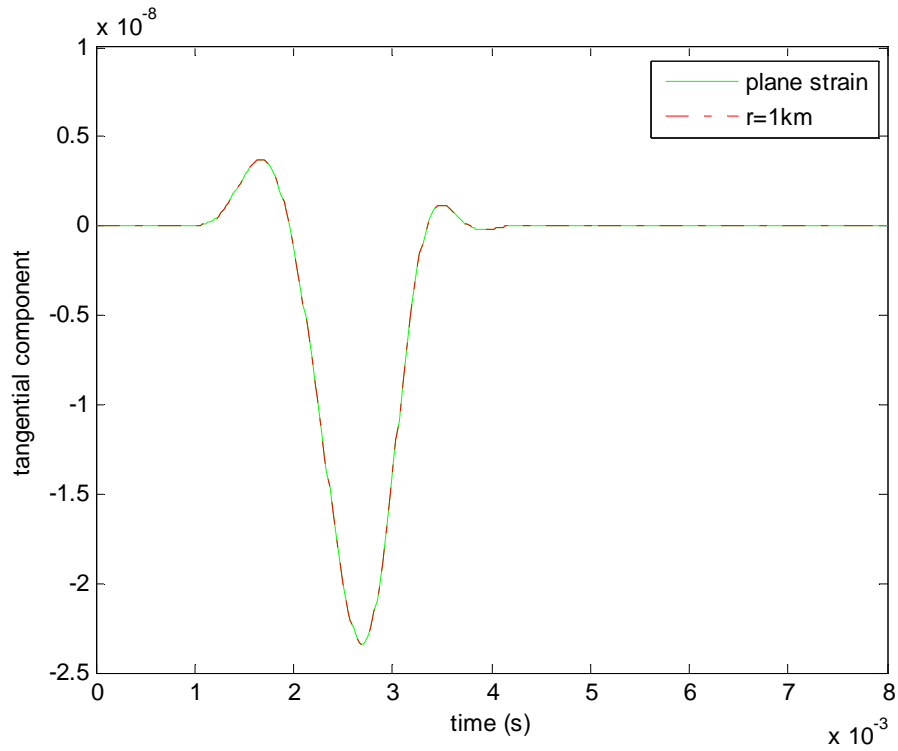


a)

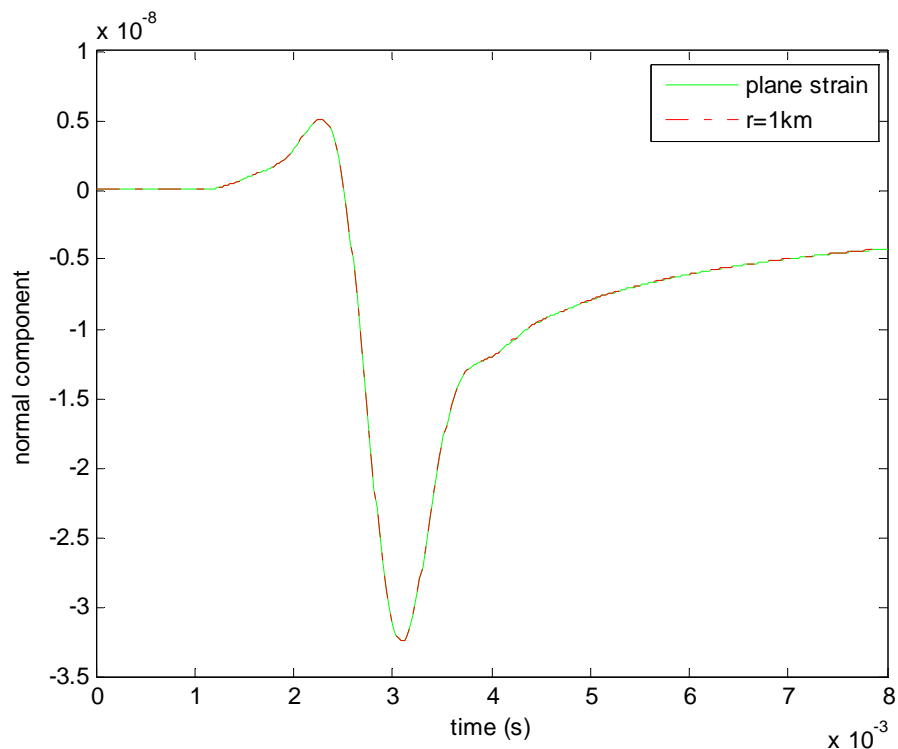


b)

Figure 4-1. Waveform comparison for boreholes with varying radii: a) Axial displacement and b) Radial displacement

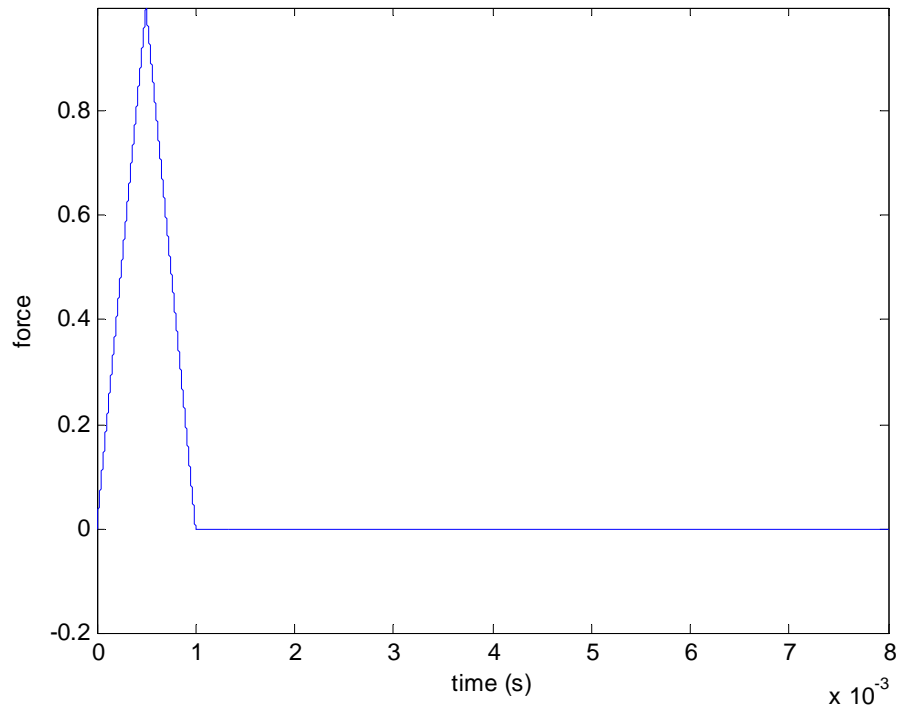


a)

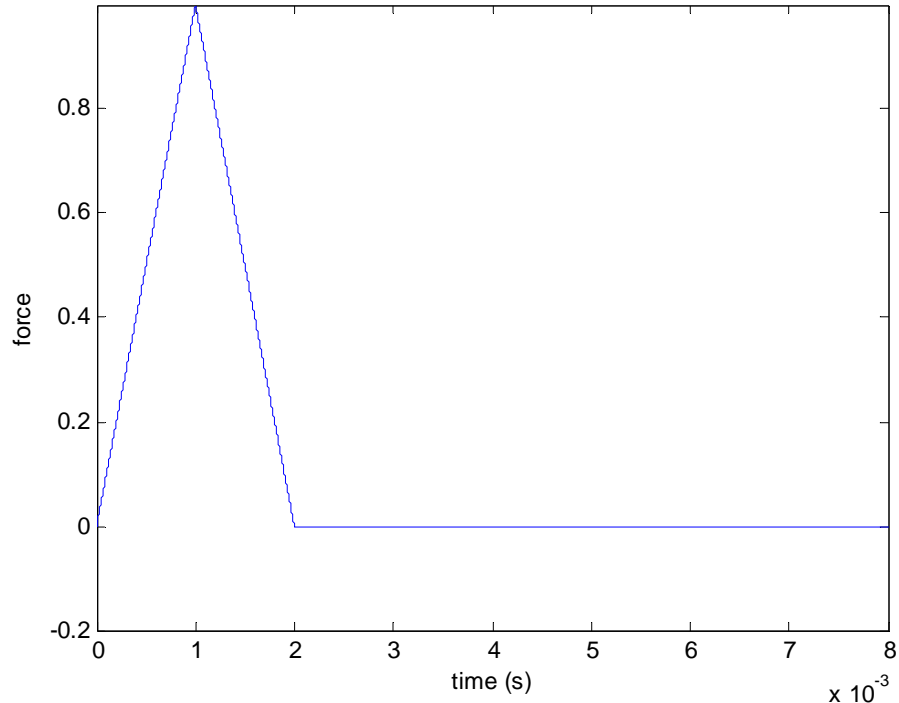


b)

Figure 4-2. Waveform comparison for a borehole with a 1 km radius and plane-strain flat ground solution: a) Tangential displacement and b) Normal displacement

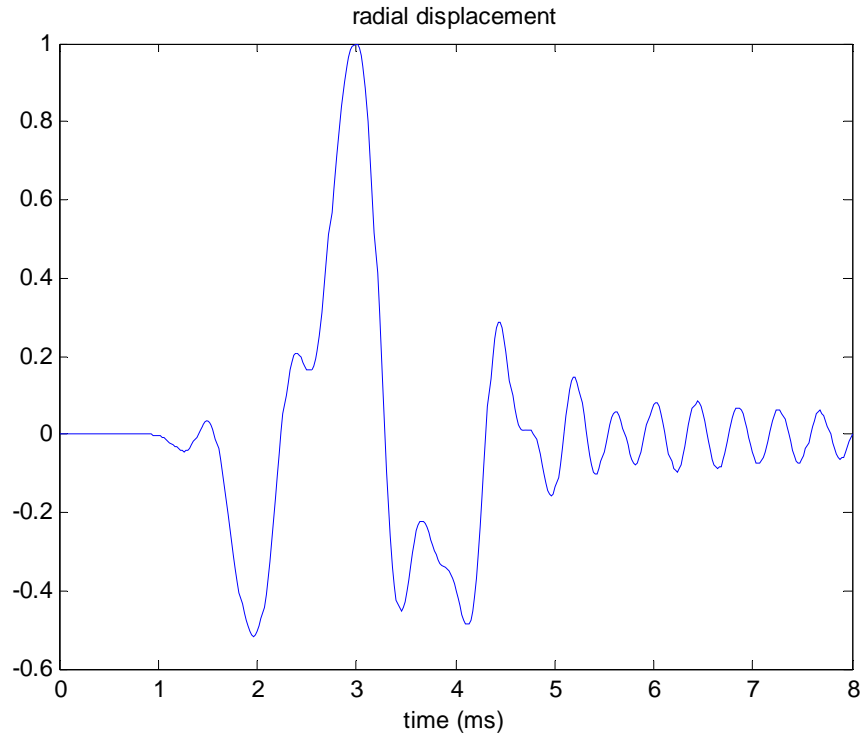


a)

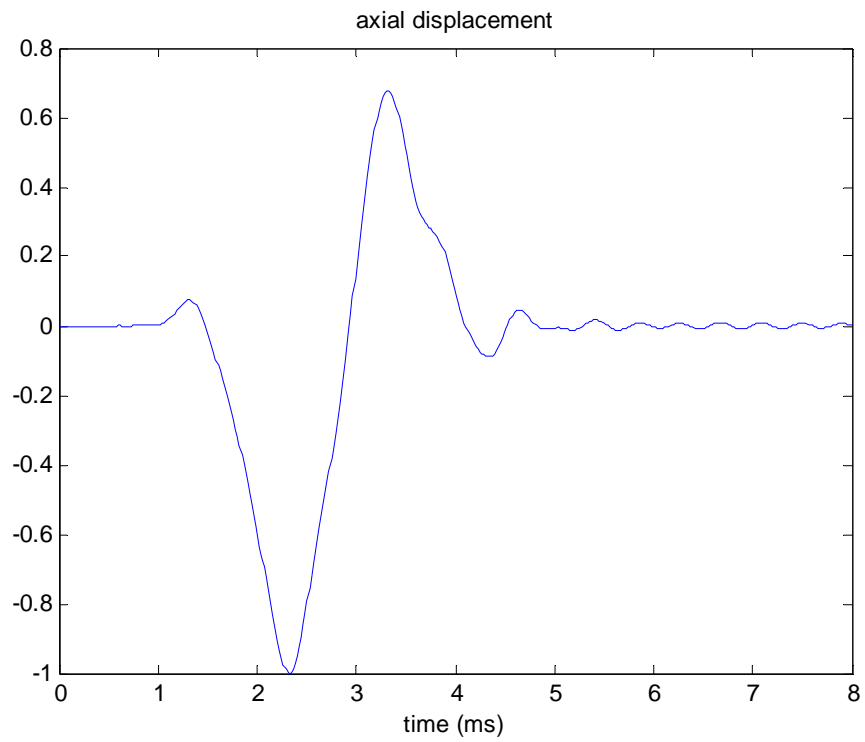


b)

Figure 4-3. Triangular wavelet sources: a) High-frequency source and b) Low-frequency source



a)



b)

Figure 4-4. Borehole synthetic data: a) Radial displacement and b) Axial displacement

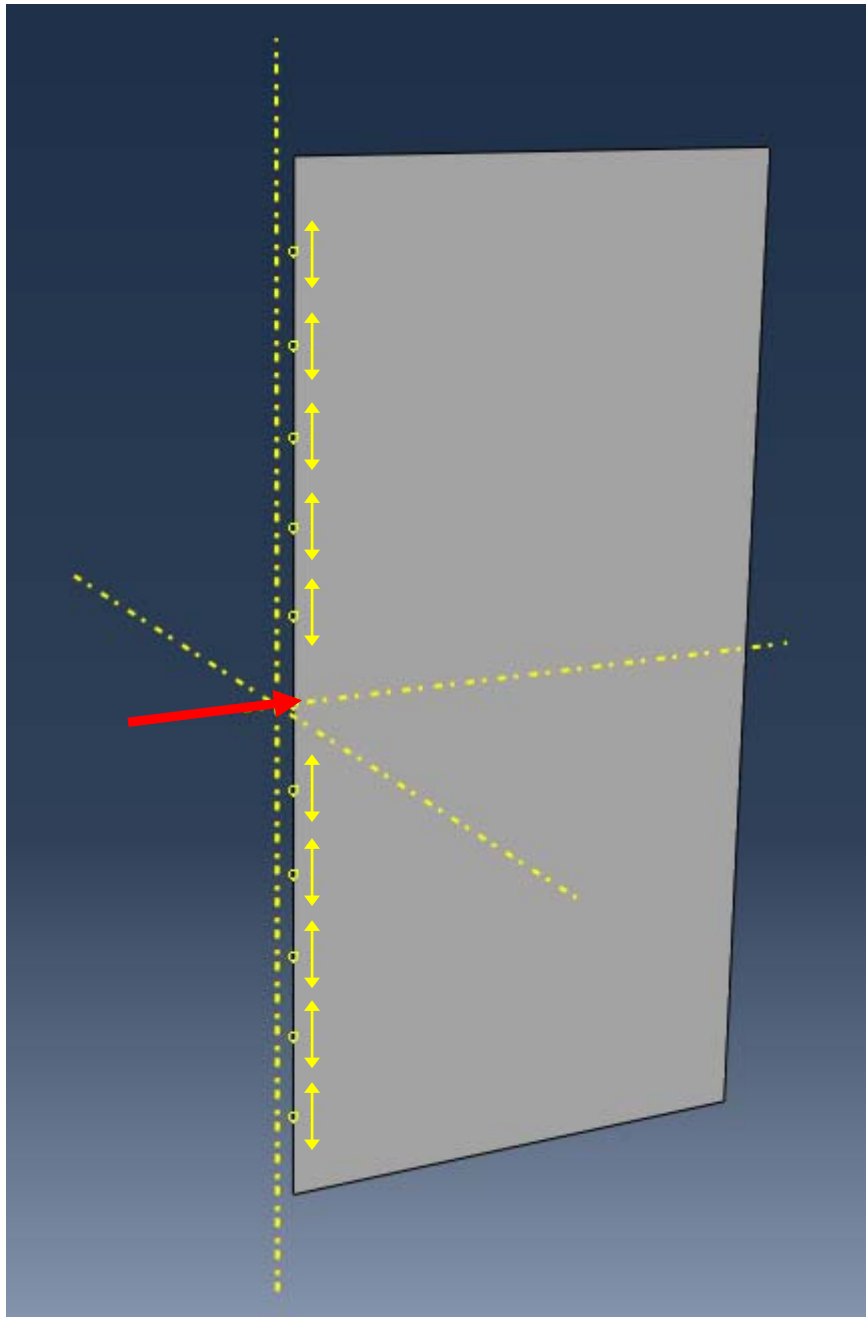


Figure 4-5. The process for conducting the synthetic experiment inside a borehole (axisymmetric model)

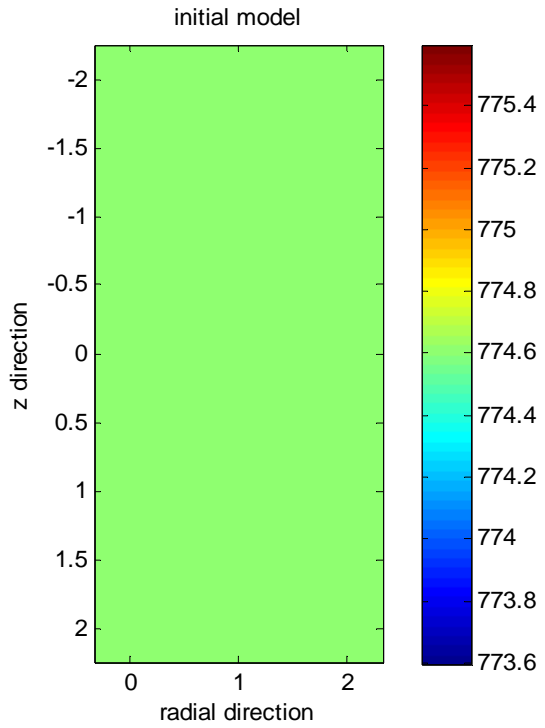
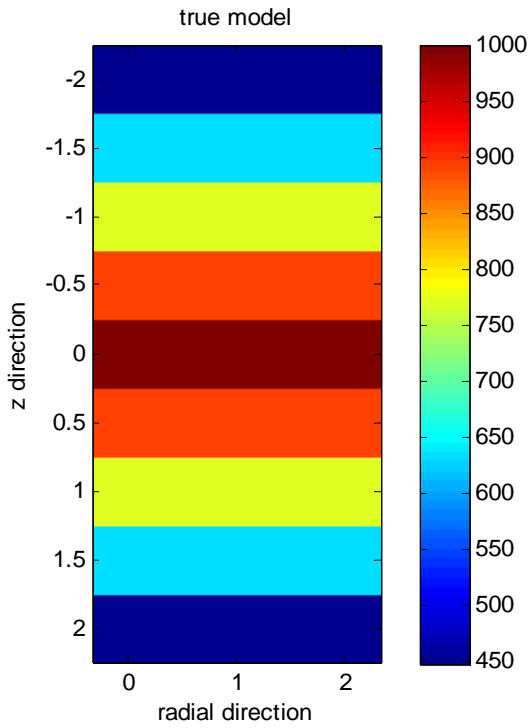
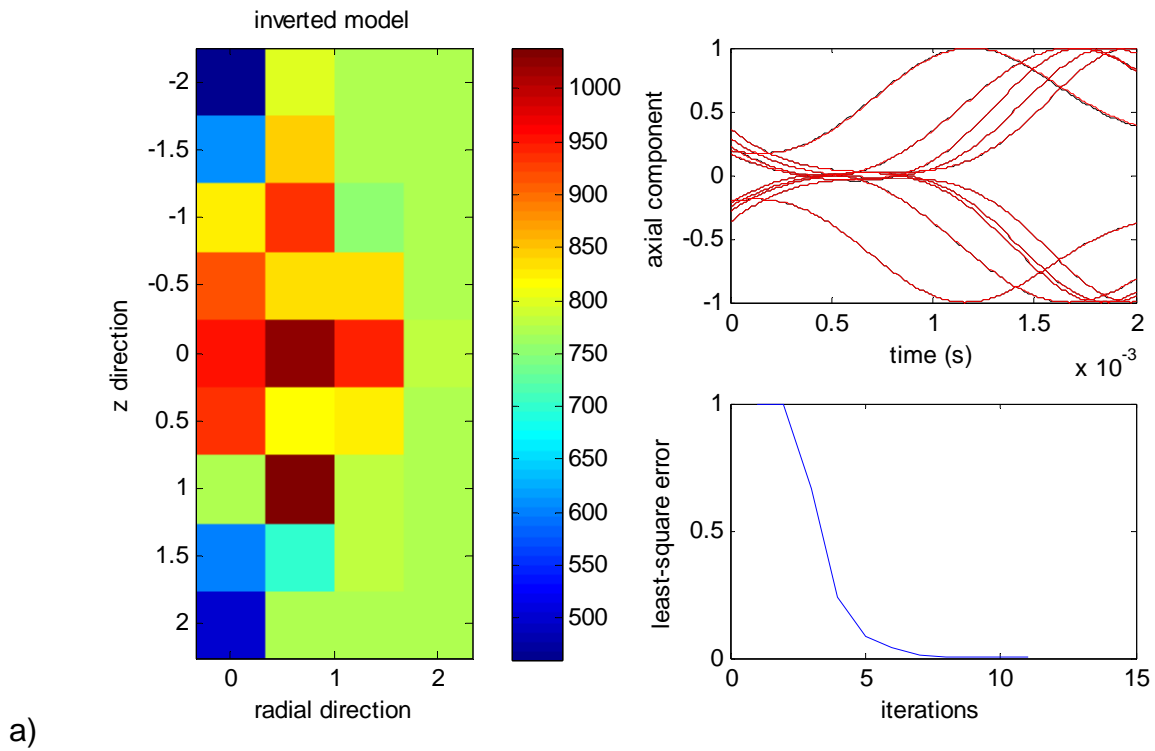
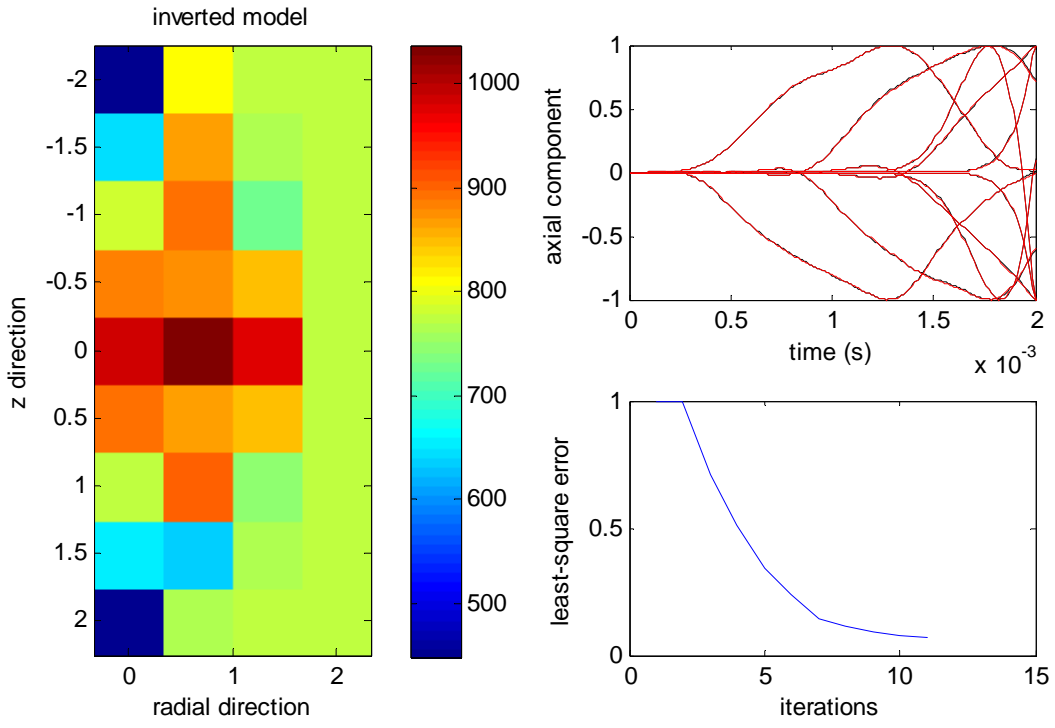


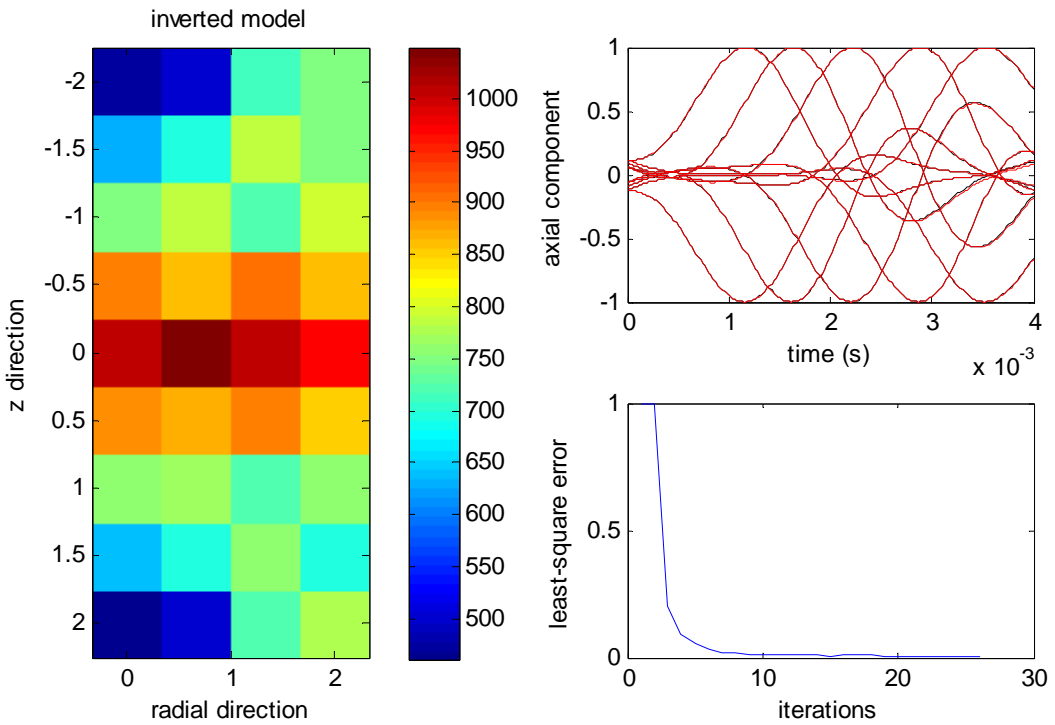
Figure 4-6. Horizontally layered model: a) True model and b) Initial model



(Figure 4-7 is continued in the next page)

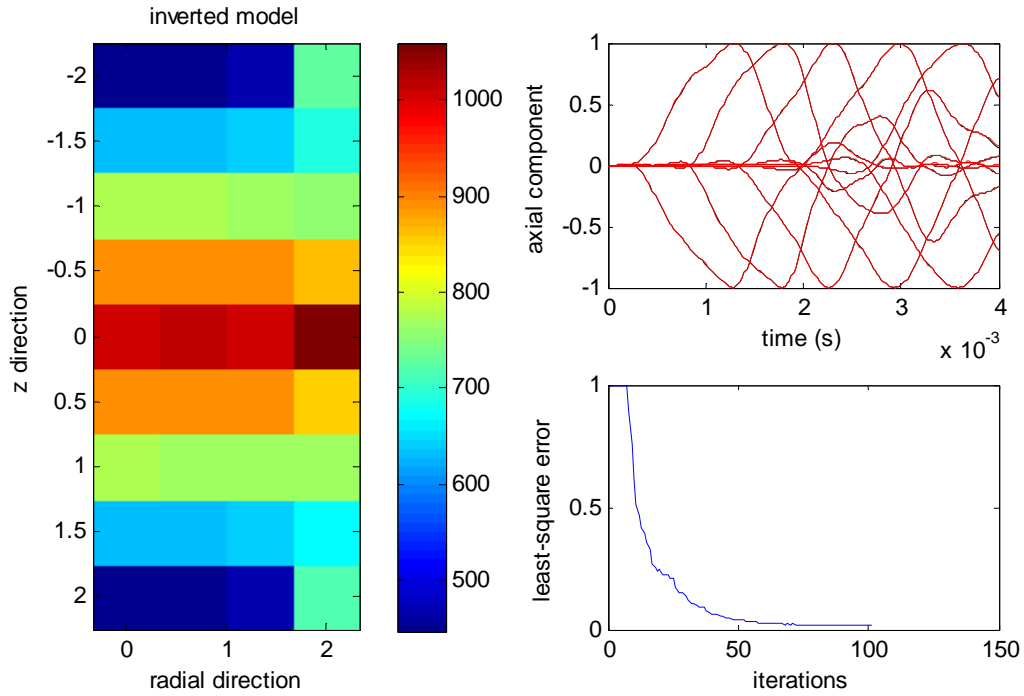


b)



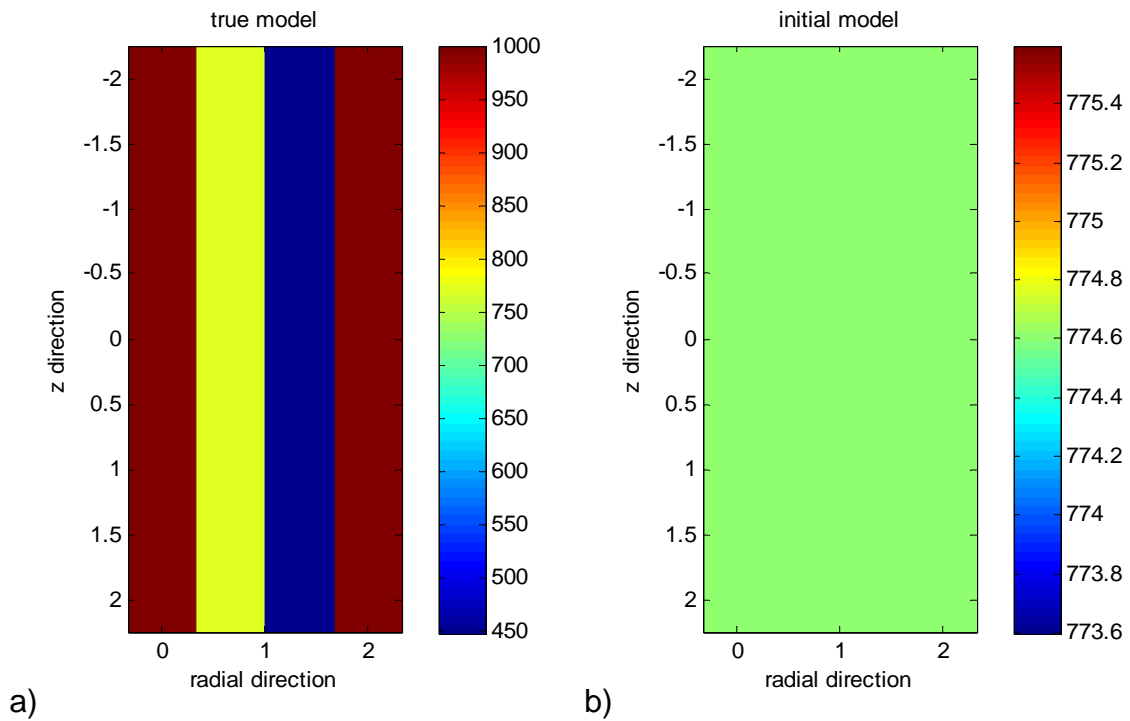
c)

(Figure 4-7 is continued in the next page)



d)

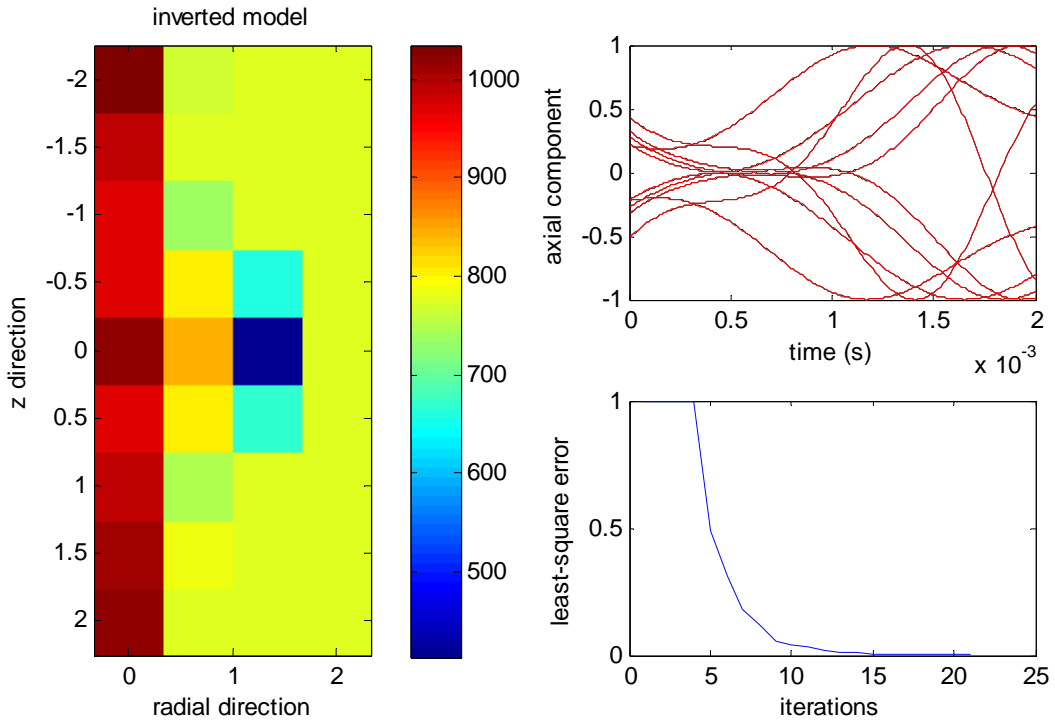
Figure 4-7. Inversion of the horizontally layered model using the multiscale approach: a) Short time window with low-pass filter, b) Short time window without filter, c) Full time window with low-pass filter, and d) Full time window without filter



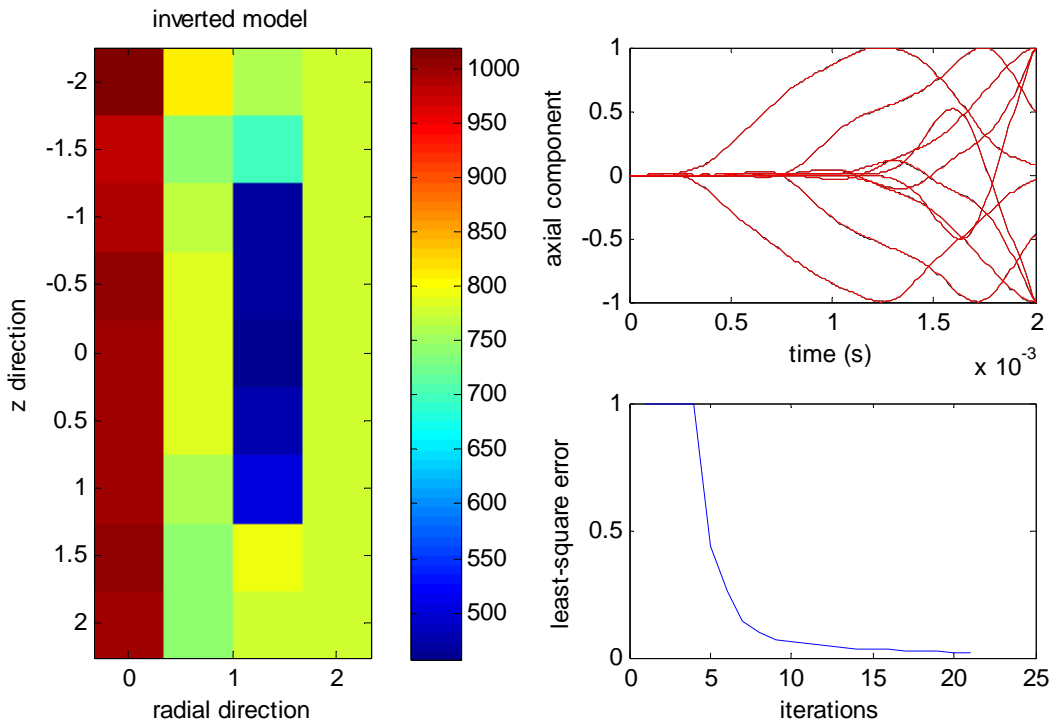
a)

b)

Figure 4-8. Cylindrically layered model: a) True model and b) Initial model

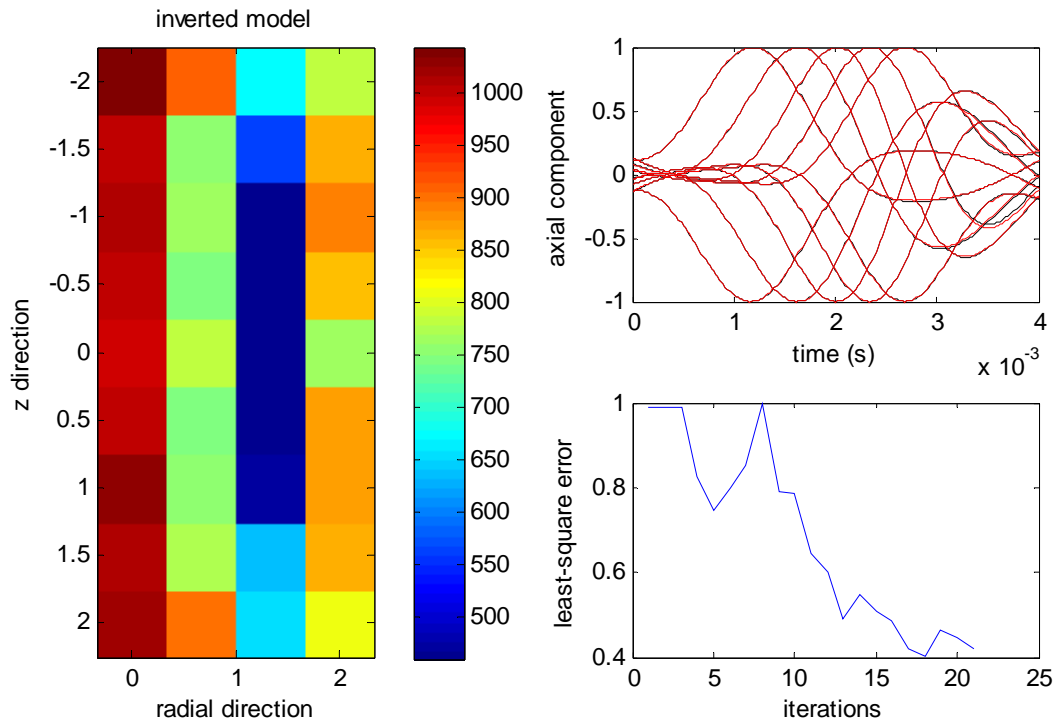


a)

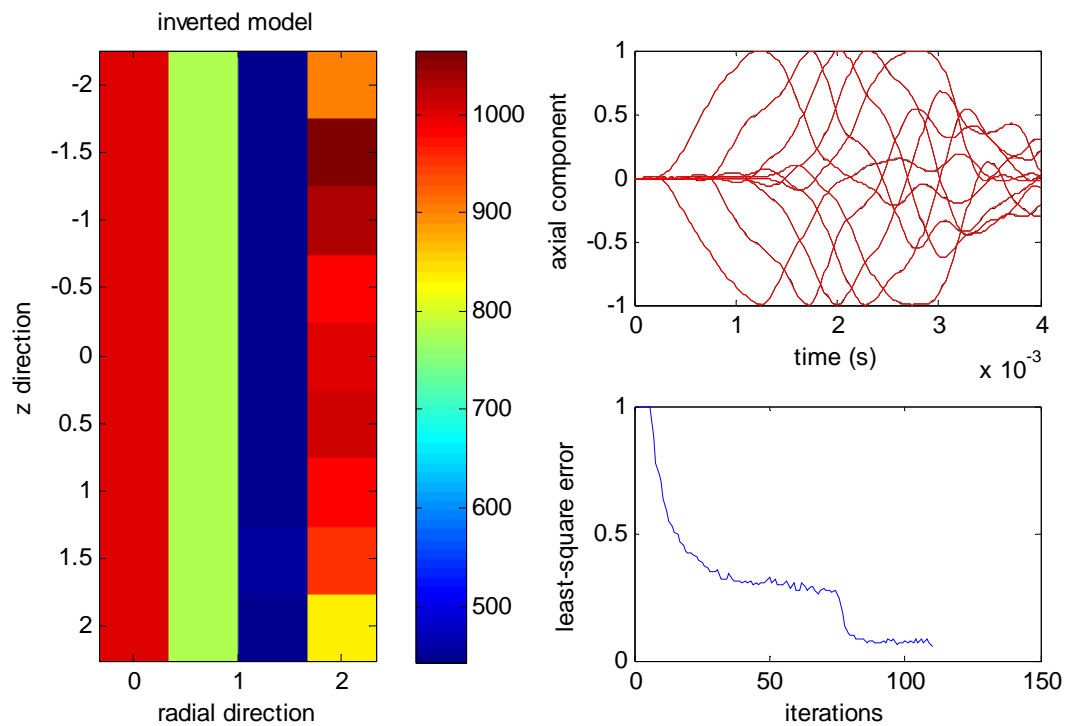


b)

(Figure 4-9 is continued in the next page)



c)



d)

Figure 4-9. Inversion of the cylindrically layered model using the multiscale approach: a) Short time window with low-pass filter, b) Short time window without filter, c) Full time window with low-pass filter, and d) Full time window without filter

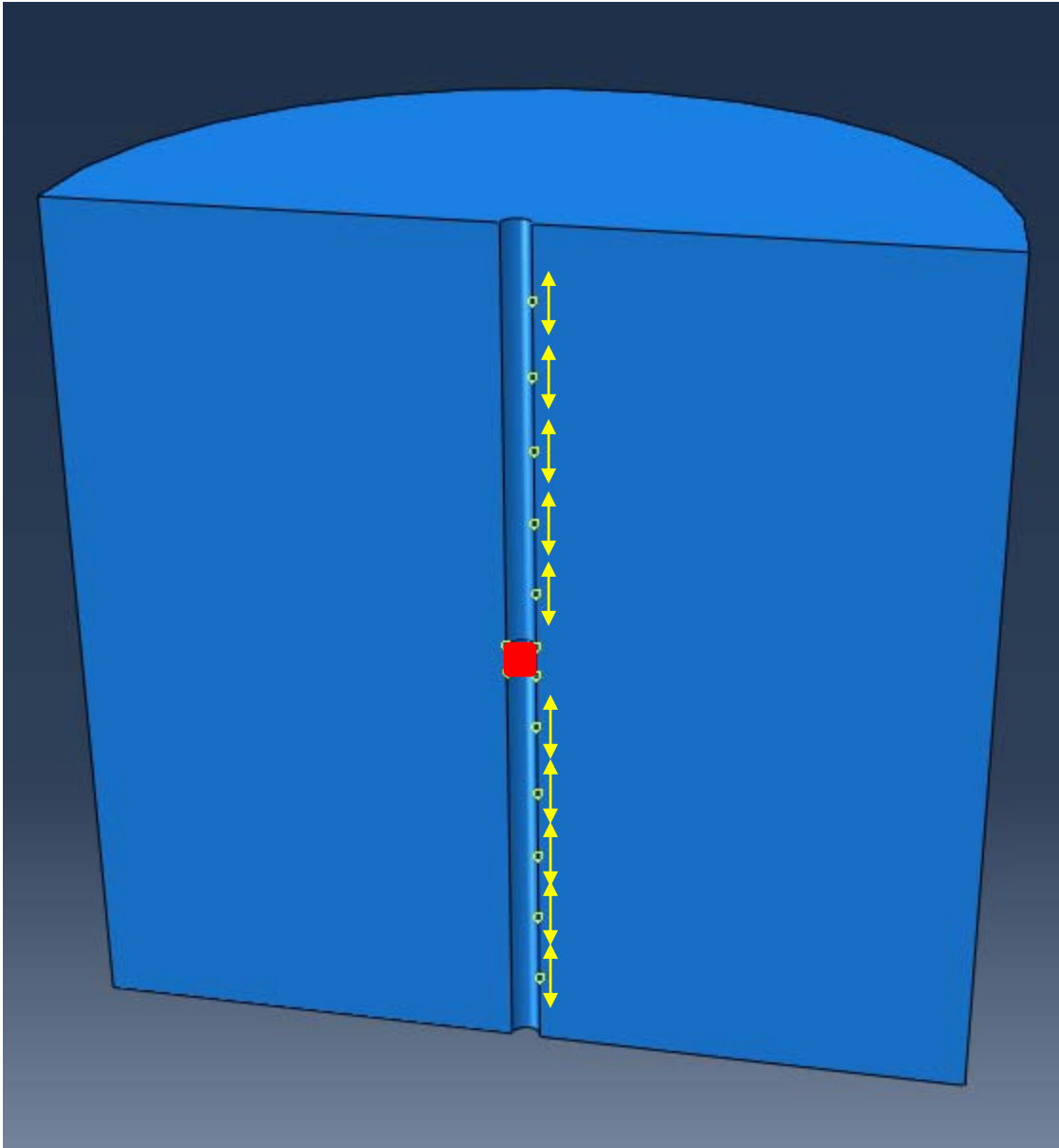


Figure 4-10. The process for conducting the synthetic experiment inside a borehole (3-D model)

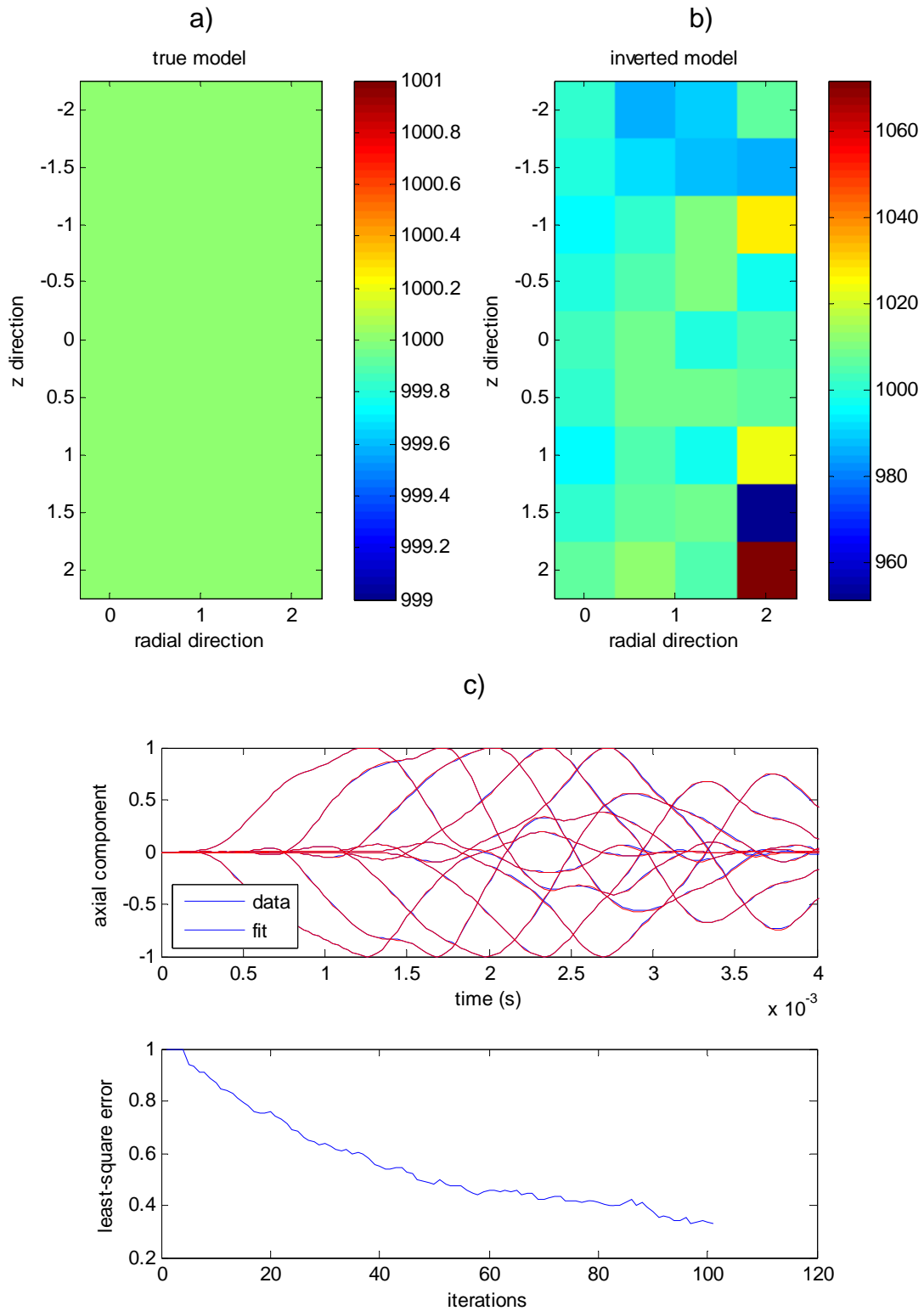


Figure 4-11. Homogeneous model: a) True model, b) Inverted model, and c) Waveform match and convergence curve

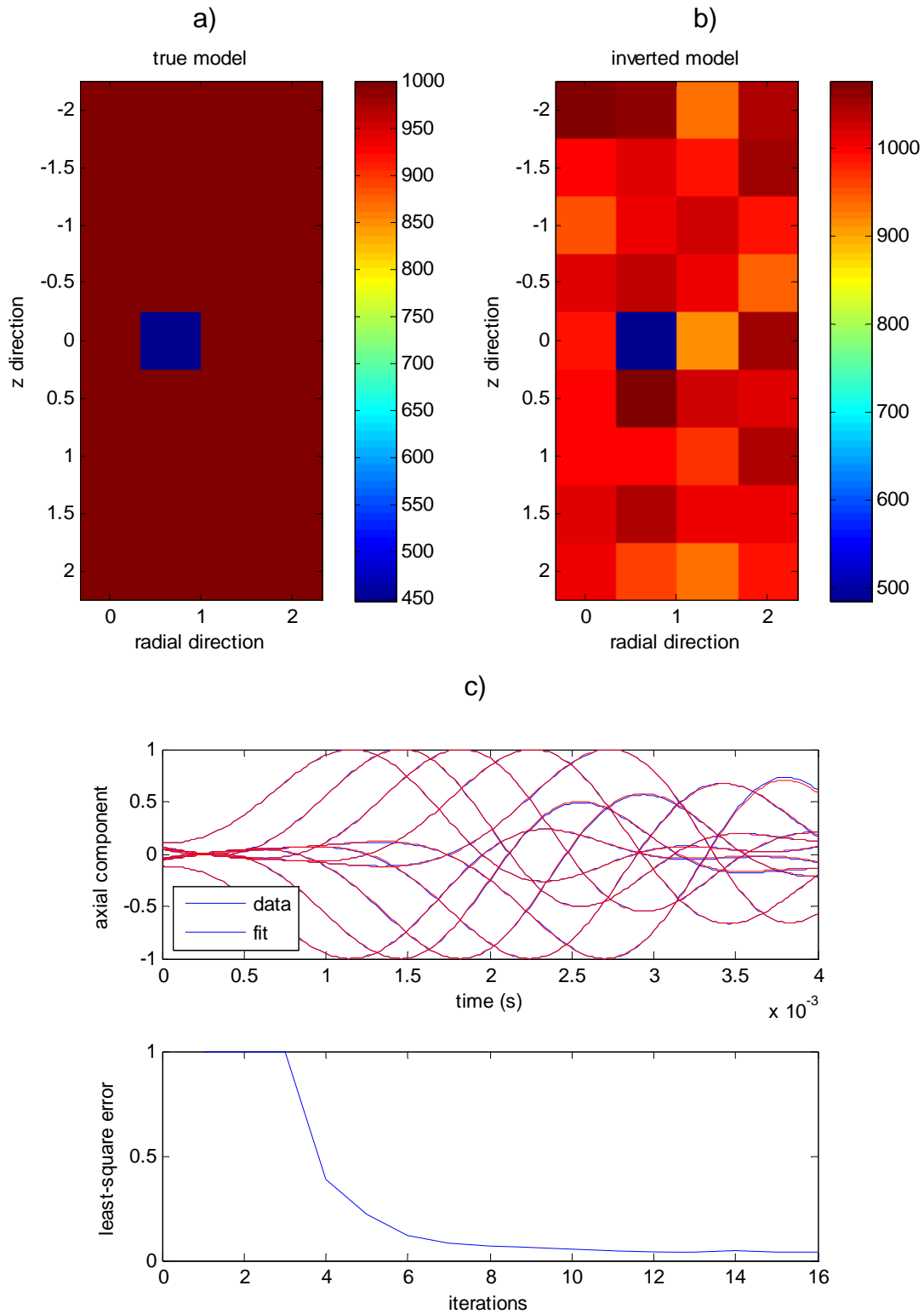
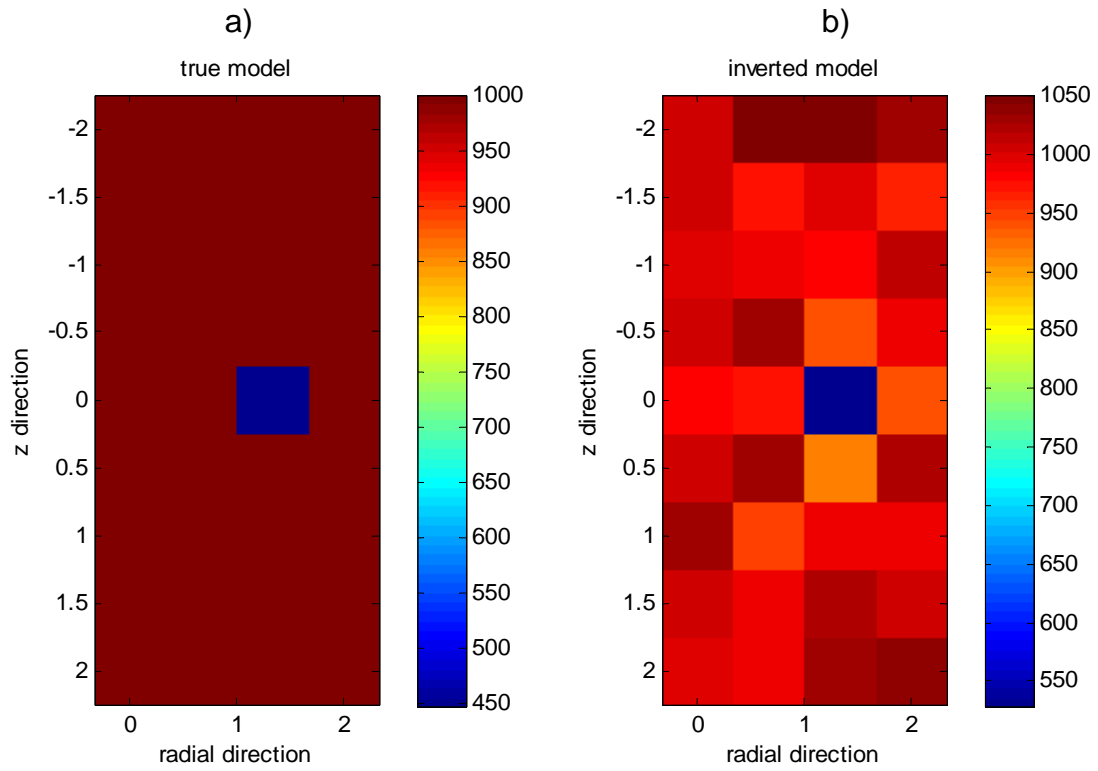


Figure 4-12. Homogeneous model with ring-type anomaly (near): a) True model, b) Inverted model, and c) Waveform match and convergence curve



c)

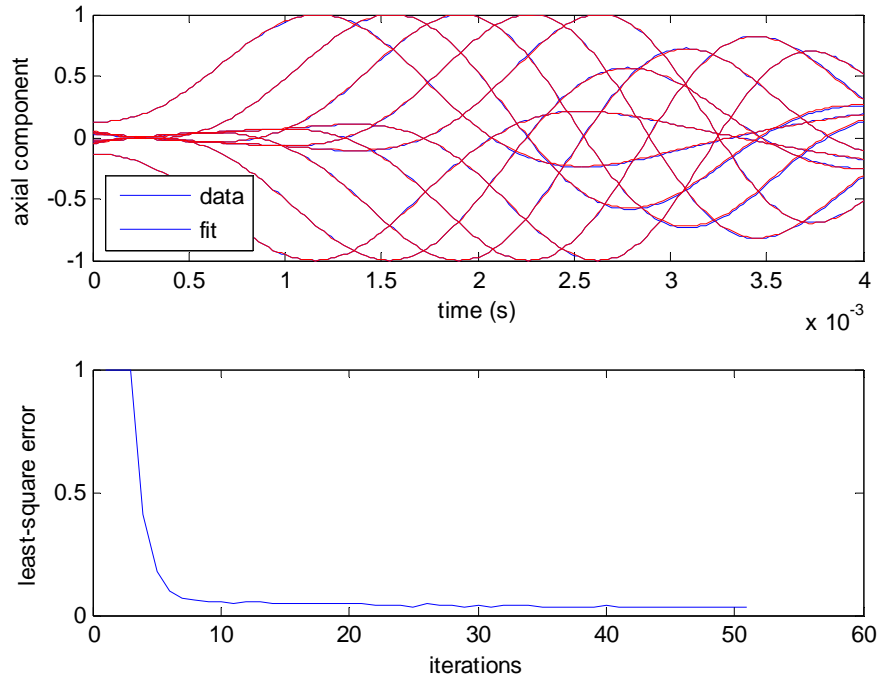


Figure 4-13. Homogeneous model with ring-type anomaly (far): a) True model, b) Inverted model, and c) Waveform match and convergence curve

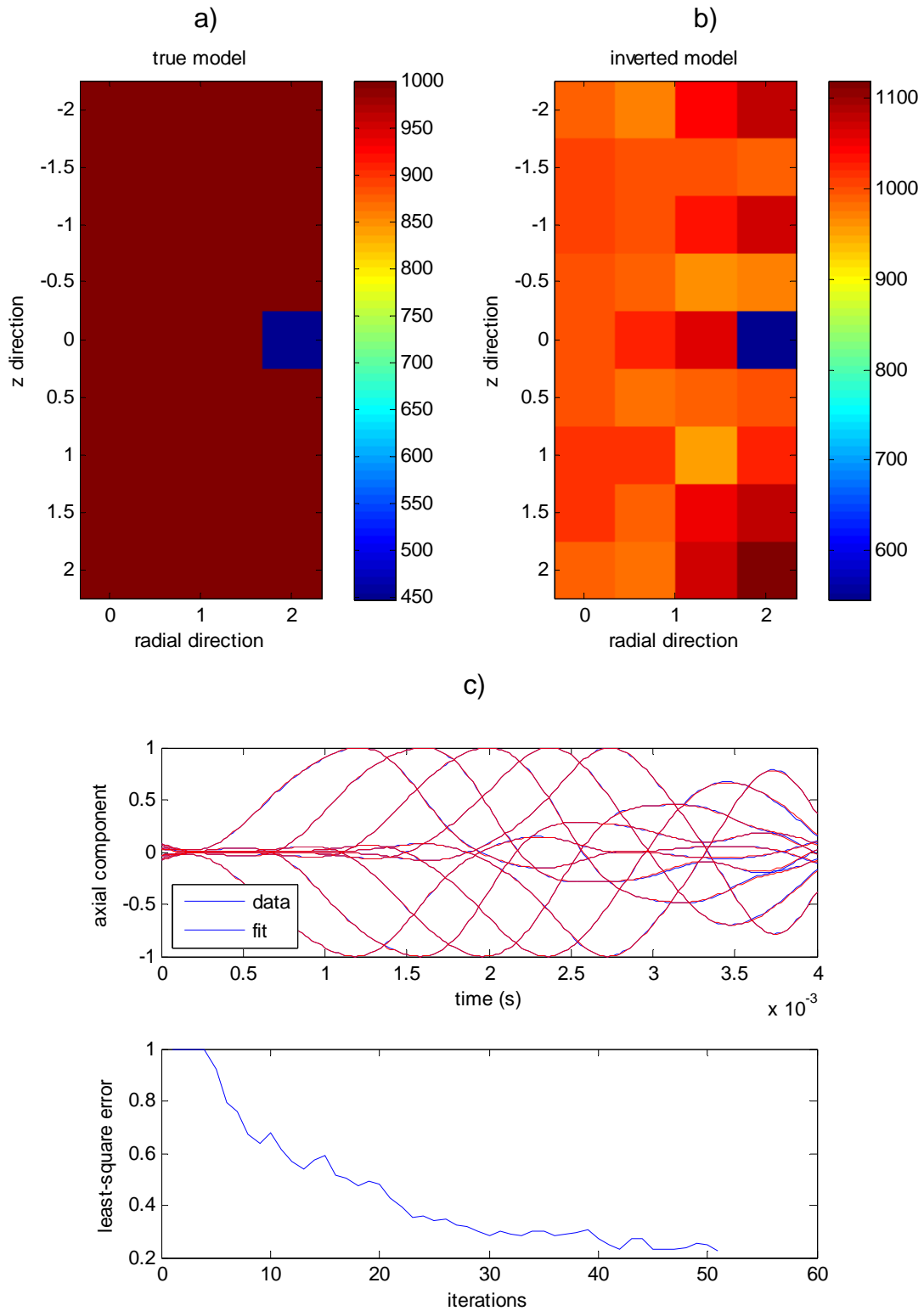
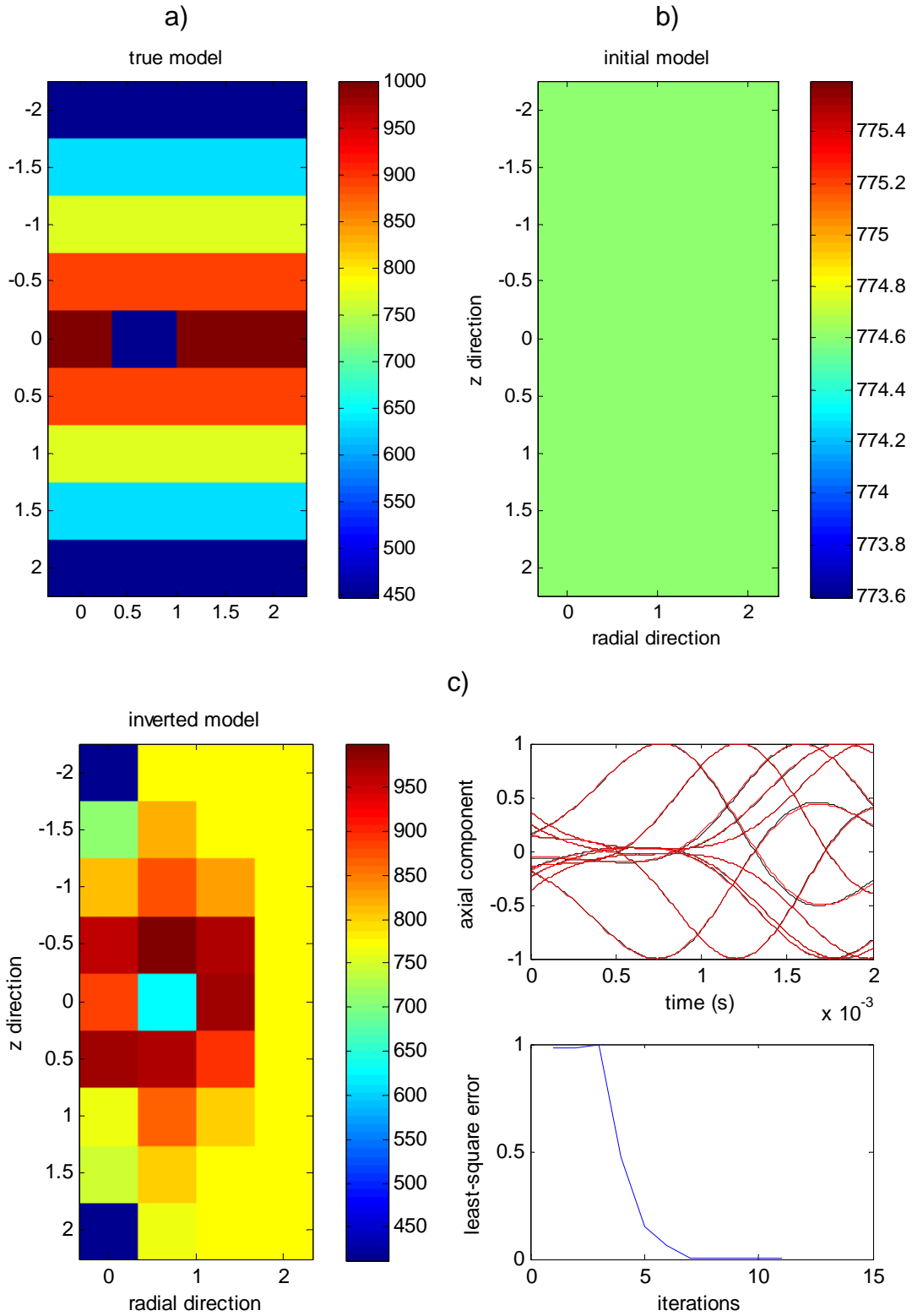


Figure 4-14. Homogeneous model with ring-type anomaly (farther): a) True model, b) Inverted model, and c) Waveform match and convergence curve



(Figure 4-15 is continued in the next page)

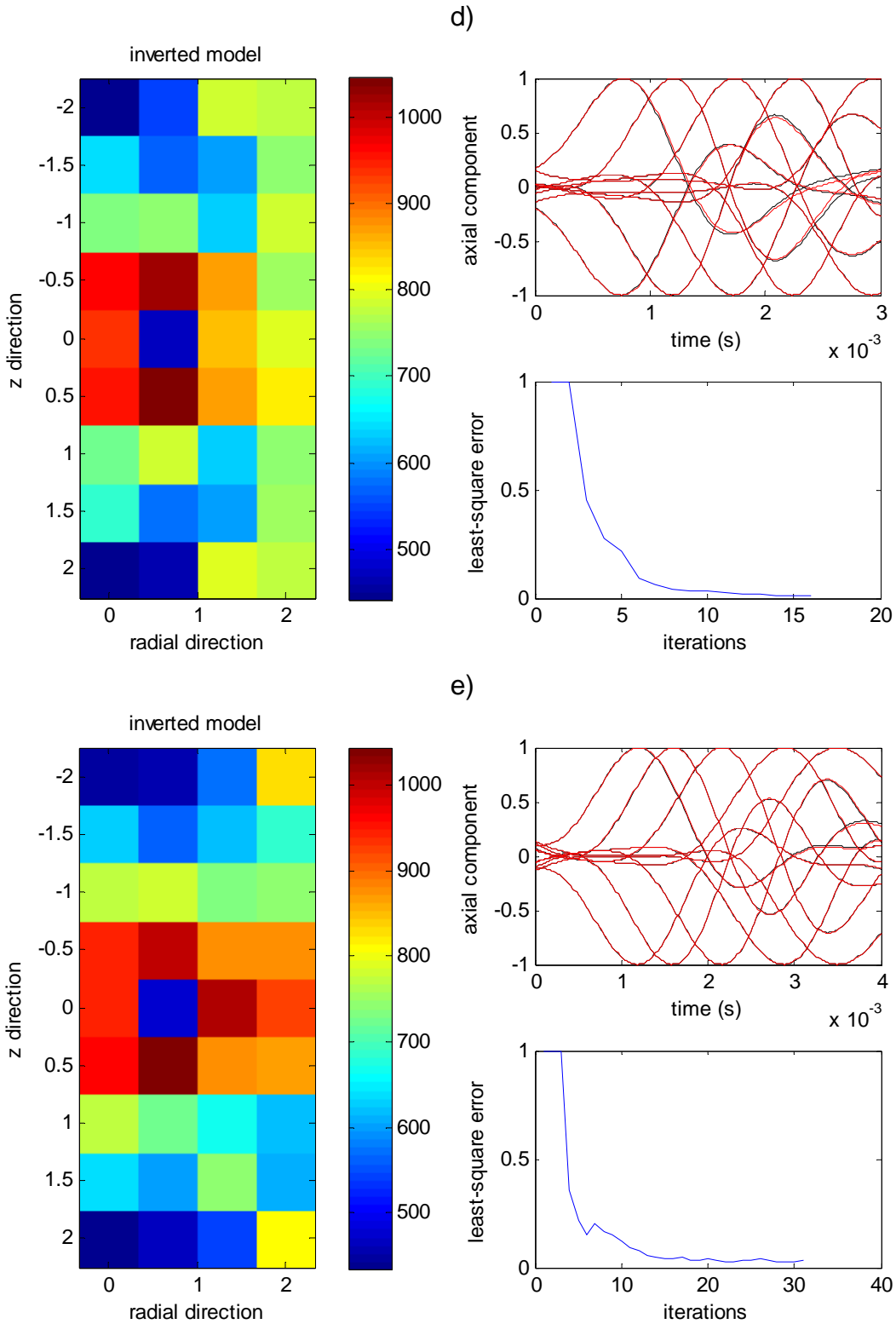


Figure 4-15. Horizontally layered model with ring-type anomaly: a) True model, b) Inverted model, c) Inversion for short time window, d) Inversion for medium time window, and e) Inversion for full time window

CHAPTER 5 LOCATING ISOLATED ANOMALIES NEAR A BOREHOLE

5.1 Introduction

The design and construction of deep foundations in karst terrain require special consideration, as the subsurface conditions are often highly variable, and characterized by sinkholes and cavities, as well as voids filled with water, air, or low-velocity materials. These anomalies are typically irregular in shape, variable in composition, and isolated in space. Characterizing these anomalies is a 3-D problem, and ideally requires a truly 3-D inversion. However, as stated above, 3-D borehole-based FWI is beyond the scope of this work. Therefore, this study attempted the proposed inversion scheme, based on an axisymmetric forward model, as an approximation to identify isolated anomalies in the vicinity of a borehole. To this end, this research conducted comprehensive synthetic model studies to establish the feasibility of the proposed imaging technique for detecting cavities and delineating in the vicinity of a rock socket.

5.2 Overview of Strategies

As noted above, FWI problems involving borehole data are highly nonlinear, and the solutions are generally non-unique. Therefore, a multiscale strategy using frequency filtering and time windowing is imperative for a successful inversion that starts with a reasonable initial model and is not prone to getting trapped in the local minima. This research proposes two additional strategies for characterizing isolated anomalies in the vicinity of a borehole.

5.2.1 Inversion with Multi-component Data

Axial (tangential) components of particle displacements were inverted throughout this report. Radial (perpendicular) components, on the other hand, may be added to the

data set to further constrain the inversion, as large impedance contrast between the cavity and its surrounding media would create a considerable amount of reflected energy (reflection and backscattering). Theoretically, this energy can be more readily detected by the radial component if the source is an omnidirectional stress pulse. In this study, unfortunately, the radial displacements derived from the 3-D models did not compare favorably with those predicted from the forward model, and hence were not included in the Inversion.

5.2.2 Inversion with Multi-bandwidth Sources

This study used a seismic source with varying frequency content in order to improve model recovery. In general, a low-frequency source penetrates deeper into the formation, thus providing a more defined skeleton of the model. However, when the dominating wavelength of the propagating waves is larger than or comparable to the size of the anomaly, diffraction allows the waves to pass the anomaly with little or no reflected energy. Since the reflected energy is critical for cavity detection, a high-frequency source (Figure 4-3a) is first applied in the inversion, followed by a low-frequency source (Figure 4-3b).

5.2.3 Inversion from Multiple Planes and with Multiple Shots

In blind tests, the location of the anomaly is unknown. Therefore, the experiment design (Figure 2-10) is critical in identifying the anomaly and characterizing its depth, size, and azimuth. The following synthetic model studies used three viewing planes – 0, 90, and 180 degrees with respect to the plane in which the anomaly is embedded – to locate the anomaly at a known location near a borehole. Once the anomaly is roughly identified, multiple shot gathers can be collected in that particular plane in order to

increase the spatial resolution of the inverted model, as the degree of non-uniqueness in the solution can be greatly reduced through the use of sensitive data.

5.3 Synthetic Model Studies

Synthetic model studies were conducted to evaluate the feasibility of the proposed imaging technique for locating isolated anomalies in the vicinity of a borehole. Anomalies were simplified as cavities (voids filled with air) in the 3-D borehole models, from which synthetic records were generated and treated as data for the inversions. As stated above, inversions were based on an axisymmetric borehole model, divided into 36 velocity cells (Figure 3-2). Because an inexact forward model was used to approximate the physical reality, some discrepancies between the inverted model and the true model were to be expected. This section investigated a single anomaly embedded in a homogeneous medium with varying distance away from the borehole wall in order to characterize its axial and radial dimensions and azimuth. Next, multiple anomalies embedded in the same plane and different planes were examined to evaluate the capability of the proposed imaging technique for locating multiple isolated anomalies around a borehole. Lastly, a single anomaly embedded in a multi-layered system was analyzed to test if the proposed imaging technique is capable of characterizing both the anomaly and individual layering.

5.3.1 Synthetic Model 1

First, a homogeneous model with an isolated anomaly near the borehole wall was studied. The anomaly was located 0.5 m from the wall and was modeled as a 0.5 m by 0.5 m cavity in the r-z plane and 0.5 m into the paper. Figure 5-1 shows the 3-D model and its cross-section at the 0-degree plane. The shear wave velocity was 1000 m/s for the homogeneous background and 0 m/s for the anomaly.

Using the test configuration shown in Figure 4-10, a uniform array of 10 receivers was used for data acquisition, with the nearest offset and trace interval being 0.5 m. The array was placed at 0-, 90-, and 180-degree planes simultaneously around the borehole wall. The inversion was carried out sequentially using three consecutive time windows: 2, 3, and 4 ms. For the first two time windows, a high-frequency source (Figure 4-3a) was used, and for the last time window, a low-frequency source (Figure 4-3b) was used. For each time window, only one low-pass filter was applied to the waveforms. The initial model was assumed to be homogeneous and having the same background velocity of 1000 m/s.

The inversion result of 0-degree plane (Figure 5-2) exhibited a sharp velocity contrast between the anomaly and background, which indicates the possible location of the anomaly in terms of axial and radial dimensions. The waveforms were reasonably well matched, and a good convergence rate was observed. Note that the recovered velocity of the anomaly was approximately 700 m/s, which is greater than the shear wave velocity of a cavity (0 m/s). This difference was due to the fact that only the Young's modulus was adjusted during inversion, while the Poisson's ratio and mass density were held constant. As a result, all velocity cells in the inversion model were elastic, while the data were generated by modeling the cavity as a boundary in the 3-D simulation. Another cause of the discrepancy was the use of an inexact forward model to approximate the 3-D reality. The anomaly shown in Figure 5-2 should be interpreted as a ring, while the true model only contains an isolated cavity embedded in the 0-degree plane. Nevertheless, it appears that an inversion based on the axisymmetric

forward model is able to determine the axial and radial dimensions of an isolated anomaly, as long as the receiver array is in the same plane as the anomaly.

The inversion results of 90-degree plane and 180-degree plane are presented in Figures 5-3 and 5-4, respectively. A sharp velocity contrast developed at exactly the same spot in both inversions, which implies that the receiver array can detect an isolated anomaly near a borehole no matter where it is placed on the wall circumference. It is arguable that the sharp velocity contrast was due to the axisymmetric forward model used for the inversion. However, considering the physics of wave propagation inside a borehole with an isolated anomaly, the reflected energy is first detected by the in-plane (0-degree plane) receivers, and then by the out-of-plane receivers (90-degree plane followed by 180-degree plane). Moreover, when waves are traveling quickly inside a small borehole, the difference in timing is so small that the reflected energy is detected as if the anomaly were directly in-plane. This explains why in the out-of-plane images the velocity contrast is observed at the same location compared to the in-plane image. However, a careful examination of the recovered images reveals that the contrast between the anomaly and background weakens as the relative angle between the anomaly and the viewing plane widens. For example, the inverted shear wave velocity was approximately 780 m/s for the 180-degree plane, and approximately 740 m/s for the 90-degree plane, as compared to 700 m/s for the 0-degree plane. This relationship is appropriate because the reflected energy attenuates as it propagates away from the anomaly, which in this case is an important indicator of where the anomaly was possibly oriented. Therefore, it appears that the proposed

imaging technique has the potential to determine both the axial and radial dimensions and the azimuth of an isolated anomaly in the vicinity of a borehole.

5.3.2 Synthetic Model 2

The next model considered in this study was a homogeneous model with an isolated anomaly slightly farther from the borehole wall. In this case, the anomaly was located 1.0 m from the wall. The anomaly was modeled as a 0.5 m by 0.5 m cavity in the r - z plane and 0.5 m into the paper. Figure 5-5 shows the 3-D model and its cross-section at the 0-degree plane. The shear wave velocity was 1000 m/s for the background and 0 m/s for the anomaly.

The same acquisition geometry and seismic sources were used as in Synthetic Model 1. The inversion was carried out sequentially using the same initial model. The final inversion results from various viewing planes are presented in Figures 5-6 through 5-8. The predicted waveforms were in good agreement with the data, and a velocity contrast developed inside a relatively uniform background for all viewing planes. The axial and radial dimensions of the anomaly can be identified as the point at which the contrast developed, while the azimuth of the anomaly can be inferred by comparing the contrast level with the background of various viewing planes. The inverted velocity of the anomaly was approximately 820, 850, and 880 m/s for the 0-, 90-, and 180-degree planes, respectively, and the color scale ranged from 800 m/s to 1050 m/s. The inverted velocity of the anomaly was greater than it was in the previous case, because the anomaly in this case was embedded deeper from the boundary of observation, resulting in weaker reflected/scattered energy to the receiver array. Despite the fact that the velocity contrast is not as sharp as desired, and that some smearing occurred around

the anomaly in the recovered image, the proposed imaging technique still holds the potential to find indications of an isolated anomaly in a 3-D space.

5.3.3 Synthetic Model 3

The third model investigated in this study was a homogeneous model with two isolated anomalies embedded in the same plane. Each anomaly was modeled as a 0.5 m by 0.5 m cavity in the r - z plane and 0.5 m into the paper. The lower anomaly was 0.5 m away from the wall, while the upper anomaly was placed 1.0 m away from the wall. The 3-D model and its cross-section at the 0-degree plane are shown in Figure 5-9. Again, the shear wave velocity was 1000 m/s for the background and 0 m/s for the anomaly.

The same acquisition geometry and inversion procedure was used for this model. The final inversion results are presented in Figures 5-10 through 5-12. For the 0-degree plane view, two contrasts occurred (Figure 5-10). The inverted shear wave velocities were approximately 750 m/s for the lower anomaly and 850 m/s for the upper anomaly. Similar to the previous examples, the velocity contrast was relatively sharp for the near (lower) anomaly and weak for the deep (upper) anomaly. The homogeneous background was not recovered perfectly, especially in cells surrounding the anomaly. In fact, the incompatibility between model and data under the waveform-matching algorithm caused the inversion artifact.

For the 90-degree plane view, only the lower anomaly was visible in the recovered image (Figure 5-11). Moreover, the contrast level was very weak in that the inverted velocity of the anomaly was approximately 875 m/s, while the inverted velocity of the background ranged from 950 m/s to 1050 m/s. The upper anomaly in this case was not distinguishable, despite the fact that the waveforms were reasonably well

matched, which suggests that the scattered wavefield was weak in the presence of multiple isolated anomalies, and that one shot in the middle of the array was not enough to achieve the desired resolution (previous research predicted that both anomalies would be visible in the image with weaker contrast).

For the 180-degree plane view, a fairly uniform velocity model was reconstructed (Figure 5-12). The inverted shear wave velocity ranged from 950 m/s to 1050 m/s, while the true background velocity was 1000 m/s, which implies that the 180-degree-out-of-plane receiver array is simply “blind” to the 0-degree plane anomalies and can only “see” what is within the plane – a homogenous background in this case. The waveforms comparison also confirms that the scattered wavefield was weak in the presence of multiple isolated anomalies. In other words, the data used in the inversion were not sufficiently sensitive to infer the internal structure of the model. Nonetheless, the fact that only the in-plane receivers could detect the anomalies simplified the interpretation and characterization processes, and demonstrated the value of the proposed multi-plane waveform inversion.

5.3.4 Synthetic Model 4

The research next investigated a homogeneous model with two isolated anomalies embedded in the opposite planes. Each anomaly was modeled as a 0.5 m by 0.5 m cavity in the r - z plane and 0.5 m into the paper. The lower anomaly was embedded in the 0-degree plane, and the upper anomaly was embedded in the 180-degree plane. Both anomalies were placed 0.5 m away from the wall. The 3-D model and the velocity cross-sections are presented in Figures 5-13 and 5-14. The shear wave velocity was 1000 m/s for the background and 0 m/s for the anomaly.

The same acquisition geometry and inversion procedure was used for this model. The final inversion results are presented in Figures 5-15 through 5-17. For the 0-degree plane view, the in-plane, lower anomaly was clearly visible, while the out-of-plane, upper anomaly was not visible (Figure 5-15). The inverted shear wave velocity of the anomaly was approximately 725 m/s. For the 90-degree plane view (Figure 5-16), both anomalies were visible, as well as some artifact in the middle of the image. The inverted shear wave velocity of the anomaly was in the range of 850–875 m/s. For the 180-degree plane view, the in-plane, upper anomaly was clearly visible, while the out-of-plane, lower anomaly was not characterized in the image (Figure 5-17). The inverted shear wave velocity of the anomaly was approximately 725 m/s. Note that the reconstructed images shown in Figure 5-15 and 5-17 are near perfect reflections of each other, due to the symmetry in the true model (Figure 5-13). For this reason, the reconstructed image shown in Figure 5-16 is also symmetric with respect to the horizontal centerline. For each case presented herein, the waveforms were in good agreement with the data, and the convergence rate was reasonable. These results indicate that the proposed imaging technique can potentially identify isolated anomalies embedded in different planes by performing multi-plane waveform inversions.

However, previous research indicates that sufficiently sensitive data should characterize even out-of-plane anomalies so that they are visible in the recovered images. Past findings also reveal that the way to infer azimuth is to compare the contrast level with the background of various viewing planes. Therefore, in the next set of experiments, two shot gathers were collected and used as data in the inversion to

validate the hypothesis. For the purpose of demonstration, these two shots were placed directly adjacent to the anomalies of interest, i.e., at $z=1$ and $z=-1$ m.

Figure 5-18 presents the final inverted model for the 0-degree plane view using two shots, in which both anomalies were characterized. The inverted shear wave velocity of the in-plane, lower anomaly was approximately 725 m/s, whereas the inverted shear wave velocity of the 180-degree-out-of-plane, upper anomaly was approximately 775 m/s. Figure 5-19 presents the final inverted model for the 90-degree plane view using two shots. In this case, both anomalies are considered out-of-plane and are clearly visible in the image. The inverted shear wave velocity was approximately 700 m/s. Figure 5-20 presents the final inverted model for the 180-degree plane view using two shots. Once again, both anomalies were well characterized in the image. The inverted shear wave velocity of the in-plane, upper anomaly was approximately 725 m/s, while that of the 180-degree-out-of-plane, lower anomaly was approximately 800 m/s. These results appear to be in good agreement with the hypothesis that the inverted shear wave velocity of the anomalies under the out-of-plane views would be greater than that of the anomalies under the in-plane views.

5.3.5 Synthetic Model 5

Finally, this research analyzed an isolated anomaly embedded in a multi-layered system in order to test whether the proposed imaging technique is capable of characterizing the isolated anomaly, as well as the individual layering. Note that a ring-shaped anomaly was previously investigated in the same layered system, in which the shear wave velocity varied gradually from 450 m/s at the top, to 1000 m/s in the middle, and back to 450 m/s at the bottom. The anomaly was located 0.5 m away from the wall

and modeled as a 0.5 m by 0.5 m cavity in the r - z plane and 0.5 m into the paper.

Figure 5-21 presents the 3-D model and the velocity section at the 0-degree plane.

A uniform shear wave velocity of 775 m/s was selected as the initial model. Following the proposed multiscale approach, the inversion was carried out sequentially using three consecutive time windows: 2, 3, and 4 ms. A high-frequency source (Figure 4-3a) was used for the first two time windows and a low-frequency source (Figure 4-3b) was used for the last time window. For each time window, only one low-pass filter was applied to the waveforms.

The final inverted models from multiple viewing planes are presented in Figures 5-22 through 5-24. In general, the layered structure was successfully delineated for all viewing planes. The associated waveforms were very well matched in the time domain, and a high level of convergence was observed. Some smearing is visible around the anomaly, which occurred because of the incompatibility between model and data, discussed above. In addition, data insensitivity prevented good velocity recovery at the far ends of the model. For the isolated anomaly of interest, the inverted shear wave velocity was approximately 600, 750, and 850 m/s for 0-, 90-, and 180-degree planes, respectively. The fact that the anomaly is more readily identifiable from the in-plane view than the out-of-plane views is in agreement with previous findings. This example demonstrates that the proposed imaging technique is capable of locating an isolated anomaly embedded in a multi-layered system, and highlights the importance of the proposed multi-plane data acquisition and inversion.

5.4 Summary

Synthetic model studies demonstrate that the proposed imaging technique is capable of finding indications of isolated anomalies in the vicinity of a borehole. The

number of anomalies and their axial and radial dimensions can be accurately determined from the recovered images, while the azimuth of anomalies can be inferred by examining the level of contrast against the background in the images recovered from multi-plane waveform inversions.

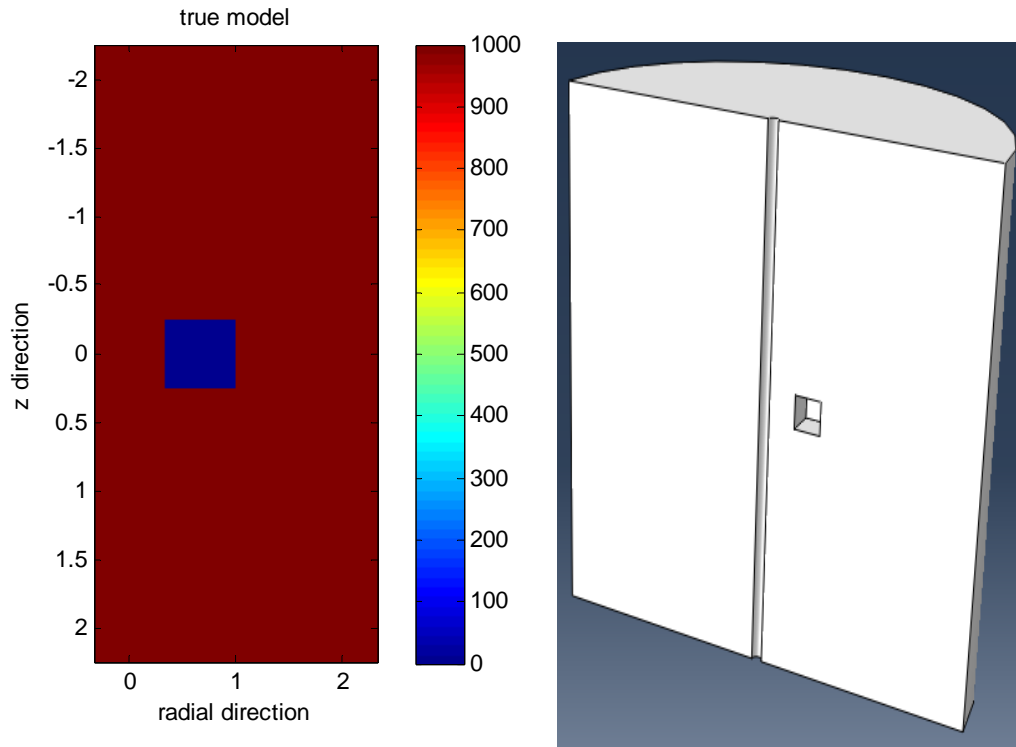


Figure 5-1. Synthetic model 1: true model and velocity section

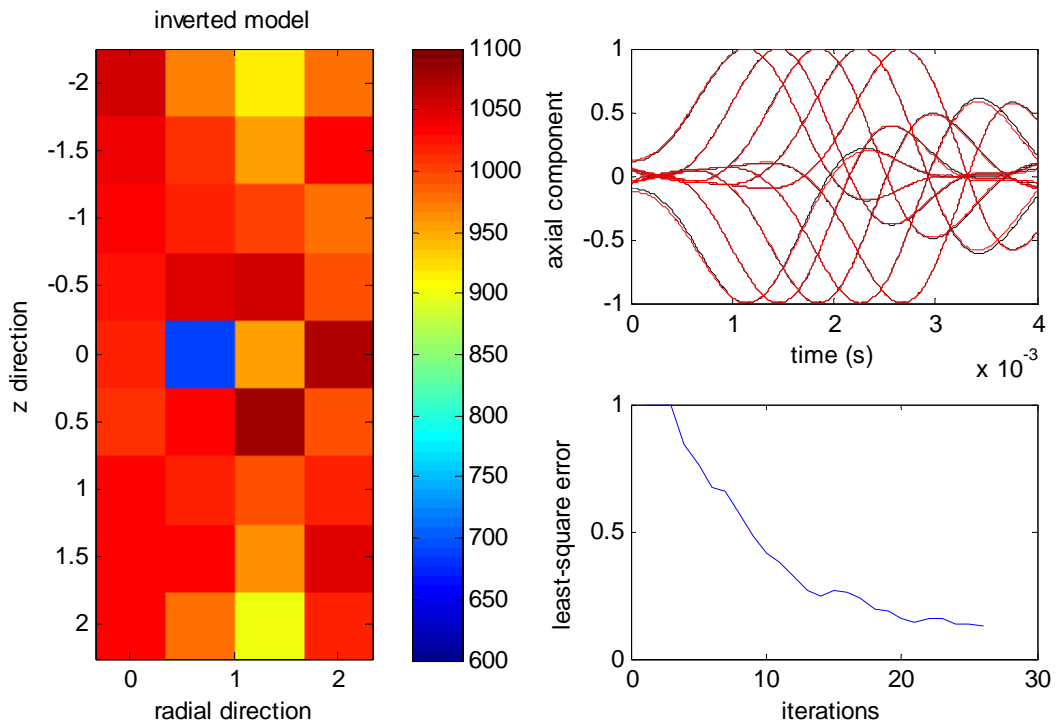


Figure 5-2. Synthetic model 1: inversion result of 0-degree plane

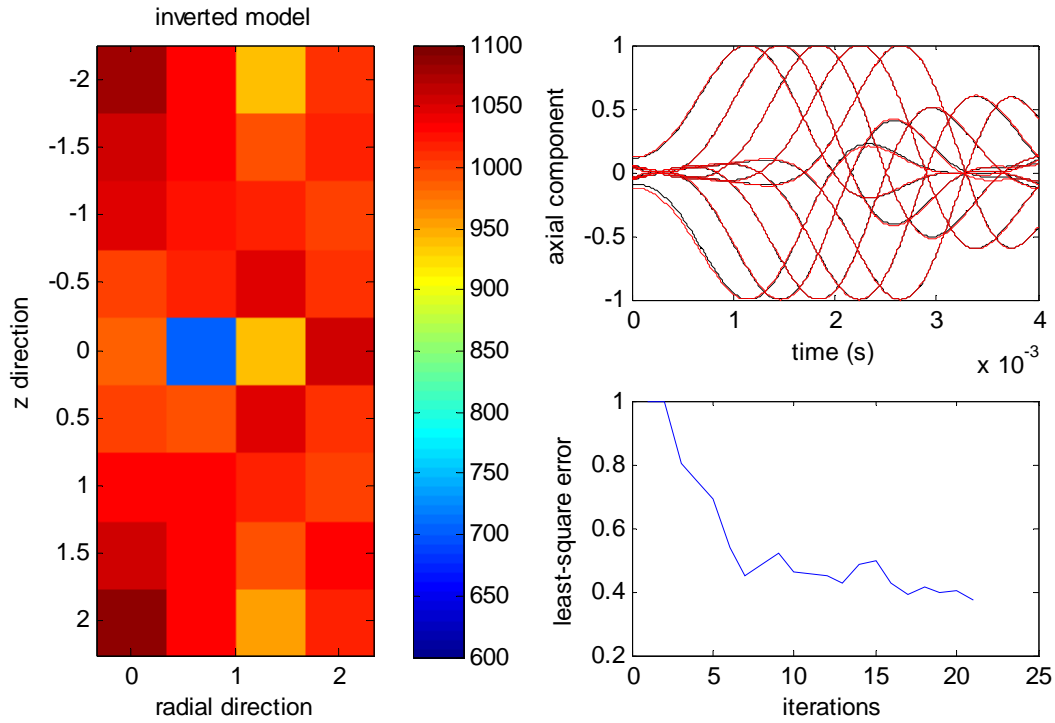


Figure 5-3. Synthetic model 1: inversion result of 90-degree plane

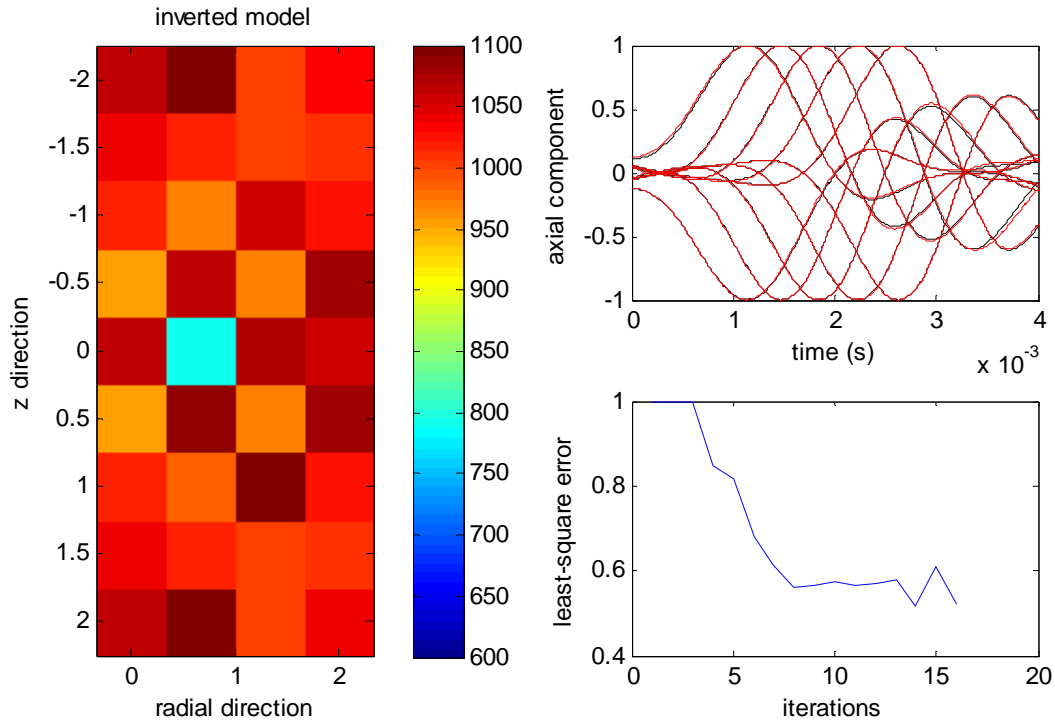


Figure 5-4. Synthetic model 1: inversion result of 180-degree plane

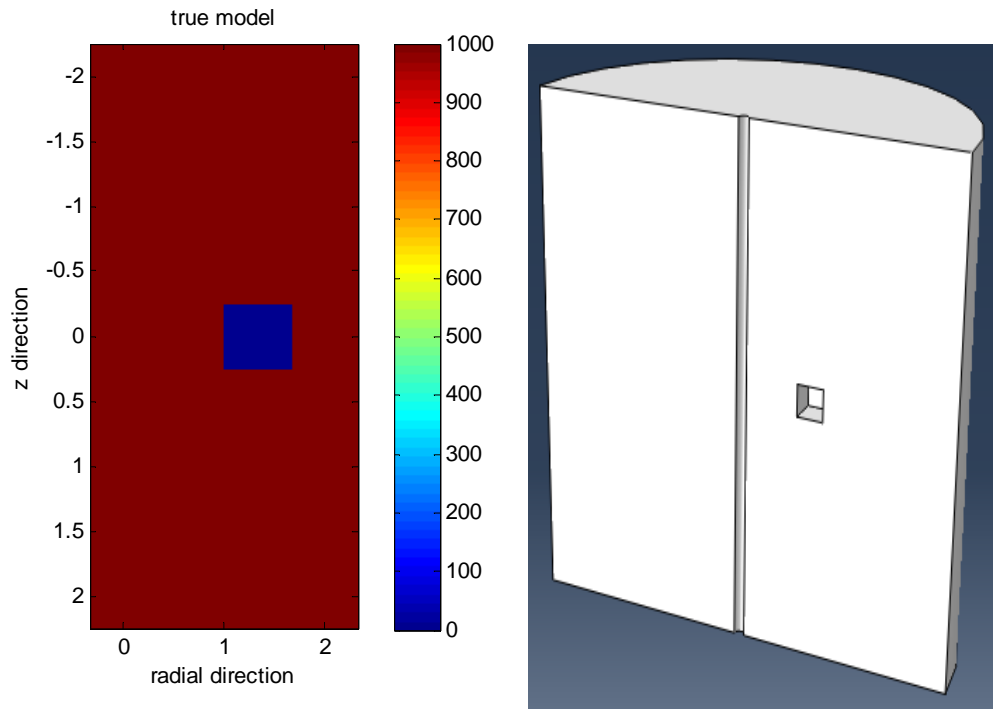


Figure 5-5. Synthetic model 2: true model and velocity section

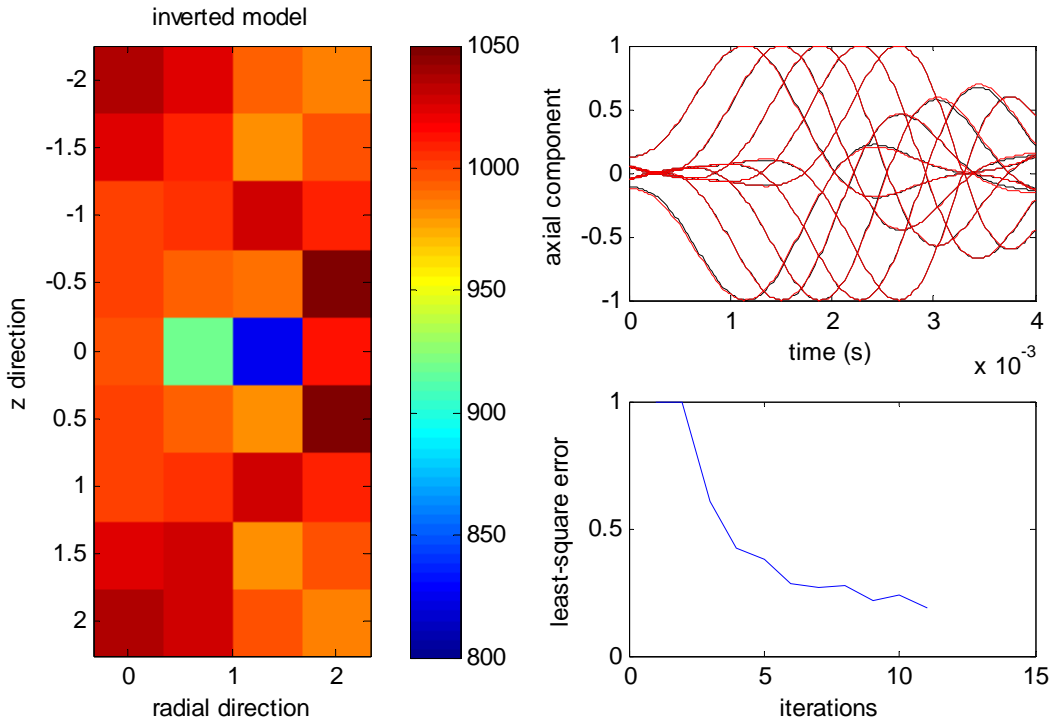


Figure 5-6. Synthetic model 2: inversion result of 0-degree plane

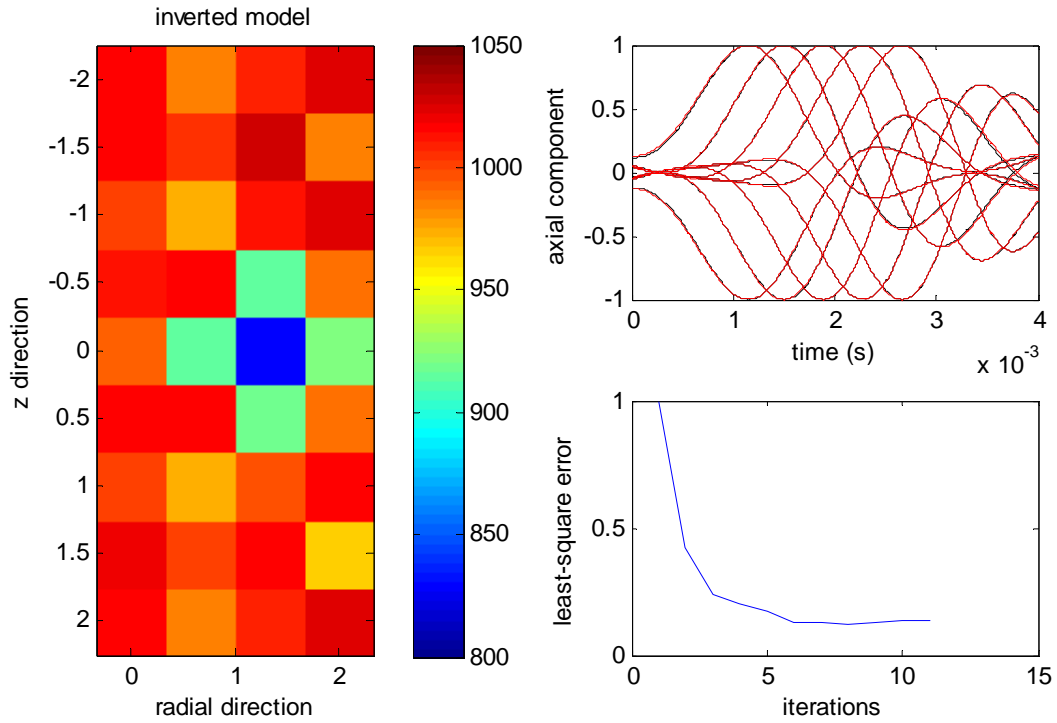


Figure 5-7. Synthetic model 2: inversion result of 90-degree plane

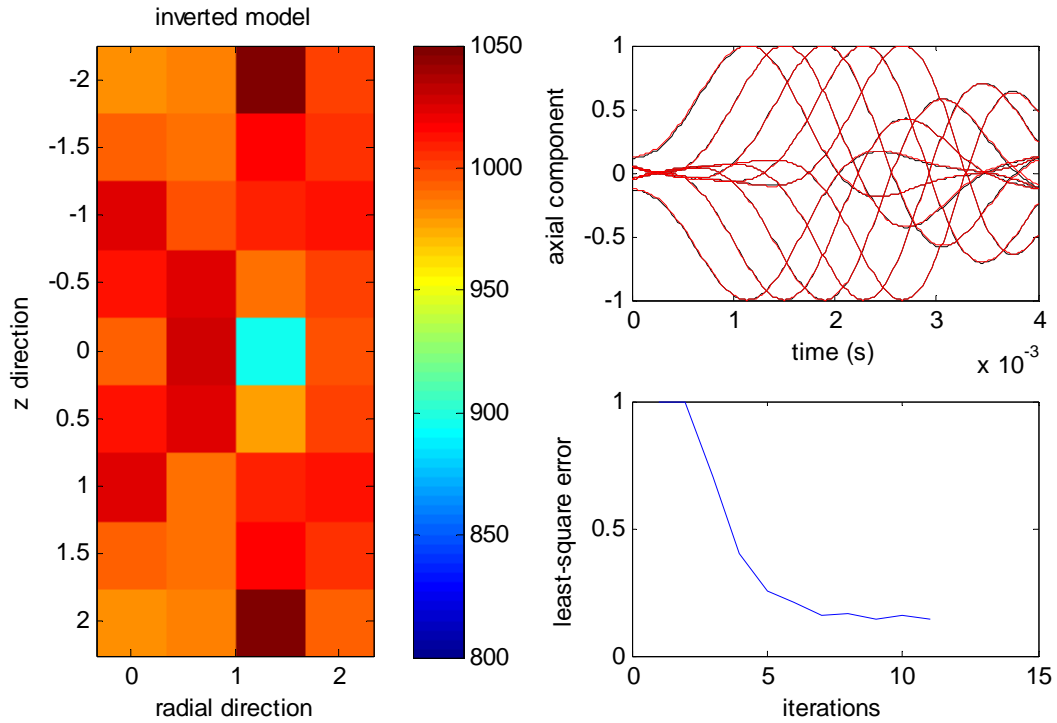


Figure 5-8. Synthetic model 2: inversion result of 180-degree plane

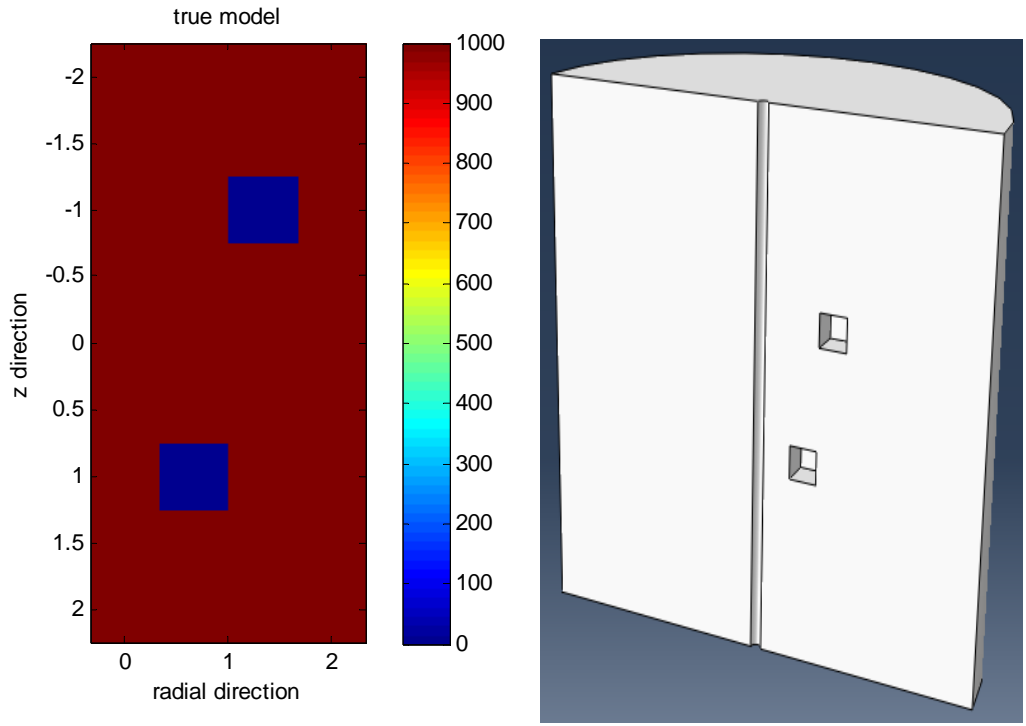


Figure 5-9. Synthetic model 3: true model and velocity section

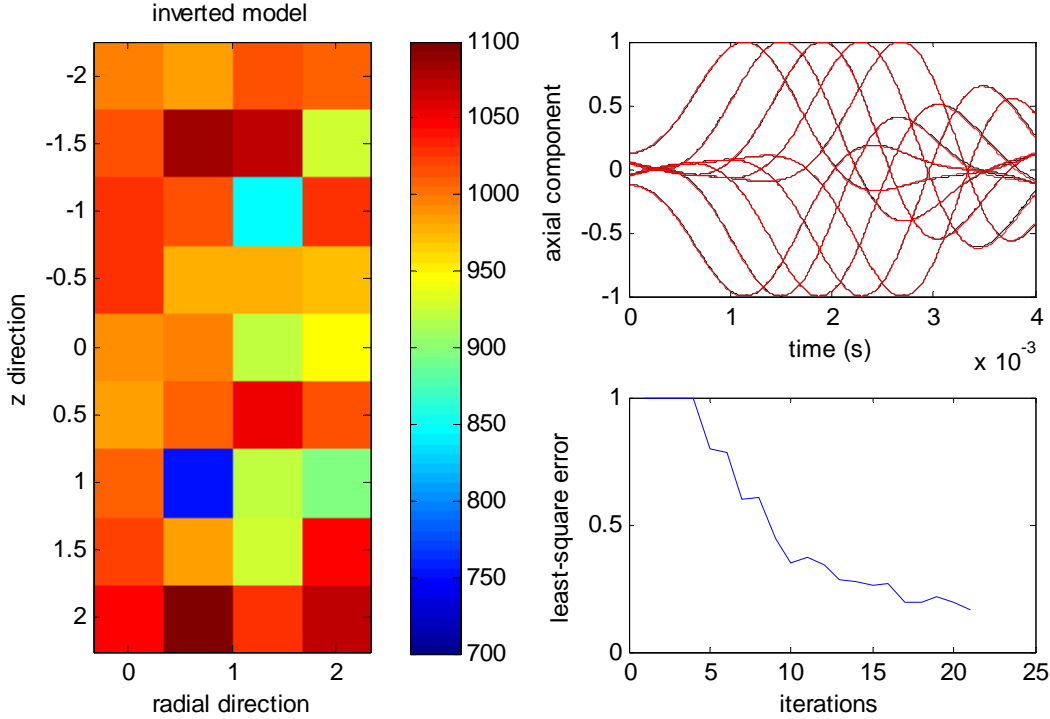


Figure 5-10. Synthetic model 3: inversion result of 0-degree plane

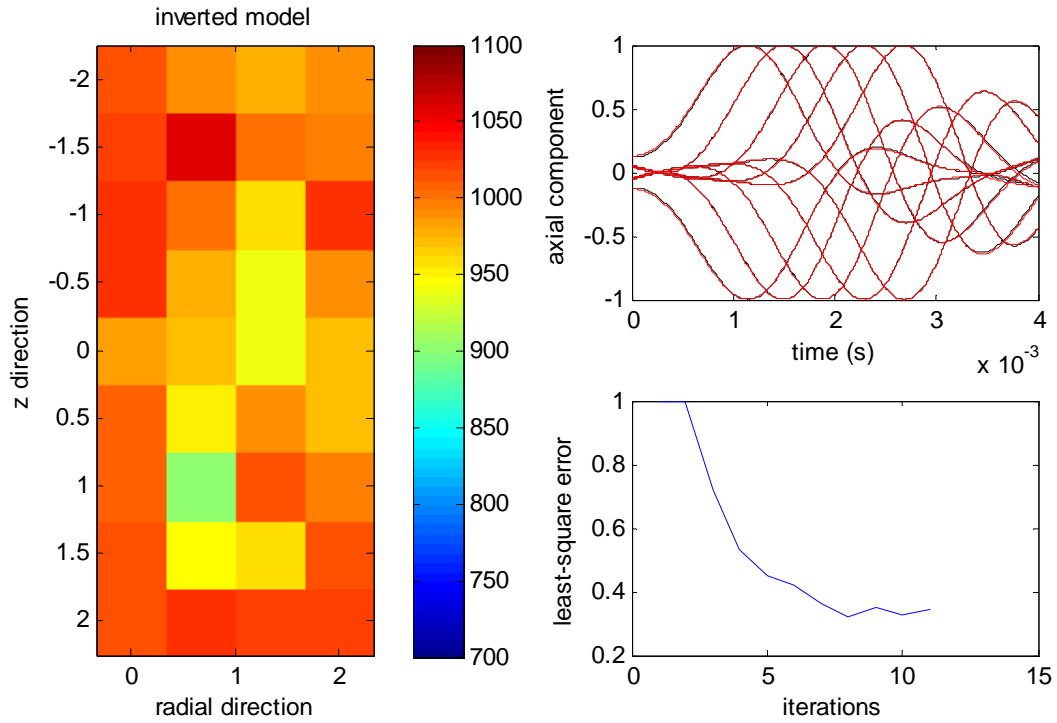


Figure 5-11. Synthetic model 3: inversion result of 90-degree plane

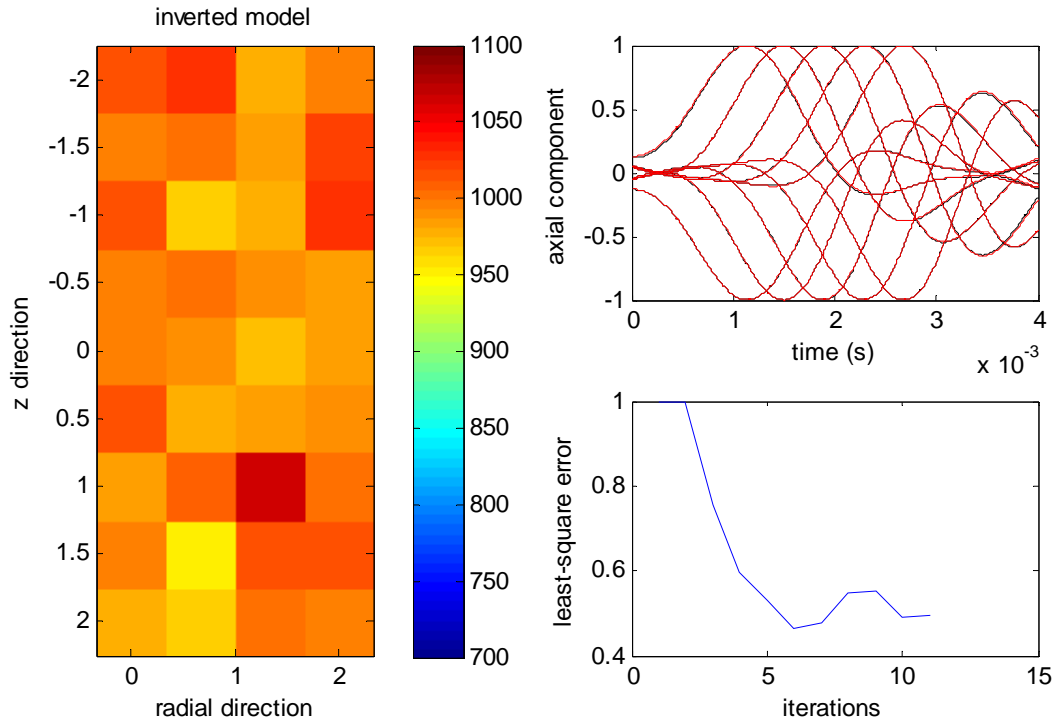


Figure 5-12. Synthetic model 3: inversion result of 180-degree plane

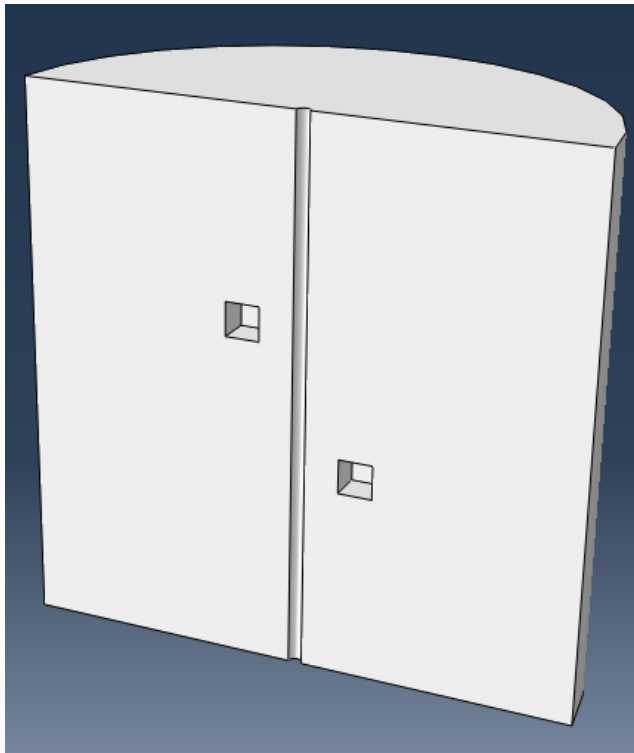


Figure 5-13. Synthetic model 4: true model

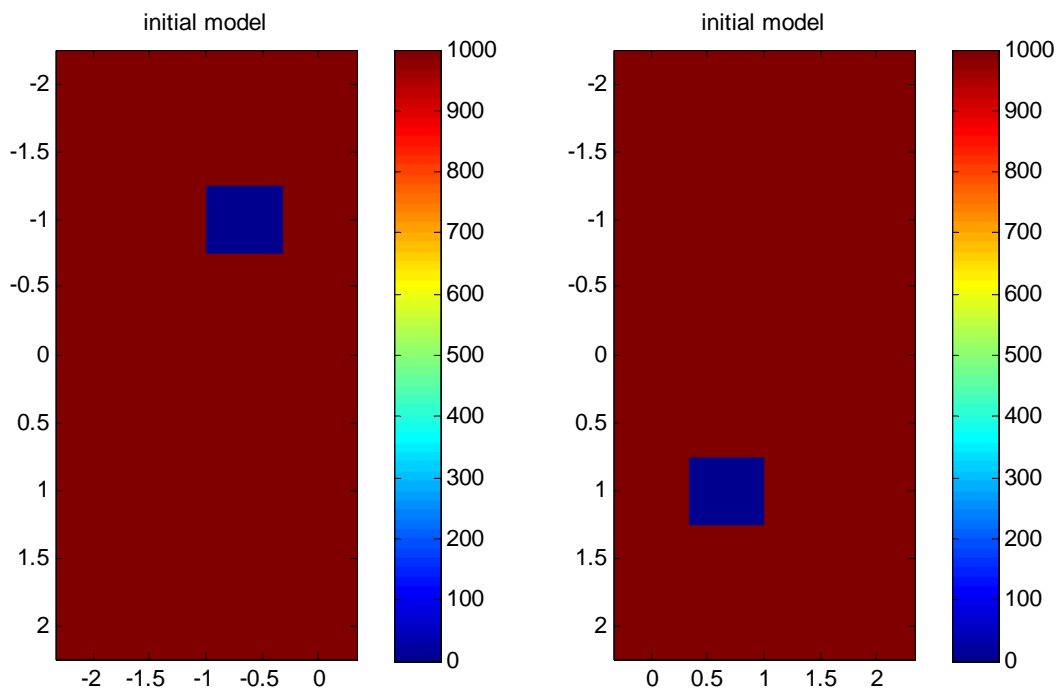


Figure 5-14. Synthetic model 4: velocity section of 0–180-degree plane

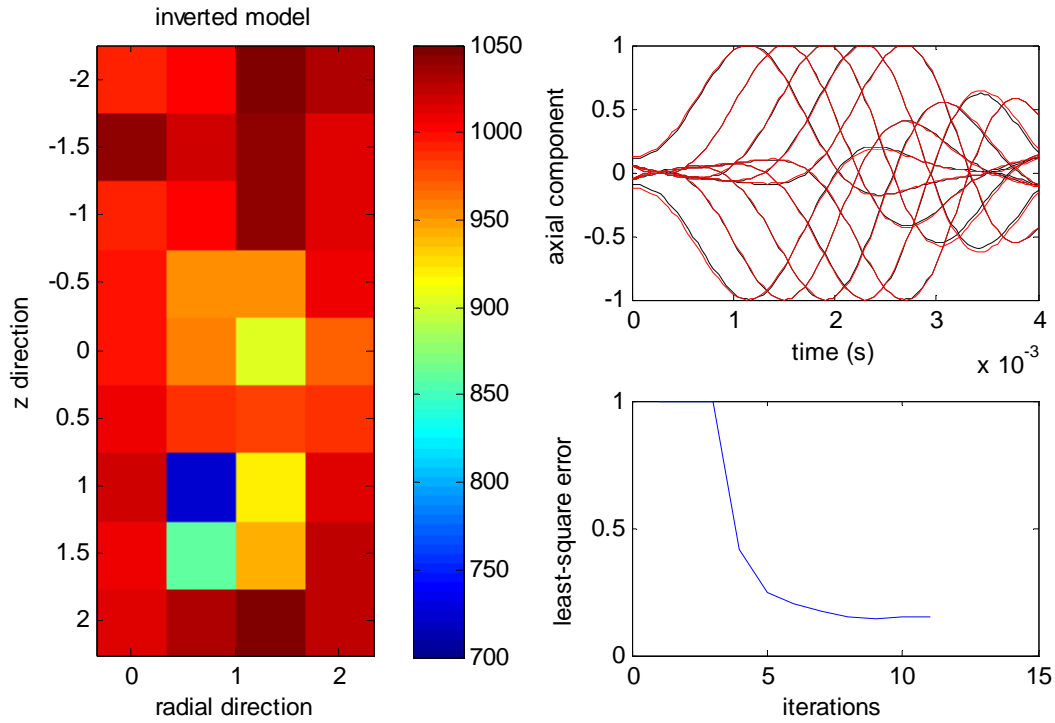


Figure 5-15. Synthetic model 4: inversion result of 0-degree plane with one shot

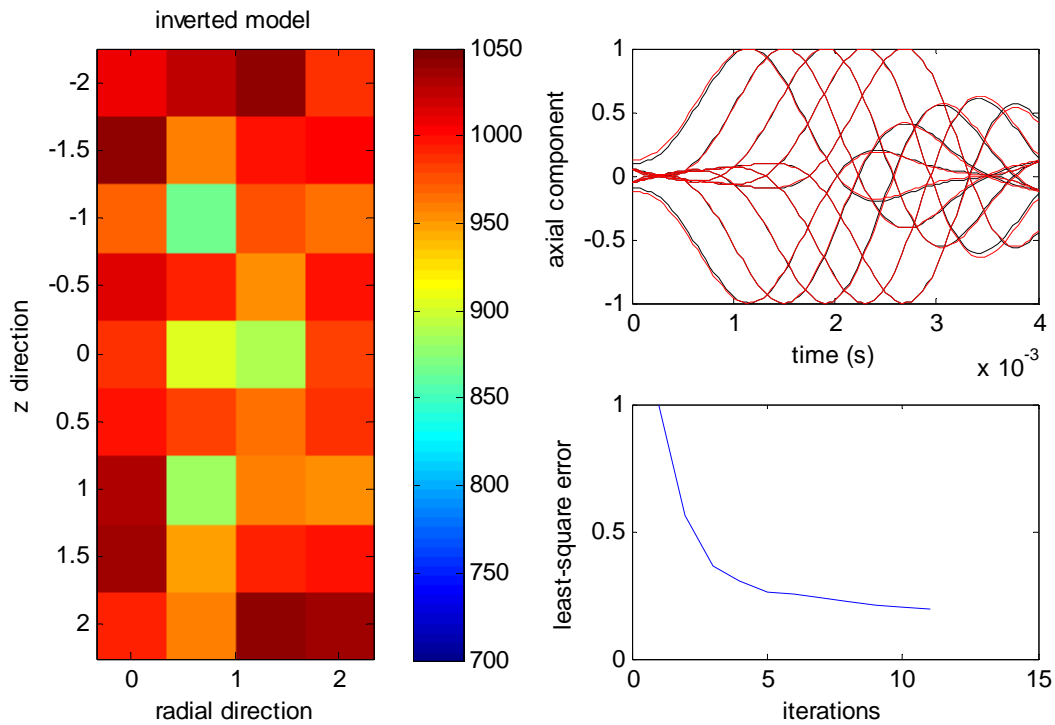


Figure 5-16. Synthetic model 4: inversion result of 90-degree plane with one shot

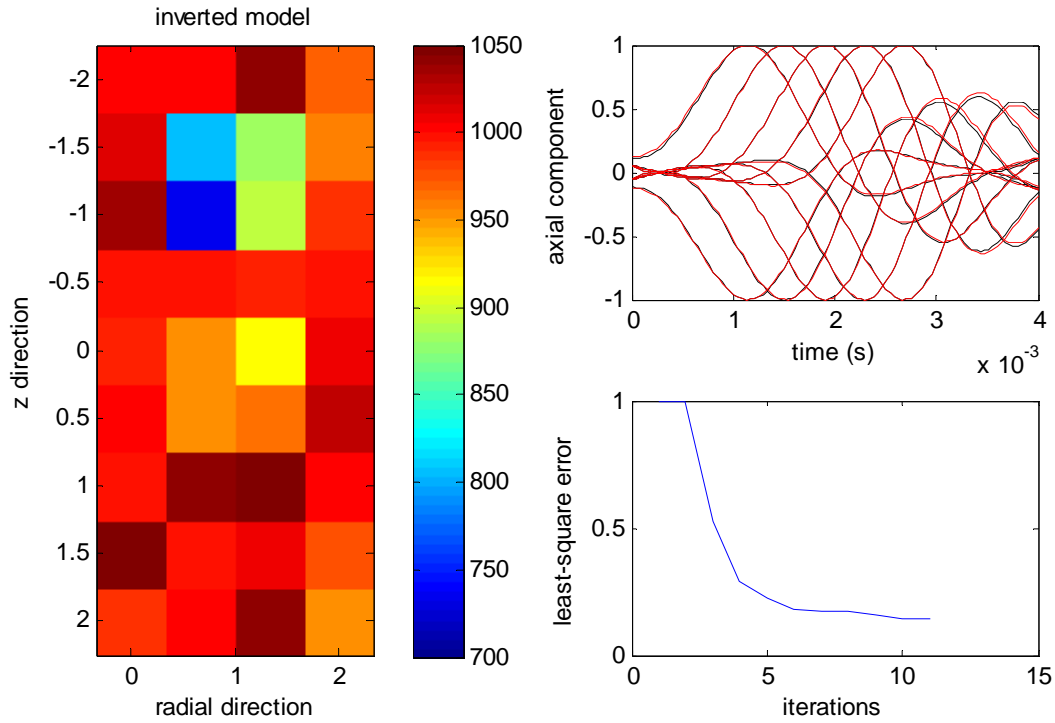


Figure 5-17. Synthetic model 4: inversion result of 180-degree plane with one shot

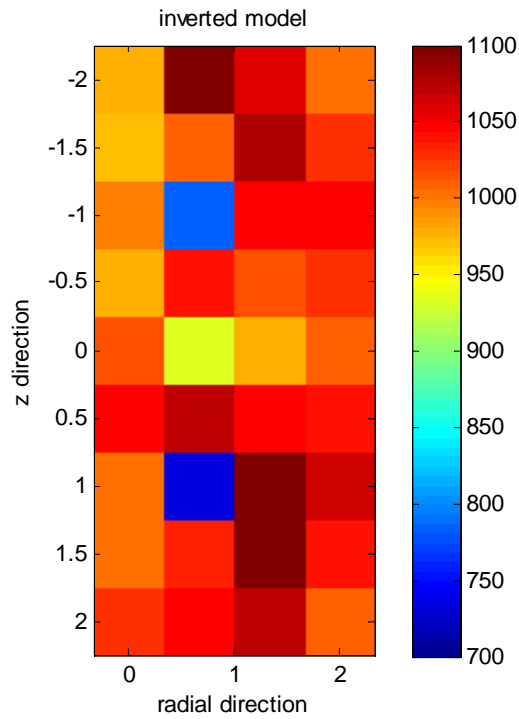


Figure 5-18. Synthetic model 4: inversion result of 0-degree plane with two shots

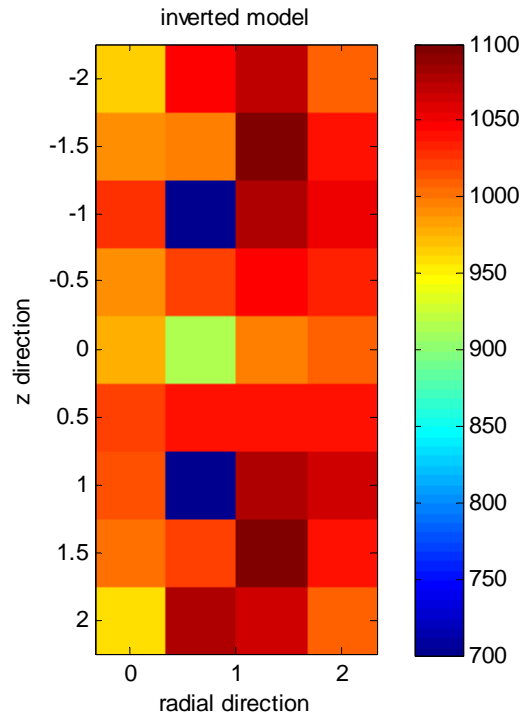


Figure 5-19. Synthetic model 4: inversion result of 90-degree plane with two shots

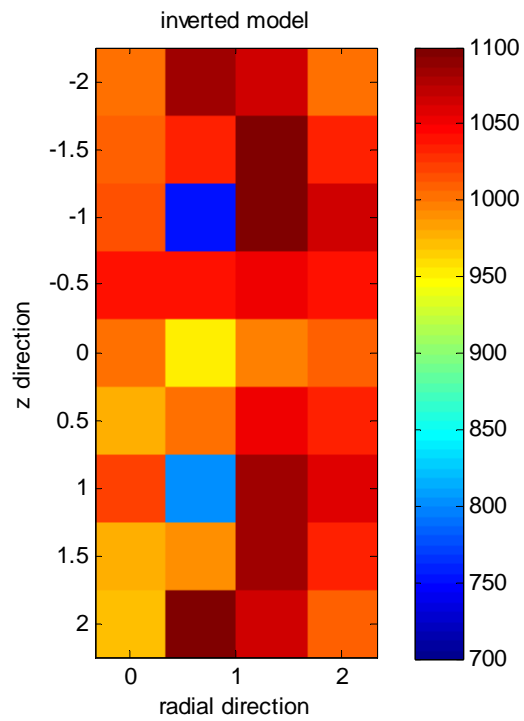


Figure 5-20. Synthetic model 4: inversion result of 180-degree plane with two shots

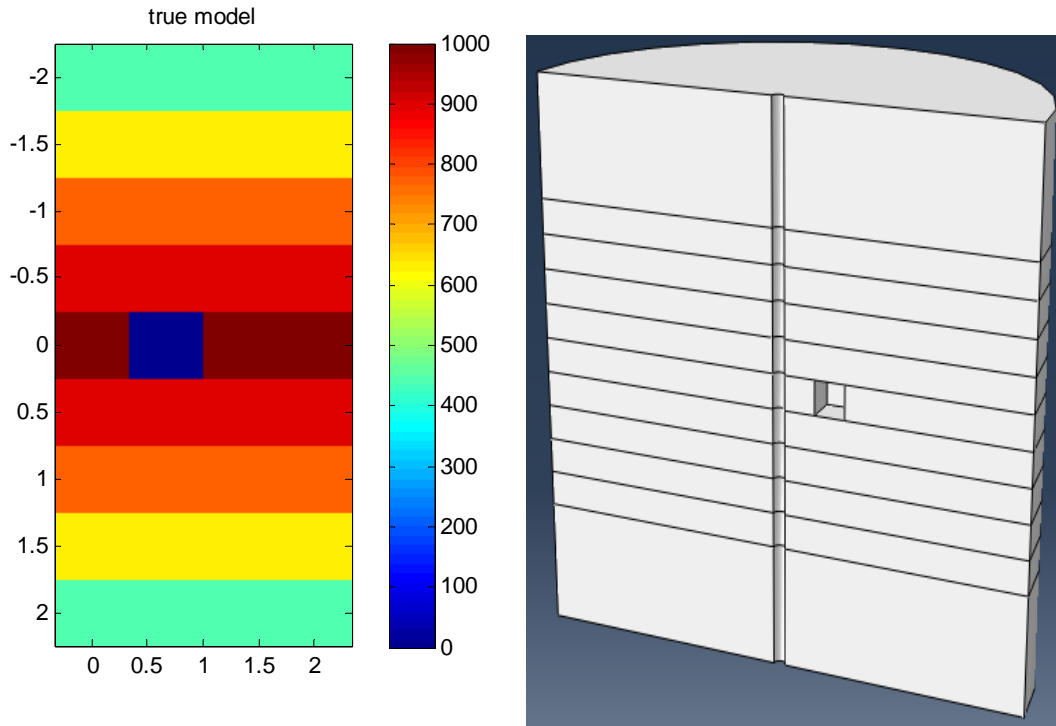


Figure 5-21. Synthetic model 5: true model and velocity section

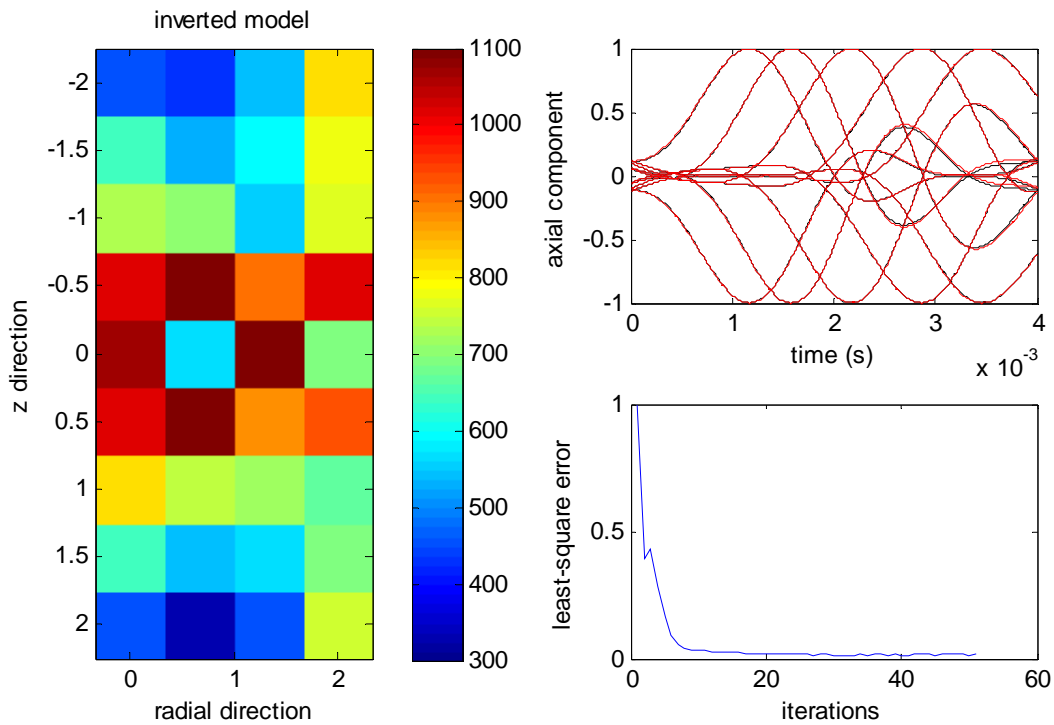


Figure 5-22. Synthetic model 5: inversion result of 0-degree plane

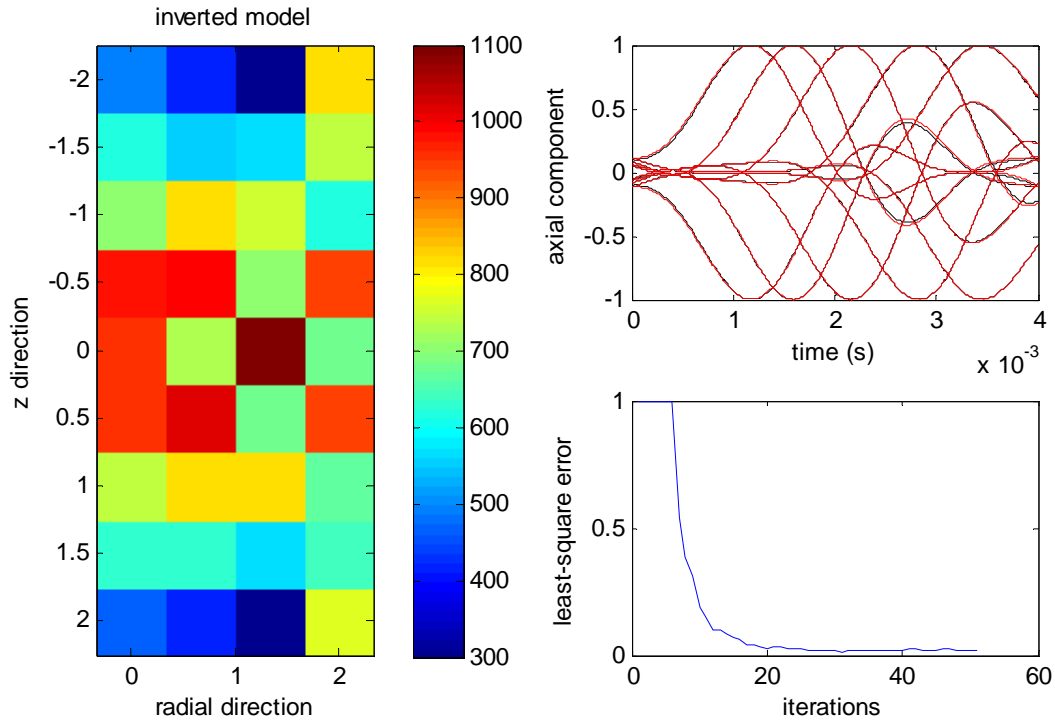


Figure 5-23. Synthetic model 5: inversion result of 90-degree plane

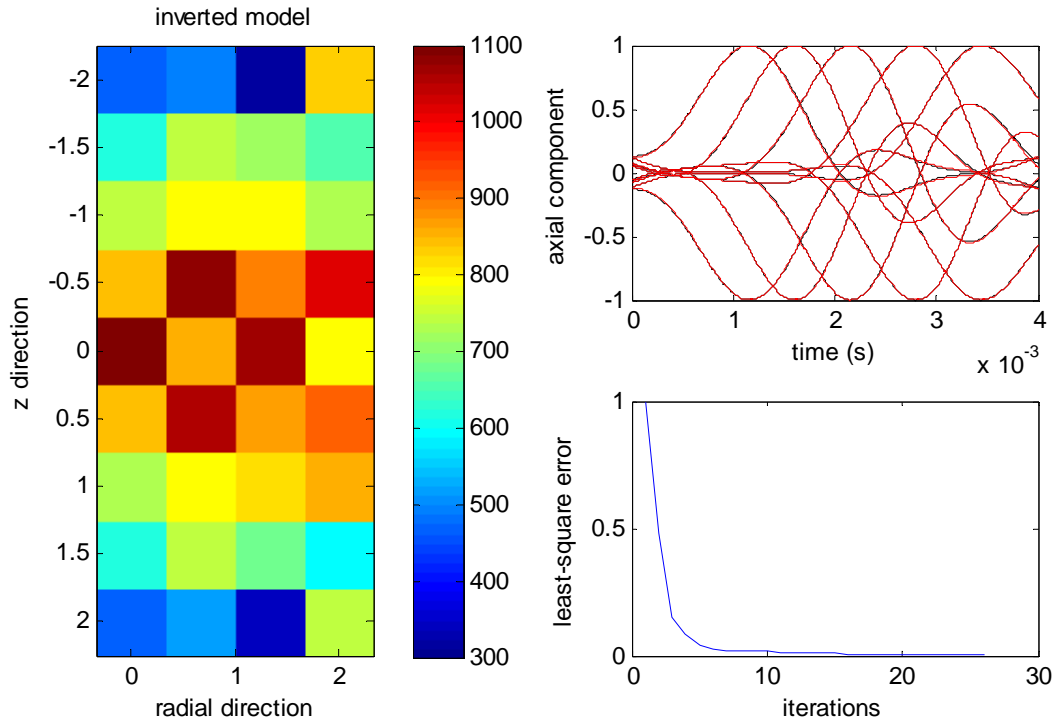


Figure 5-24. Synthetic model 5: inversion result of 180-degree plane

CHAPTER 6 CLOSURE

6.1 Summary of Findings

The technique of borehole-based FWI using a regularized Gauss-Newton method has been developed to provide high-resolution velocity images along and around a borehole at depth and within a socket proposed for use in the design of a drilled shaft foundation. The capability of the proposed imaging technique has been demonstrated through comprehensive synthetic model studies, and the findings are summarized as follows.

6.1.1 Forward Modeling

- Wave propagation inside a cylindrical cavity is complicated and significantly different from that on flat ground, due to a different set of boundary conditions imposed by the borehole geometry.
- ABAQUS is capable of modeling the borehole geometry and simulating wavefields generated from mechanically impacting sources (either point load or uniformly distributed ring load).
- Accurate 3-D borehole models and axisymmetric borehole models were both formulated using ABAQUS. The axisymmetric model with a ring load was chosen as the forward model to be used in the inversion, after considering the computational advantages and assumption limitations of the model.

6.1.2 Inversion System

- The regularized Gauss-Newton method proved to work well for the time-domain FWI within a borehole.
- An interface, written in Python script, was developed to integrate the forward model solved in ABAQUS into the inversion algorithm implemented in MATLAB.
- High nonlinearity of FWI coupled with a downhill optimization scheme requires a reasonably good starting model to avoid local minima. To lessen the restriction of the initial model, some strategies were adopted during the inversion stage, such as frequency filtering and temporal windowing, which proved to work well in the synthetic model studies.

6.1.3 Inversion Results

- The proposed imaging technique is capable of delineating Earth models that are either horizontally or cylindrically multi-layered. It is also capable of locating ring-type anomalies at various distances away from the borehole wall, embedded inside a homogeneous or a layered background.
- Despite the fact that the forward model is axisymmetric, detection of isolated anomalies was attempted. For synthetic models in this study, waveforms were collected at 0-, 90-, 180-degree planes in relation to the isolated anomaly, and then inverted. It was found that the axial and radial dimensions of a 0.5-m square anomaly within 2 m from a borehole can be accurately determined for all viewing planes. For the azimuth, the inverted velocity corresponding to its viewing plane increased as the angle between anomaly and viewing plane increased. Also, a slight but consistent time shift occurred in the associated wavefields. These two important observations can be explained by the fact that the reflected energy scattered by the anomaly attenuates as it propagates and is detected by the receivers at different timings.
- The proposed imaging technique appears to be capable of finding indications of isolated anomalies in the vicinity of a borehole. The key is to perform multi-plane waveform inversions around the borehole circumference. In the current implementation on a standard personal computer, it takes less than 4 hours per plane to produce the shear-wave velocity images. It is recommended that, in an actual test, six or eight planes be used for the imaging purpose, as waveforms can be recorded and processed simultaneously if the borehole logging tool is capable of doing so.

6.2 Conclusions

The findings outlined above have led to following conclusions. In order to perform FWI within a borehole, the cylindrical geometry and the associated boundary conditions must be modeled correctly. Due to the formidable computer time and uncertainty of 3-D borehole inversion, the axisymmetric forward model was chosen for the proposed imaging effort.

The inversion was based on a regularized Gauss-Newton method, and the interface between ABAQUS and MATLAB was developed using Python script. Inversions of synthetic data suggest that the proposed imaging technique is capable of delineating Earth models that are either horizontally or cylindrically multi-layered. It is

also capable of locating ring-type anomalies at various distances away from the borehole wall. For more realistic anomalies (voids and cavities), which are often spatially isolated, it is proposed that the inversion be done circumferentially on multiple viewing planes in relation to the anomalies. It was found that the axial and radial dimensions of the anomaly can be accurately determined for all viewing planes. Due to the nature of an axisymmetric forward model, the azimuth of the anomaly can be difficult to determine. However, comparing the velocity values of the anomaly inverted from multiple viewing planes revealed that the velocity increased as the angle between the anomaly and the viewing plane increased. This relationship can be explained by the fact that the reflected energy scattered by the anomaly attenuated as it propagated. In other words, the in-plane view exhibited the strongest reflection, while the 180-degree-out-of-plane view had the weakest. Furthermore, close comparison of the synthetic waveforms recorded on multiple viewing planes revealed that a slight but consistent time shift occurred in the associated wavefields, which can also be explained by the timing of reflection as a result of the anomaly. Therefore, the azimuth of the anomaly can be determined approximately.

6.3 Borehole Logging Tool

In this research, a single-well imaging technique based on full waveform inversion was developed. The potential of the technique was evaluated by synthetic data generated inside a borehole. However, to be able to implement in the field, a borehole logging tool that can effectively take advantage of the proposed imaging technique must be built. The basic design of the tool would include a seismic source and a receiver array, properly instrumented and integrated within a housing that can move up and down a borehole, is waterproof, and will couple to the borehole wall. The

seismic source should be capable of generating an omnidirectional, ring-type stress pulse that excites perpendicularly to the borehole wall. The receiver array, comprised of ten to twelve small-sized, three-component accelerometers, should be vertically placed at approximately a 15 cm interval along the borehole wall. To improve spatial coverage, the source should be designed such that it can repeatedly excite at multiple locations along the array. In practice, the borehole logging tool should be able to create a 3-D scan of material along and around the borehole by rotating the receiver array circumferentially inside the borehole. Alternatively, a 3-D receiver array, consisting of multiple 1-D vertical arrays discussed above, could be placed around the borehole circumference with a uniform azimuthal interval to improve the efficiency of the field testing.

6.4 Recommendations

The following recommendations are suggested after reviewing the findings and conclusions discussed above:

- A new borehole logging tool must be developed that is capable of generating and recording full waveforms from an instrumented array deployed vertically and circumferentially along the borehole wall. Physical modeling can then validate the proposed imaging technique before it is applied in the field.
- The system of FWI itself needs further development. For example, multiple shots can be added to increase the resolution of velocity recovery. Multi-variable inversion needs to be investigated for simultaneous reconstruction of both compressional and shear wave velocities, as well as density.
- The integration between ABAQUS and MATLAB offers many opportunities for solving inverse problems in general. These programs can easily simulate full waveform-based seismic crosshole tomography and vertical seismic profiling for the purpose of site characterization.
- 3-D surface-based FWI is still in its infancy. A successful inversion ultimately requires an extremely efficient forward model coupled with a carefully designed receiver array and a fairly good starting model. 3-D borehole-based FWI may be similarly managed where parallel computing is key.

LIST OF REFERENCES

- Aki, K. and Richards, P. (1980). *Quantitative Seismology: Theory and Methods*, W. H. Freeman, San Francisco, CA.
- Aster, R. C., Borchers, B., and Thurber, C. H. (2005). *Parameter Estimation and Inverse Problems*. Academic Press, Waltham, MA.
- ASTM Standard D4428/D4428M-07, 2007, "Standard Test Methods for Crosshole Seismic Testing," ASTM International, West Conshohocken, PA, 2007, DOI: 10.1520/D4428_D4428M-07, www.astm.org.
- ASTM Standard D7400-08, 2008, "Standard Test Methods for Downhole Seismic Testing," ASTM International, West Conshohocken, PA, 2008, DOI: 10.1520/D7400-08, www.astm.org.
- ASTM Standard D5777-00, 2011, "Standard Guide for Using the Seismic Refraction Method for Subsurface Investigation," ASTM International, West Conshohocken, PA, 2011, DOI: 10.1520/D5777-00R11E01, www.astm.org.
- ASTM Standard D7128-05, 2010, "Standard Guide for Using the Seismic-Reflection Method for Shallow Subsurface Investigation," ASTM International, West Conshohocken, PA, 2010, DOI: 10.1520/D7128-05R10, www.astm.org.
- Biot, M. A. (1952). "Propagation of Elastic Waves in a Cylindrical Bore Containing a Fluid." *Journal of Applied Physics*, 23(9), 997-1005.
- Bunks, C., Saleck, F. M., Zaleski, S., and Chavent, G. (1995). "Multiscale seismic waveform inversion." *Geophysics*, 60(5), 1457-1473.
- Burger, H. R. (1992). *Exploration Geophysics of shallow subsurface*. Prentice Hall, Englewood Cliffs, New Jersey.
- Chabot, L. (2003). "Single-Well Imaging Using Full-Waveform Sonic Data." M.S. thesis, the University of Calgary.
- Cheng, D. (1997). "Nondestructive Testing of Multilayered Cylindrical Structures." Ph.D. dissertation, the University of Texas at Austin.
- Coates, R., Kane, M., Chang, C., Esmersoy, C., Fukuhara, M., and Yamamoto, H. (2000). "Single-well Sonic Imaging: High-definition Reservoir Cross-sections from Horizontal Wells." SPE/CIM International Conference on Horizontal Well Technology, Calgary, Canada.
- Constable, S., Parker, R., and Constable, C. (1987). "Occam's inversion: A practical algorithm for generating smooth models from electromagnetic sounding data." *Geophysics*, 52(3), 289-300.

- Fernandez, A. and Santamarina, J. C. (2003). "Design Criteria for Geotomographic Field Studies." *Geotechnical Testing Journal*, 26(4), 410-420.
- Fortin, J. P., Rehbinder, N., and Staron, P. (1991). "Reflection imaging around a well with the EVA full waveform tool." *The Log Analyst*, 32(3), 271-278.
- Foti, S. (2000). "Multistation Methods for Geotechnical Characterization using Surface Waves." Ph.D. dissertation, Politecnico di Torino, Italy.
- Hornby, B. E. (1989). "Imaging of near-borehole structure using full-waveform sonic data." *Geophysics*, 54(6), 747-757.
- Ingber, L. (1989). "Very fast simulated re-annealing." *Mathematical and Computer Modeling*, 12(8), 967-973.
- Kalinski, M. E. (1998). "Determination of In Situ Vs and Gmax Using Surface Wave Measurements in Cased and Uncased Boreholes." Ph.D. dissertation, the University of Texas at Austin.
- Kitsunezaki, C. (1980). "A New Method for Shear Wave Logging." *Geophysics*, 45(10), 1489-1506.
- Lailly, P. (1983). "The seismic inverse problem as a sequence of before stack migrations." Conference on Inverse Scattering, Theory and Application, Society of Industrial and Applied Mathematics, Expanded Abstracts, 206-220.
- Lamb, H. (1904). "On the Propagation of Tremors over the Surface of an Elastic Solid." *Philosophical Transactions of the Royal Society of London*, A203, 1-42.
- Levenberg, K. (1944). "A Method for the Solution of Certain Non-Linear Problems in Least Squares." *The Quarterly of Applied Mathematics*, 2(2), 164-168.
- Love, A.E.H. (1892). *A Treatise on the Mathematical Theory of Elasticity*, Cambridge University Press, England.
- Marquardt, D. W. (1963). "An Algorithm for Least-Squares Estimation of Nonlinear Parameters." *Journal of the Society for Industrial and Applied Mathematics*, 11(2), 431-441.
- McMechan, G. A. and Yedlin, M. J. (1981). "Analysis of dispersive waves by wave field transformation." *Geophysics*, 46(6), 869-874.
- Mok, Y. J., Stokoe, K. H., II, and Wilson, C. R. (1988). "Analysis of downhole seismic data using inverse theory." Proceedings of Ninth World Conference on Earthquake Engineering, 3(1), 65-70, Tokyo, Japan.
- Mora, P. R. (1987). "Nonlinear two-dimensional elastic inversion of multi-offset seismic data." *Geophysics*, 52(9), 1211-1228.

- Mora, P. R. (1989). "Inversion = migration + tomography." *Geophysics*, 54(12), 1575-1586.
- Nazarian, S. and Stokoe, K, H, II (1984). "Nondestructive Testing of Pavements Using Surface Waves." *Transportation Research Record*, 993, 67-79.
- Nigbor, R. L., and Imai, T. (1994). "The suspension P-S velocity logging method." Geophysical Characterization of Sites, ISSMFE, Technical Committee 10 for XIII ICSMFE, 57-63, International Science Publishers, New York.
- NRC. (2000). Seeing into the Earth: Noninvasive Characterization of the Shallow Subsurface for Environmental and Engineering Applications, National Academy Press, Washington D.C.
- Palmer, D. (1980). The Generalized Reciprocal Method of Seismic Refraction Interpretation. Society of Exploration Geophysicists, Tulsa, Oklahoma.
- Park, C. B., Miller, R. D., and Xia, J. (1999). "Multi-Channel Analysis of Surface Wave (MASW)." *Geophysics*, 64(3), 800-808.
- Plassix, R. E. (2008). "Introduction: Towards a full waveform inversion." *Geophysical Prospecting*, 56(6), 761-763.
- Pratt, R. G. and Worthington, M. H. (1990). "Inversion theory applied to multi-source cross-hole tomography. Part 1: Acoustic wave-equation method." *Geophysical Prospecting*, 38(3), 287-310.
- Pratt, R. G. (1990). "Inversion theory applied to multi-source cross-hole tomography. Part 2: Elastic wave-equation method." *Geophysical Prospecting*, 38(3), 311-329.
- Pratt, R. G., Shin, C., and Hicks, G. J. (1998). "Gauss-Newton and full Newton methods in frequency-space seismic waveform inversion." *Geophysical Journal International*, 133(2), 341-362.
- Rayleigh, L. (1885). "On Waves Propagated along the Plane Surface of an Elastic Solid." *Proceedings of the London Mathematical Society*, 17(1), 4-11.
- Romdhane, A., Grandjean, G., Brossier, R., Rejiba, F., Operto, S., and Virieux, J. (2011). "Shallow-structure characterization by 2D elastic full-waveform inversion." *Geophysics*, 76(3), R81-93.
- Santamarina, J. C. and Fratta, D. (2005). Discrete Signals and Inverse Problems: An Introduction for Engineers and Scientists, John Wiley & Sons, Chichester.
- Schlumberger. (1997). DSITM – Dipole Shear Imager: Corporate brochure SMP-9200, 36 pages.

- Sen, M. K. and Stoffa, P. L. (1992). "Rapid sampling of model space using genetic algorithms: examples from seismic waveform inversion." *Geophysical Journal International*, 108(1), 281-292.
- Sheen, D. H., Tuncay, K., Baag, C. E., and Ortoleva, P. J. (2006). "Time domain Gauss-Newton seismic waveform inversion in elastic media." *Geophysical Journal International*, 167(3), 1373-1384.
- SIMULIA ABAQUS 6.11, Dassault Systems, ABAQUS Inc., 2011.
- Sirgue, L. and Pratt, R. G. (2004). "Efficient waveform inversion and imaging: A strategy for selecting temporal frequencies." *Geophysics*, 69 (1), 231-248.
- Stokoe, K. H., II and Woods, R. D. (1972). "In Situ Shear Wave Velocity by Cross-Hole Method." *Journal of the Soil Mechanics and Foundation Division*, 98(5), 443-460.
- Stokoe, K. H., II, Wright, S.G., Bay, J. A., and Roesset, J. M. (1994). "Characterization of geotechnical sites by SASW method," *Geophysical Characteristics of Sites*, ISSMFE, Technical Committee 10 for XIII ICSMFE, International Science Publishers, New York, 15-25.
- Stokoe, K. H., II and Santamarina, J.C. (2000). "Seismic-Wave-Based Testing in Geotechnical Engineering," *International Conference on Geotechnical and Geological Engineering*, Melbourne, Australia, 1490-1536.
- Tarantola, A. (1984). "Inversion of seismic reflection data in the acoustic approximation." *Geophysics*, 49(8), 1259-1266.
- Tarantola, A. (1987). *Inverse Problem Theory: Methods for Data Fitting and Model Parameter Estimation*, Elsevier Science Publ. Co., New York.
- Tran, K. T. and Hiltunen, D. R. (2012). "Two-Dimensional Inversion of Full Waveforms Using Simulated Annealing." *Journal of Geotechnical and Geoenvironmental Engineering*, 138(9), 1075-1090.
- Tran, K. T., Hiltunen, D. R., Sarno, A. I., Hudyma, N. (2011), "Geophysical Testing of Rock and its Relationships to Physical Properties," *Final Report for Contract FDOT BDK-75-977-01*, Florida Department of Transportation, February, 190 pp.
- Tran, K. T. and McVay, M. C. (2012). "Site characterization using Gauss-Newton inversion of 2-D full seismic waveform in the time domain." *Soil Dynamics and Earthquake Engineering*, 43(1), 16-24.
- Virieux, J. and Operto, S. (2009). "An overview of full-waveform inversion in exploration geophysics." *Geophysics*, 74(6), WCC1-26.
- White, D. J. (1989). "Two-Dimensional Seismic Refraction Tomography." *Geophysical Journal International*, 97(2), 223-245.

Zerwer, A., Cascante, G., and Hutchinson, J. (2002). "Parameter Estimation in Finite Element Simulations of Rayleigh Waves." *Journal of Geotechnical and Geoenvironmental Engineering*, 128(3), 250-261.

Zhang, J. and Toksoz, M. (1998). "Nonlinear refraction travelttime tomography." *Geophysics*, 63(5), 1726-1737.

Zywicki, D. J. (1999). "Advanced Signal Processing Methods Applied to Engineering Analysis of Seismic Surface Waves." Ph.D. dissertation, the Georgia Institute of Technology.